MANIPULATING SPATIOTEMPORAL VARIABLES TO PROGRAM COORDINATED BEHAVIORS IN MICROBIAL CONSORTIA.

by

Sonali Gupta

A dissertation submitted in partial fulfillment of
the requirements for the degree of

Doctor of Philosophy
(Biophysics)

at the
UNIVERSITY OF WISCONSIN–MADISON
2021

Date of final oral examination: 08/05/2021

The dissertation is approved by the following members of the Final Oral Committee:

Jo Handelsman, Professor, Microbiology
William Bement, Professor, Cell & Molecular Biology
Ophelia Venturelli, Assistant Professor, Biochemistry
Philip Romero, Assistant Professor, Biochemistry
Megan McClean, Assistant Professor, Biomedical Engineering

DISCARD THIS PAGE

TABLE OF CONTENTS

DISCARD THIS PAGE

LIST OF TABLES

DISCARD THIS PAGE

LIST OF FIGURES

Appendix
Figure Page

ABSTRACT

Microbes use sophisticated mechanisms to coordinate community-level functions in complex environments. Intracellular gene regulatory networks, as well as the physical processes that mediate intercellular signaling and exchange, both present spatial and temporal constraints that can alter the nature of the information being communicated. Here we investigate the effects of spatiotemporal variables in programming coordinated behaviors within microbial consortia. We first design a microfluidic platform to investigate how the spatial arrangement of microbes impacts gene expression and growth. We elucidate key biochemical parameters that dictate the mapping between spatial positioning and gene expression patterns. We show that distance can establish a low-pass filter to periodic inputs and can enhance the fidelity of information processing. Spatial separation enhanced the disparate roles of positive and negative feedback on the synchronization and robustness of a genetic oscillator distributed between two strains. We implemented relay signaling to extend the spatial range of microbial communication in a patterned agarose device by constructing an amplify-and-forward circuit and mutating its regulatory sequences to modify the dose response. Quantification of growth and metabolite release in an amino-acid auxotroph community demonstrates that the interaction network and stability of the community are highly sensitive to temporal perturbations and spatial arrangements. In sum, we use a small number of gene regulatory modules to generate a diverse portfolio of collective behaviors by introducing spatial and temporal variations in the signaling and exchange processes of microbial consortia.

Chapter 1

Introduction

1.1 Life Finds a Way

Just as early genetics papers revealed that there are elegant ways of breaking systems to understand their logic, synthetic biology shows us that there are clever ways of building systems in order to better understand how life works. The past five years of research into the rich and messy terrain of life has been a constant exercise in humility alongside regular encounters with the profound. Living systems can be precisely tuned yet noisy, machinic yet idiosyncratic, optimized yet ever evolving. To study such systems is to play with models that are useful even if they aren't true, and involves experiments with a clear hypothesis but data that forces you to see beyond it.

Here I present a story in five acts that shows that space and time are not simply the background for biological phenomena, rather, these variables are themselves factors mediating the intensive processes of living systems.

1.2 Gene Regulatory Network Design

Those familiar with molecular biology understand a gene as a sequence of DNA that gets copied into RNA and then converted into a corresponding sequence of amino acids, which folds onto itself to make a protein capable of catalyzing a particular biochemical reaction. Those unfamiliar with this process have perhaps a more metaphysical understanding of a gene as an abstract piece of biological information that somehow encodes a trait. While both the mechanistic and metaphysical aspects of this process can be infinitely elaborated on, it is more instructive for the purposes of this study to begin with their shared understanding of a gene as a unit of information.

Francis Crick emphasized this information-based perspective in his classic paper formulating the central dogma of molecular biology, claiming that the information contained within a DNA sequence can flow unidirectionally to dictate a protein's sequence, and that "once sequential information has passed into the protein, it cannot get out again" [1]. While this central dogma marks one of the first attempts to trace information propagation to and from the gene, it is premised on the narrow definition of “sequential information,” where such information flows from DNA to RNA to the protein. However, the innumerable mechanisms by which proteins influence the expression of DNA, and thereby act as conductors of information enabling genes to self-regulate, begs the more expansive formulation of biological information developed through systems biology. Beyond the linear logic of the central dogma, a systems perspective makes evident that “information flows multi-directionally between different tiers of biological information, of which genes, transcripts and proteins constitute only the most obvious three” [2]. Thus if we understand genes as units of biological information, we can define a gene regulatory network as a system that conducts the flow of information to and from genes to orchestrate a particular biological function.

Gene regulatory networks as assemblages of core motifs

Figure 1.1 shows a basic schema of a gene regulatory network (GRN) where a given set of genes constitute nodes within the network and the edges reflect the influence of each gene on others and/or itself. Genes influence each other through various mechanisms, both directly and indirectly, often mediated by their protein products.[1] Feedback within the network occurs when genetic outputs (proteins or otherwise) in turn alter the expression of some or all of the genes that produced them. A positive feedback loop (**Figure 1.2**) is formed when the expression of a gene produces a protein that further increases the expression of the gene. Conversely, a negative feedback loop (**Figure 1.2**) occurs when the expression of a gene inhibits its further expression. Often feedback occurs via the interaction with other genetic or molecular components in the network. Autoregulation refers to schemas in which feedback occurs in the absence of these other components, for instance, the direct interaction of a protein with the DNA sequence that encodes it (**Figure 1.2**). A GRN can be composed of interwoven positive and negative feedback loops acting in an autoregulatory or intersecting manner.

The expression levels of each gene in the network characterizes the ‘state’ of a GRN at a given timepoint. The network may change its state in response to exogenous inputs or changing conditions, such as the complex GRNs that govern stress-responses in bacteria in response to nutrient-starvation [4]. The network may also operate relatively autonomously as a function of its own internal dynamics, as seen in time-keeping GRNs that regulate the circadian rhythm even in the absence of external inputs like light [5]. A mathematical analysis of the network topology can determine the possible states of a given GRN, including states that are theoretically possible even if they have not been experimentally observed [6,7]. Because GRNs are high-level representations of information flow within a biological network, the numerical parameters that govern state

---

[1] Proteins such as transcription factors or recombinases act interact directly with DNA to regulate expression. RNA transcripts can also directly and indirectly regulate gene expression in a variety of ways.

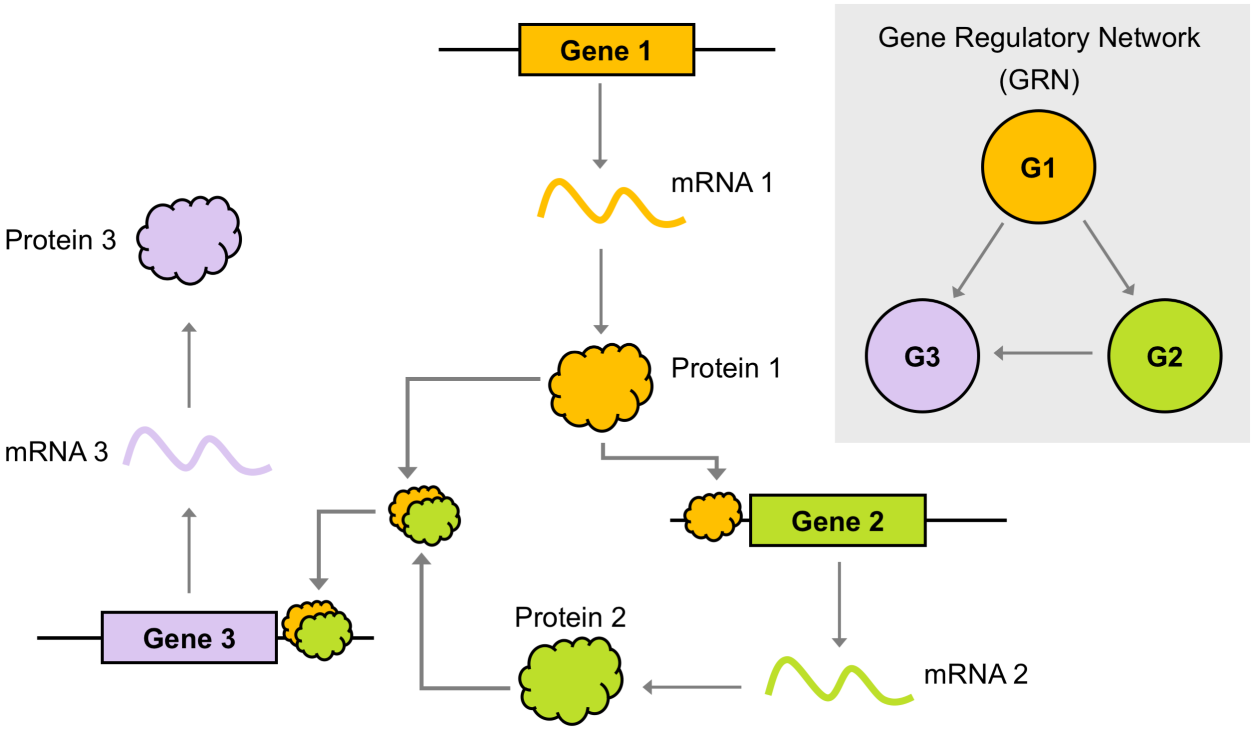

Figure 1.1: A schematic of a gene regulatory network. Gene 1 is transcribed and translated into a Protein 1, which directly interacts at a regulatory site of Gene 2 to regulate its expression. Proteins 1 and 2 require each other to regulate Gene 3, which is therefore indirectly regulated by Genes 1 and 2. The combined influences of all genes on themselves and on each other is abstracted into a gene regulatory network, shown on the right. Note that information does not flow 'backwards' in this network (i.e. from Protein 1 to Gene 1) directly or indirectly – the circuit depicted here lacks feedback. *Figure adapted with modifications from* [3].

transitions of GRNs often reflect several 'lumped' biophysical processes. One of the aims of this study is to identify parameters that can generate spatially-determined responses in GRNs.

In living systems, noise is often a key parameter dictating the stability of a GRN in a given state, and its ability to transition between states [6, 8, 9]. GRNs can also exhibit memory, such that the past states of the system influence the requirements for the system to inhabit future states [10]. Simple GRNs composed of only two genes (such as the toggle-switch discussed below) can exhibit complex behavior that integrates features such as noise and memory [11, 12]. This underscores the fundamental principle that "complexity in life does not arise from a disparity in the number of available components (genes), but from the nature and

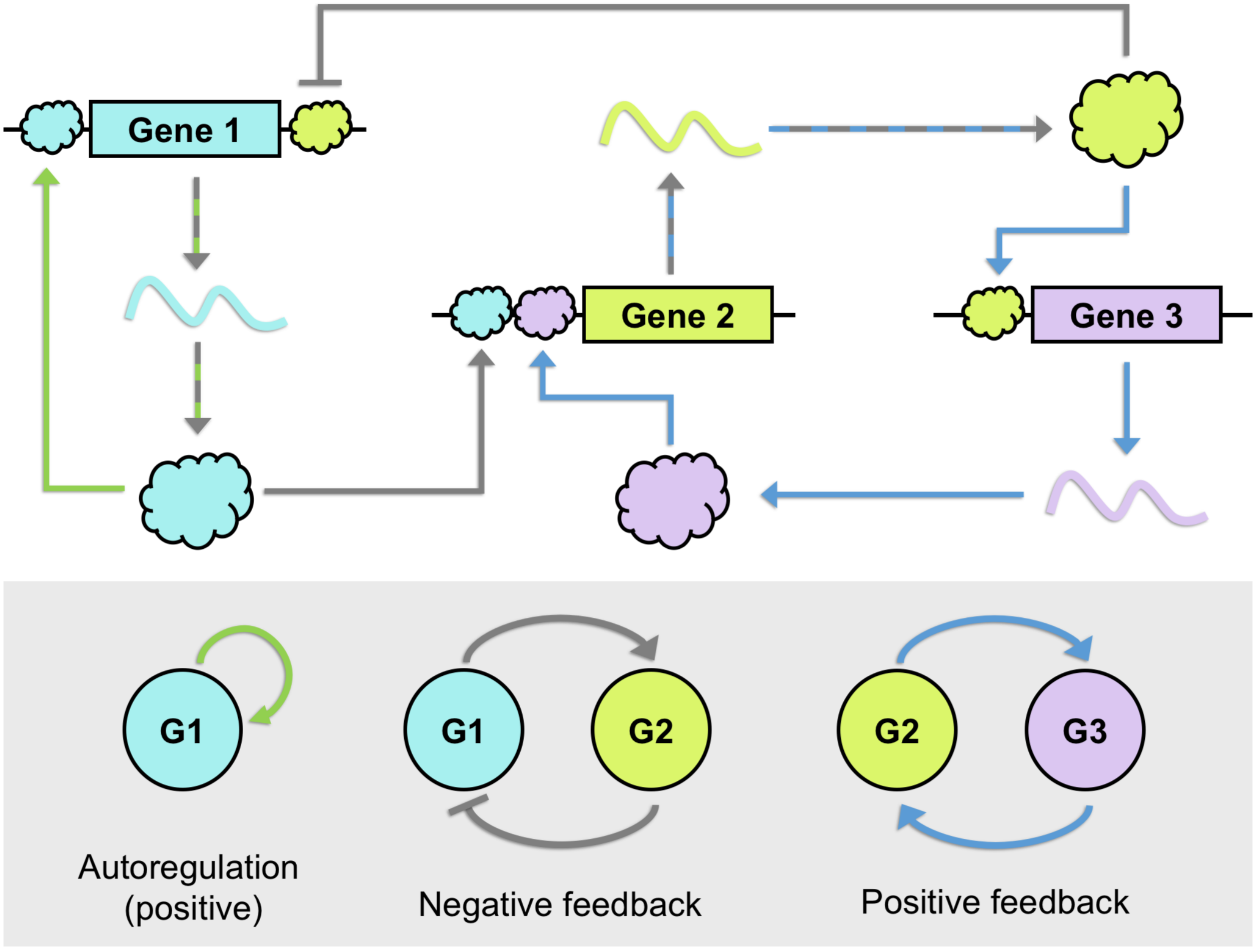

Figure 1.2: Positive and negative feedback in a gene regulatory network. Gene 1 in this network is autoregulatory (grey arrows) as its protein product directly increases its own expression. Gene 1 also indirectly inhibits its own expression by promoting its repressor, Gene 2 (pink arrows). Gene 2 and Gene 3 increase their expression through an indirect positive feedback loop with each other (blue arrows).

dynamics of the interactions between such components" [3]. Thus, complex functions can be engineered in biological contexts by altering the network of relations between relatively few components.

We might then ask, why are naturally occurring GRNs that govern relatively simple functions quite elaborate in design? For instance, the GRN that governs the viral switch between exponential replication (the lytic phase) and silent integration into the host's genome (the lysogenic phase) utilizes multiple components and layers of feedback regulation [13], and integrates noise as a key variable [14]. The complexity of native

GRNs reflects the fine-tuned logic of adapting to multitudinous contingencies throughout evolutionary history [15, 16]. Nevertheless, across the tree of life, we can identify the consistent reoccurrence of numerous elemental motifs that, when hierarchically assembled, compose the architecture of native GRNs [16, 17]. These motifs are the point of departure from which we can derive generalizable principles of gene circuit design.

A brief history of synthetic gene circuits

The toggle-switch was the first instance of an entirely synthetic core gene regulatory motif designed and constructed in living cells [11]. The system was built using parts from the genetic module governing the lytic-lysogenic decision in the virus bacteriophage λ, reconstructing its switch-like logic with two genes that each inhibit the expression of the other such that when one gene is in the ON state, the other is forced into the OFF state (**Figure 1.3,**top). The two possible stable states of this genetic circuit make it a bistable system that can be 'toggled' by the addition of inducers that intervene in one of the two mechanisms of repression. The system remains in the state it was toggled into in the absence of further inputs, exhibiting a basic form of cellular memory [11]. This history dependence, or hysteresis, is a characteristic of bistable systems and can be constructed with any set of biological components, so long as the network topology is preserved. Indeed, reproducing this topology using electrical components instead of genetic parts results in the reset-set latch, a basic circuit element for storing memory in electronics [18].

The first synthetic gene clock in living cells was constructed by assembling biological components to reflect the topology shown in **Figure 1.3,**bottom [19]. Under a set of defined conditions, this system maintains stable oscillations such that the expression of each gene cycles in time, out of phase with the expression of the other genes. The repressilator reflects yet another generalizable principle of circuit design; that an even number of mutually repressing genes creates a switch-like function, whereas an odd number of genes in the negative feedback loop produce cyclical behavior [20]. The repressilator thus reflects a cardinal motif present in the time-keeping functions of various naturally occuring GRNs, such as those governing circadian rhythms in plants [21] and mammals [22].

The toggle-switch and the repressilator were formative for the discipline of synthetic biology because they demonstrated that information processing functions can be engineered in living systems by restructuring biomolecular components according to fundamental design principles. The past two decades in synthetic biology have seen the unrelenting development of what is now a vast arsenal of synthetic GRNs capable of functions such as multi-layered digital logic [24–27], signal amplification [28–31], memory [32–34], dynamic filtration [35, 36], decryption [37–39], pattern [6, 7, 40–43] and pulse [44] generators, integral feedback controllers [45], and state machines [46], just to name a few. These biological computers can interface with everything from living materials [47] to electronics [48], and can remain operative in environments beyond

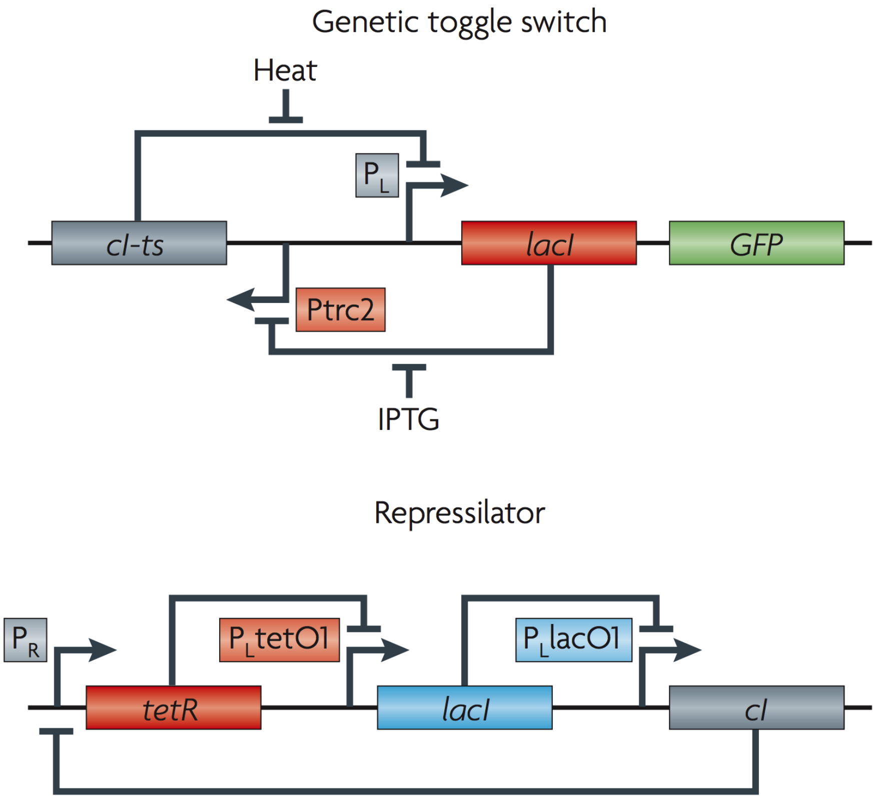

Figure 1.3: Core GRN motifs: the toggle switch and the repressilator. Top: in this genetic toggle switch, two inputs to the system, heat and a chemical inducer, IPTG, each alleviate the inhibition of one of the repressive mechanisms, causing the system to flip between states. Bottom: gene circuit design of the first synthetic gene clock, the repressilator, in which expression of the genes *tetR*, *lacI* and *cI* oscillate in time, phase-shifted with respect to each other. *Figure reproduced from* [23].

the living cell, from cell-free lysates [49,50] to protocells [51]. The unique challenges encountered in the process have in turn enriched analytical frameworks in theoretical fields ranging from information science [52] to control theory [53, 54]. In this work, I design and construct GRNs in bacteria with the aim of determining how the biophysical processes involved in information propagation and molecular exchange alter the collective behaviors of microbial consortia.

Gene regulatory networks designed and constructed for this study

The GRNs engineered for this research were distributed across two populations and are thus represented by interactions between cells which contain the genes of interest (**Figure 1.4**). I begin with the implementation of a communication module divided across two strains of *Escherichia coli*. The sender population is programmed to generate a molecular signal that is received by the receiver population, which turns on a gene in response (**Figure 1.4a**). With no feedback involved, this gene circuit reflects the unidirectional flow of information from one set of cells to another. I investigate how the internal variables of this synthetic communication system affects information propagation from sender to receiver. By spatially separating the populations, I identify circuit parameters that can alter the spatial profile of gene expression of the receivers. I further study the temporal response of the circuit by generating forced oscillations in the system and characterize the fidelity of information propagation from senders to receivers by calculating the signal-to-noise ratio of gene expression as a function of their spatial separation.

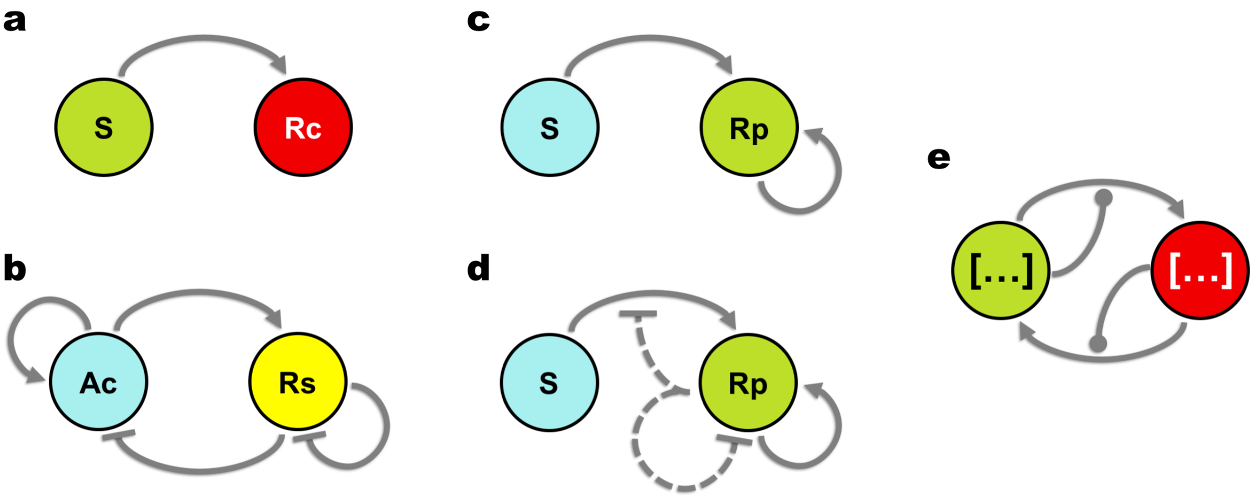

Figure 1.4: Gene regulatory networks designed and constructed for this study. **(a)** Senders (S) generate a signal that turns on gene expression in the receivers (Rc). **(b)** A dual-feedback circuit in which an activator population (Ac) turns on gene expression in itself and in the repressors (Rs), whereas the repressors inhibits gene expression within itself and in the activators. **(c)** Senders (S) turn on gene expression in repeaters (Rp), which in turn autoregulate to enhance their expression. d Negative feedback is added to the GRN shown in **(c)** such that the repeaters inhibit the incoming signal from the senders as well as their own positive feedback mechanism. Dotted lines indicate that the negative feedback occurs at a time delay. **(d)** Two populations cross-feed necessary metabolites to each other, establishing a positive feedback loop. The metabolites have unique roles within the cell, and are involved in complex GRNs (denoted by the ellipses) that regulate cell growth, gene expression, and the production of shared metabolites. These intracellular processes in turn alter the positive feedback in disparate ways, represented by circular line-ends.

I further investigate a bidirectional communication module involving both positive and negative feedback using a gene circuit motif known as the Smolen oscillator [55], which has the distinct property of synchronizing the expression of the two genes involved in the circuit [56] (**Figure 1.4b**). The genetic oscillator is split between two cell populations; the activator population executes positive autoregulation and activation of gene expression in the repressor population, which in turn exhibits negative autoregulation and inhibits gene expression in the activators. Information flow in this circuit is bi-directional, and mediated by two orthogonal signals, one generated by each strain. I studied the effects of spatial separation on the synchronization of gene expression between the activator and repressor populations.

The sender-receiver communication module was altered to create a sender-repeater circuit capable of relay communication (elaborated in the following section). The repeater cells reproduce the signal received from the senders, creating an autoregulatory positive feedback loop (**Figure 1.4c**). Signal amplification by the repeaters serves to propagate information further across space. Genetic variants of the repeater strain were engineered to alter internal circuit parameters such as the threshold of signal required for activation of gene expression. The effect of different spatial arrangements of these variants on information propagation is studied in the context of relay signaling. I additionally characterize the influence of signal amplification and circuit parameters on noise in information transfer.

A core motif ubiquitous in GRNs throughout the natural world is the incoherent feed-forward loop (IFFL), known for its unique information-processing functions [36, 57]. The 'incoherence' of this circuit topology comes from the antithetical effect the first gene in the cascade has on the last; expression of the first gene activates expression of the last gene in the cascade through one mechanism, while simultaneously repressing its expression through another. Symmetry breaking between the positive and negative mechanisms of regulation grants the IFFL its distinct function in spatial and temporal dimensions. If the signal associated with the activation mechanism travels further in space than the inhibitory signal, a spatial band pattern is observed [58, 59]. If instead the activation signal proceeds at a faster rate than the inhibitory signal, a pulse is generated in time [44]. I construct an IFFL motif by building the fast-activation mechanism with the sender-repeater system, and reprogramming the repeaters to degrade the signal with a delay relative to the activation mechanism (**Figure 1.4d**). I investigate the properties of information propagation in this system, with the aim of generating traveling waves with a capacity for destructive interference.

Finally, I explore a synthetic community composed of two cell populations in which one strain, ΔPhe, is an E. coli mutant incapable of synthesizing phenylalanine, and the second strain, ΔMet, cannot synthesize methionine. As both methionine and phenylalanine are essential for cell survival, the strains cannot grow in the absence of either amino acid. When these amino acids are not present in the environment, the only source of the missing amino acid for each strain is its partner strain. Thus the two cell populations are compelled to cross-feed for survival, establishing a relationship known as auxotrophy. While the strains' mutualism may be likened to a positive feedback loop, because each amino acid plays a singular role in a variety of metabolic processes within the cell, the engineered feedback loop in this system interfaces with the native GRNs regulating the metabolic processes of each strain (**Figure 1.4e**). The growth dynamics of each strain are observed over time to deduce the cumulative effects of the two distinct and complex native GRNs associated with each amino acid linked through positive feedback.

Based on an understanding of GRNs as assemblages of core motifs that possess distinct information-processing functions, I have outlined the repertoire of gene circuits designed and synthetically constructed in this study in order to orchestrate coordinated behavior in microbial consortia. I now turn to the physical processes that mediate this coordination of function across space and in time.

1.3 Biophysical Processes Mediating Information Exchange in Microbial Consortia

While GRNs delineate information-processing modules within cells, the physical processes that mediate communication within and between GRNs can themselves alter the nature of what is being communicated [60]; information cannot be considered separately from its mode of propagation. This section therefore deals with the spatial and temporal dimensions of the biophysical processes of communication engineered within microbial consortia. The two interacting modules for every GRN presented in this study are separately encoded within distinct populations of *E. coli*, resulting in two strains that remain spatially separated from each other. The physical movement of signals and metabolites functions as a link between the two strains that completes the logic of their circuit. Thus, diffusion is the primary means of information transfer in this study. In this section, I first review key variables of diffusive processes that mediate communication within and across GRNs, followed by a brief discussion of the circuit parameters relevant to the communication mechanisms used in the GRNs.

Diffusion-mediated signaling and exchange in a highly controlled microenvironment

Diffusion is a ubiquitous phenomenon in biological systems across many scales, governing innumerable processes, from a DNA-binding protein locating its binding site [61], intercellular signaling [**?**, 62], and long-range communication across ecosystems [63, 64]. The diffusion coefficient defines the flux of a particle, that is the area traveled per unit time, in response to a standard difference in its concentration. This value depends on numerous variables such as the size of the particle, the density of the medium, the temperature, and the pressure. The effective diffusion coefficient can even be influenced by structural features of the environment, such as porosity [65]. The initial spatial distribution of the diffusing molecule is determined by its sources. If a biomolecule is generated by cells, the spatial arrangement of the cells, their density, and their overall population size are important variables in determining the net concentration and spatial distribution of the molecule. Additionally, the rate of production and the rate of degradation of the molecule, the presence of flow in the environment, and 'sinks' that sequester, dilute, or otherwise remove the molecule from circulation, all influence how its net concentration and spatial distribution evolves over time. It is evident that diffusive processes are inseparable from their environmental contexts, involving numerous variables that must be considered relative to one another.

Let us assume that two microbial strains are exchanging signals or metabolites via diffusion to coordinate their behavior in a natural environment such as the gut or soil microbiome. In addition to the variables listed above (which are always operative in diffusive processes), one could imagine numerous additional contingencies arising from these complex environments that could impact the nature of the interaction. For instance, disparities in the relative abundances of each strain in a given region can shape the nature of their interaction [66]. Factors affecting their spatial arrangement, such as the degree of mixing of the two strains and their degree of mobility in the environment, also dictate the relative concentrations of exchanged biomolecules in a given region, which in turn can dictate collective behaviors or community stability [63, 67, 68]. Indeed, the spatial organization of microbes can both influence, and be influenced by, the nature of their interactions [69–71]. The physical architecture of the environment (for instance, the dense protrusions of intestinal villi or the porousness of a clay particulate in soil) can further present geometric constraints or idiosyncracies that affect the spatial distributions of cells and the biomolecules that mediate their interactions [63, 72]. Finally, it is difficult to assess the robustness or responsiveness of microbial interactions to specific perturbations when numerous variables are simultaneously in flux. For this research, I fabricated a highly regulated microenvironment in order to eliminate confounding factors and isolate the intracellular and environmental variables that can reliably manipulate the activity of GRNs.

Microfluidic platforms are ideally suited for this purpose and have been extensively used for live cell culturing and imaging [56, 73–77]. By patterning a silicon mold with a customizable design that involves some combination of micron-scale channels, chambers, junctions, inlets/outlets, valves, or mixers, one can precisely direct the flow of small volumes of liquid through the device. There exist endless variations of microfluidic devices to perform a wide range of functions, from single-cell lineage tracking of replicating bacteria [78], to the generation of thousands of droplets that can be rapidly screened, each one a microreactor for a biochemical process or a microenvironment for the biological entities encapsulated within [76, 77, 79]. In this study, I design and construct a microfluidics platform to culture two physically separated populations of bacteria, while allowing the strains to interact via the diffusion-mediated exchange of biomolecules through interaction channels of varying micron-scale lengths (**Figure 2.1**). The population size and density of the strains were fixed by standardizing the size of the growth chambers. Micropumps are programmed to supply a continuous flow of media, providing nutrients and washing away excess cells as they grow out of the chamber. Media conditions can be altered at any point to dynamically modulate the behavior of the GRNs. Fluorescent proteins expressed by the bacteria provide readouts of GRN activity at the single-cell level, which is monitored in real-time by an inverted microscope. The symmetrical design of this device insulates the interaction channel from any net flow at equilibrium, such that the physical movement of signaling molecules and metabolites reflects only passive diffusion across the channel. The microfluidic platform thus confers precise and tunable control over various environmental parameters that impact diffusion-mediated intercellular interactions.

Features and functions of quorum sensing and relay signaling

With the exception of the metabolic exchange auxotroph system, all the GRNs used in this study are based on a mechanism known as quorum sensing, in which a diffusible signaling molecule interacts with components of the GRN to regulate gene expression [80, 81]. In its natural context, quorum sensing functions as a density-sensing mechanism wherein microbes generate low baseline levels of a small, diffusible signaling molecule, known as an autoinducer, while simultaneously sensing its concentrations in the environment [82]. High cell densities cause the environmental concentrations of the autoinducer to exceed a critical threshold, upon which alterations in genetic regulation cause cells to transition from acting as individual agents to coordinating collective behavior [80, 83]. One of the most well characterized and commonly used quorum sensing systems is derived from an aquatic microorganism, *Vibrio fischeri*, which uses quorum sensing to synchronize luminescent behavior across its population [84]. In various microorganisms, quorum sensing catalyzes the formation of biofilms, extracellular three-dimensional matrices which facilitate communication, resource sharing, and environmental protection [85, 86]. Other quorum sensing functions include the regulation of virulence [87] and the contact-mediated exchange of DNA, a process known as conjugation [88]. In synthetic circuits, the genes, proteins, and signaling molecules of quorum sensing systems are commonly integrated with various extant biological components to perform a wide range of functions [41, 56, 74, 75, 89].

In this work, quorum sensing systems were assembled across populations of *E. coli* which communicate via the diffusion of signals called homoserine lactones (HSLs). While some GRN dynamics can be controlled by exogenously supplying chemical inputs to the system, each quorum sensing system also comes with a set of relatively fixed variables. For instance, the diffusion coefficient and degradation rate of each HSL is largely a function of its molecular properties, the viscosity of the medium, and the temperature of the environment, which are all kept fixed to optimize cell growth and circuit function within the microfluidic device. Altering the degradation rates of the HSLs would require a significant intervention to the circuit, as in the IFFL GRN (**Figure 1.4d**) which uses an intracellular enzyme, called a lactonase, to degrade HSL at a rate that can externally controlled. While the parameters defined by internal properties of quorum sensing systems remain experimental constants, their effect on GRN activity was nevertheless explored through computational simulations in this study.

The diffusion coefficient of signals and metabolites influences the spatial range of inter-microbial interactions [6], defined here as the distance across which one population can detectably respond to the other. The range of communication thus places a limit on the scale at which a signal can coordinate population-level behavior. Signaling molecules with greater diffusion coefficients can expand the spatial range of microbial interactions [74], but this strategy requires alterations to the mechanism of communication. In this study, I explore whether a mechanism called relay signaling can be used to tune the spatial range of a GRN by engineering cells to reproduce a signal upon its reception to further its spatial propagation via diffusion (**Figure 1.4c**). I further attempt to control the rate of signal propagation across a community by altering features of the positive feedack loop that governs signal regeneration. Relay signaling has been found to facilitate collective behavior in natural systems, such as optimizing the growth of a microbial community by coordinating resource sharing across the population [90]. We hypothesize that relay signaling could be used to engineer robust coordinated behaviors, for instance by generating all-or-nothing responses across a community or by making signal propagation less sensitive to variations in cell density. In this work I test relay signaling in patterned agar devices with bacteria cultured in 3 mm wells 1 cm apart connected by a communication channel (**Figure 2.3**). The input signal is generated by sender cells in the first well, with each subsequent well functioning as a relay 'node' in which repeater cells receive HSL from the previous node(s) and in turn regenerate HSL, furthering its diffusion to the next node(s).

1.4 Findings and Significance

The microfluidic device engineered to facilitate microbial interactions within a highly regulated microenvironment was found to maintain concentration gradients across the interaction channels in the device. Due to these gradients, as sender cells on one side of the interaction channel generate HSL, the concentration of HSL sensed by the receivers on the other end of the channels is dependent on the degree of spatial separation between the populations. In receiver cells, HSL forms an activated complex with its receptor to activate the expression of a gene encoding a fluorescent protein (**Figure 1.4a**). By measuring this fluorescence over time, we found that gene expression in receiver cells was a function of their distance from the sender cells; spatial information is thus encoded within the gene expression profiles of the receivers. This phenomenon is observed in natural systems; for instance bacteria sense glucose concentrations in their environment, and swim against its gradient to optimize nutrient availability [91]. Genetically programmed positional information is also the basis for morphogenesis in embryos, as specific combinations of signals, or morphogens, trigger distinct genetic programs, creating differential gene expression in response to overlapping morphogen gradients [92]. By establishing a platform to control environmental and circuit parameters in response to concentration gradients, we can engineer and test GRNs capable of performing spatially dependent functions.

We developed a mathematical model to represent the essential mechanisms involved in the GRN that produced this effect within the microfluidic environment and used computational techniques to ensure that the model was predictive of our experimental observations. This allowed us to simulate a variety of situations that would be challenging to test experimentally. We ran simulations across a large range of separation distances and found that just 150 sender cells could transmit a signal to receivers up to 1 mm away; a significant distance on the microbial scale. The model simulations also show that lowering the threshold of the signal required to prompt gene expression in the receivers would eliminate the spatial sensitivity of the response under the conditions tested. The model further predicted that spatial boundaries in gene expression could be engineered by 'digitizing' gene expression of the receivers, i.e. making their responses more switch-like. Finally, the model identified a correlation between the amount of HSL receptor in receiver cells and the signal threshold, pointing to an alternative strategy for tuning the spatial sensitivity of gene expression. Identifying the circuit parameters that can regulate spatial sensitivity and create spatial boundaries in a simple GRN informs circuit design strategies that can be applied to engineer pattern formation in bacteria.

Because the functions of GRNs are mediated by physical interactions between biomolecules, their rates of production and assembly, transport, and degradation can influence the rate of signal propagation within the GRN [93]. Intracellular processes that govern resource allocation, cell division, and metabolic flux can further impose a rate limit for accurate information processing within a GRN [94]. We can study the responsiveness and the accuracy of information processing within a system by introducing defined perturbations to system inputs, and determining their influence on the output. To do this, we forced oscillations in the senders by pulsing their gene expression at a constant frequency, and characterized the oscillations in gene expression in the receiver population. We found that driving the system at a slower oscillatory period of 2 h resulted in expected behavior; the period of the receiver gene expression matched the input period and the amplitude of the signal decreased with spatial separation, in agreement with model predictions. However, when we forced oscillations at double the frequency, we observed that oscillations displayed increased variability and the amplitude of receiver gene expression lost its dependence on distance. These higher-frequency fluctuations in the input were being damped by distance in diffusion-mediated signal propagation. Our results show that we can exploit the spatial arrangement of GRN components to filter out fluctuating environmental signals above a critical frequency.

Using spectral analysis, we quantified the distribution of the receiver gene expression across a range of frequencies. Because the senders were externally driven at a known frequency, the net power of receiver gene expression at this input frequency reflects an accurately transmitted signal across the sender-receiver GRN. The net power at all frequencies outside the signal bandwidth reflects the noise in receiver gene expression. We found that the signal-to-noise ratio in receiver gene expression at 2 h periodic forced oscillations decreased with spatial separation. Here the signal-to-noise ratio was dominated by high signal detected at shorter separation distances. However, when we doubled the frequency of forced oscillations, the output signal lost its dependence on distance while the noise increased at shorter distances. Therefore, at higher frequencies, the signal-to-noise ratio is greatest at longer separation distances as noise dominates at shorter separation distances. This result implies that for a given frequency of a fluctuating input, there exists an optimal distance that maximizes the fidelity of information transfer. We speculate that diffusional dissipation of the signaling molecule may damp fluctuations in its synthesis caused by driving the GRN close to its 'speed limit' [95]. This theory explains the observed reduction in noise over distance but also implies that spatial optimization of the signal-to-noise ratio is highly dependent on the source of the noise.

Having characterized a GRN in which information flows unidirectionally from sender to receiver, we next studied the effects of spatial separation on a dual-feedback system in which information flows bidirectionally between an activator and a repressor, and synchronizes oscillatory gene expression across the populations (**Figure 1.4b**). We found that increasing the spatial separation between activators and repressors disrupted their synchronized oscillations in divergent ways. The activators sustained the period of their oscillations while increasing the amplitude with distance, whereas the repressor displayed decreasing amplitudes and often an abrupt loss in oscillatory behavior with distance. By increasing their spatial separation, we effectively modulated the relative strength of inter-strain feedback to autoregulatory feedback. This result demonstrates that spatial patterning of microbial populations, or nodes in the GRN, can effectively tune the strengths of different edges of the regulatory network.

The loss of synchronized function with spatial separation in the dual-feedback oscillator demonstrates the sensitivity of microbial interactions to spatiotemporal parameters. We sought to engineer a microbial community that could display coordinated behavior across an extended spatial range using amplify-and-forward relay signaling. A patterned agar device was developed to study a relay mechanism in which a sender population, confined to the first node in a series, triggers a signaling cascade such that each subsequent repeater node receives the HSL signal, amplifies it, and forwards it to the next node in the series through diffusion (**Figure 1.4c**). We found that the baseline 'leakiness' in gene expression in the engineered repeaters was sufficient to activate the highly sensitive positive feedback loop and drive the system to saturation at a significant metabolic cost to the cells. Since the repeaters were able to auto-activate in the absence of signal from the senders, we sought to establish an OFF state by increasing the signal threshold required for activation. To do this, we inserted mutations in the regulatory sequence of the gene responsible for generating the HSL signal to generate four variants of the repeater strain. We characterize the activity of these variants and demonstrate that the mutations were able to alter a variety of circuit parameters. Notably, one of the variants displayed a 100-fold increase in the threshold required to trigger the amplify-and-forward relay mechanism. We test whether the repeater variants extend the spatial range of communication compared to the sender-receiver consortium. Our model identified the threshold as an important variable in generating delays and tuning spatial sensitivity. We thus explore the effect of a higher threshold on noise filtering, and propose a schema for engineering pulse-like excitable dynamics across the sender-repeater community (**Figure 1.4d**).

Coordinated behaviors in microbial communities often function to optimize growth or fitness [83,90]. We investigated the influence of spatial and temporal factors on the growth of $\Delta metA$ and $\Delta pheA$ strains cross-feeding methionine (M) and phenylalanine (F) in batch culture, and in spatially-separated and well-mixed conditions within the MISTiC microenvironment (**Figure 1.4e**). Regardless of the initial proportions of the two strains, the community reached a defined steady-state composition with the $\Delta pheA$ strain dominating the population fraction. This bias was also evident in the observed growth rates of strains in the spatially separated condition. $\Delta metA$ doubling times indicated very slow growth and no detectable dependence on spatial separation from the Δphe strain. In contrast, the doubling time for $\Delta pheA$ substantially decreased with distance from $\Delta metA$, indicating benefit from $\Delta metA$ despite the lack of growth in the latter. We titrated levels of all the amino acids available to the cells between 0.003X to 1X amino acids and observed increasing distance-dependence in strain interaction with decreasing amino acid concentrations. Across these experiments, the $\Delta pheA$ strain had an overall higher sensitivity of growth to distance. Given the disparity in growth rates between the MISTiC environment and batch culture, we sought to isolate only the effects of spatial separation on growth by culturing the strains together within MISTiC growth chambers. This well-mixed condition also displayed a stronger dependence of the growth rate of $\Delta pheA$ on $\Delta metA$ than the reciprocal.

The consistently low growth rates of $\Delta metA$ across all conditions as well as the benefit it confers to $\Delta pheA$ prompted us to 'rescue' the $\Delta metA$ strain by supplementing with 1X M. In response, the $\Delta pheA$ strain demonstrated two distinct growth phases; growth in the first phase is independent of distance, whereas growth in the second phase is augmented by increased spatial separation. This reversal in trend in the growth dynamics of $\Delta pheA$ indicates mild competition with $\Delta metA$. From this we can infer that the rapid growth of $\Delta metA$ resulted in a substantial decrease in the release rate of F. To verify this result we cultured each auxotroph strain in varying concentrations of its rescuing amino acid, and measured the amount of amino acid it secreted. Consistent with the MISTiC results we found that the $\Delta metA$ strain releases the most amount of F when its growth is arrested. As the strain is rescued, it begins to consume its own supply of F. The $\Delta pheA$ displayed the inverse trend, with no detectable M secretion until its growth rate was completely rescued at 1X amino acids. Our results point to the divergent metabolic roles of M and F in *E. coli.* The cell contains no metabolic 'sink' for F such excess F is simply secreted from the cell. In contrast, M is sequestered in the cell in the form of S-adenosyl-methionine, a donor of valuable methyl groups required as a necessary co-factor in a range of enzymatic reactions as well as DNA methylation. Spatial separation within this auxotroph community alters the amount of the rescuing amino acid received by each strain, and the resulting growth dynamics dictate whether the cells will release or sequester the amino acid required by their mutualistic partner. Our investigation of auxotrophic interactions demonstrates that the underlying regulatory networks of cell can have divergent effects on synthetic GRNs depending upon the spatiotemporal and environmental context.

Microbes have developed sophisticated mechanisms to orchestrate their transition from individual cells into assemblages capable of higher-order functions [83, 90]. For a given set of microbial interactions, one can map the underlying attractors or critical points to map possible states of the system. Yet, the topology of a GRN alone does not account for the physical processes that mediate information propagation across the population, and which may alter the nature of the information being communicated. Therefore, spatiotemporal considerations are not simply constraints on the system; rather they mediate that can shape its behavior. The research I present here explores the spatial and temporal aspects of inter-microbial communication, gene expression, and growth. I detail how circuit parameters interface with environmentally prescribed conditions, and identify their effects on the dynamic responses of various GRNs. I show that distance can establish a low-pass filter to periodic inputs and can enhance the fidelity of information processing. Using both computational and experimental approaches, I alter both the spatial range and the temporal delays of expression. I then implemented relay signaling to extend the spatial range of microbial communication in a patterned agarose device by constructing an amplify-and-forward circuit and mutating its regulatory sequences to modify the dose response. Quantification of growth and metabolite release in an amino-acid auxotroph community demonstrates that the interaction network and stability of the community are highly sensitive to temporal perturbations and spatial arrangements. Even though the GRNs used in this study were relatively simple two-component systems using only a few sets of signaling molecules, I managed to profile a diverse portfolio of behaviors only using spatial and temporal variations, demonstrating their fundamental importance in engineering coordinated functions.

Chapter 2

Microfluidic and Patterned Agar Devices to Study Microbial Interactions

Ecologically driven spatial heterogeneity in bacterial populations is often observed on the micrometer scale [72, 96, 97]. There exist key challenges to precisely patterning microbes at this scale, particularly within a dynamically controlled environment. Bacterial populations have been physically separated using patterned agarose [98], hydrogels [99], partitioned microfluidics [100], nanoporous membranes [97], cellulose nanofibrils [101], nanochannels [102], and bioprinting [103] techniques to study interactions and chemical signal communication. Many of these platforms don't enable a continuous flow environment which is necessary to apply transient perturbations and to wash out excess bacteria to maintain a constant population size. Microfluidic platforms are ideally suited for continuous culturing and dynamic inputs, and have been extensively used for live cell culturing and imaging [56, 73–77].

We developed a microfluidic platform, MISTiC (Mapping Interactions across Space and Time in Communities), to deepen our understanding of the effects of defined spatial structure and temporally changing environmental signals on microbial community properties. The device integrates micrometer-level spatial patterning, temporal control of environmental stimuli, and single-cell quantification of growth and gene expression within microbial consortia with real-time imaging in chemostat conditions. The population size and density of the strains were fixed by standardizing the size of the growth chambers. A pair of strains is physically separated across interaction channels of varying lengths through which the strains exchange diffusible biomolecules. The symmetrical design of this device insulates the interaction channel from any net flow at equilibrium, such that the physical movement of signaling molecules and metabolites reflects only passive diffusion across the channel. The microfluidic platform thus confers precise and tunable control over various environmental parameters that impact diffusion-mediated intercellular interactions.

We designed a second device, FAIRY (Forwarding Amplified Information with RelaY), out of agar patterned with a polydimethylsiloxane (PDMS) mold in order to rapidly characterize strain activity within a relay setup. The 3-node and 7-node devices consisted of agar-filled culturing wells connected with an interaction channel. The device lacks the dynamic control of the MISTiC setup, but enabled easy prototyping of relay strains using a simple setup with larger population sizes communicating over longer distances imaged in real-time.

2.1 MISTiC: Mapping Interactions across Space and Time in Communities

A key feature of MISTiC is the physical separation of two microbial strains connected by interaction channels through which signals and metabolites can diffuse between strains (**Figure 2.1**). The growth chambers located on either end of the interaction channel have dimensions of 10 × 50 × 1.5 μm, with a fixed population capacity of approximately 150 cells restricted to a monolayer, enabling single-cell resolution of gene expression and growth. As the population grows and divides, excess cells are washed away by continuous media flow through the connected main channels. The device thus functions as a chemostat for long-term imaging. The interaction channels have lengths of 25, 50, 100, or 250 μm, with a height less than 0.5 μm, and structurally supported by pillars 0.5 μm in diameter. These features serve as a physical barrier for the cells, while permitting diffusion of biomolecules between growth chambers. Each device consists of 10 replicates for each interaction channel length. The symmetry of the microfluidic design balances the pressure across growth chambers and prevents convective flow through the interaction channels. With two inlets connected to each main channel, media conditions can be altered to dynamically modulate the behavior of the strains, monitored in real-time. The MISTiC platform enables us to study the effect of spatiotemporal variables on diffusion-mediated microbial interactions in a tightly controlled microenvironment.

To visualize diffusion and characterize the molecular gradients established across interaction channels in MISTiC, we loaded a small molecule dye, fluorescein, into one of the main channels of the device. Fluorescein diffused from the ‘source’ chambers connected to the main channel, across the interaction channels, and into the sink chambers (**Figure 2.2**). The concentration of fluorescein within the interaction channels decreased as a function of the distance from the source chamber. The average fluorescein concentrations within sink chambers decreased with increasing interaction channel length. This data was used to develop a computational model for diffusion within MISTiC.

2.2 Modeling diffusion in the MISTiC microenvironment

We used the finite-differences method to model diffusion through the MISTiC interaction channels by approximating it as a one-dimensional process and discretizing space in the interaction channels into 1 μm regions. We modeled the concentrations of fluorescein diffusing across interaction channels of varying lengths at rate D_1. Fluorescein is administered through one of the main channels of the device at a concentration of 10 μM. The concentration of fluorescein in the ‘source’ chambers connected to this main channel is represented by

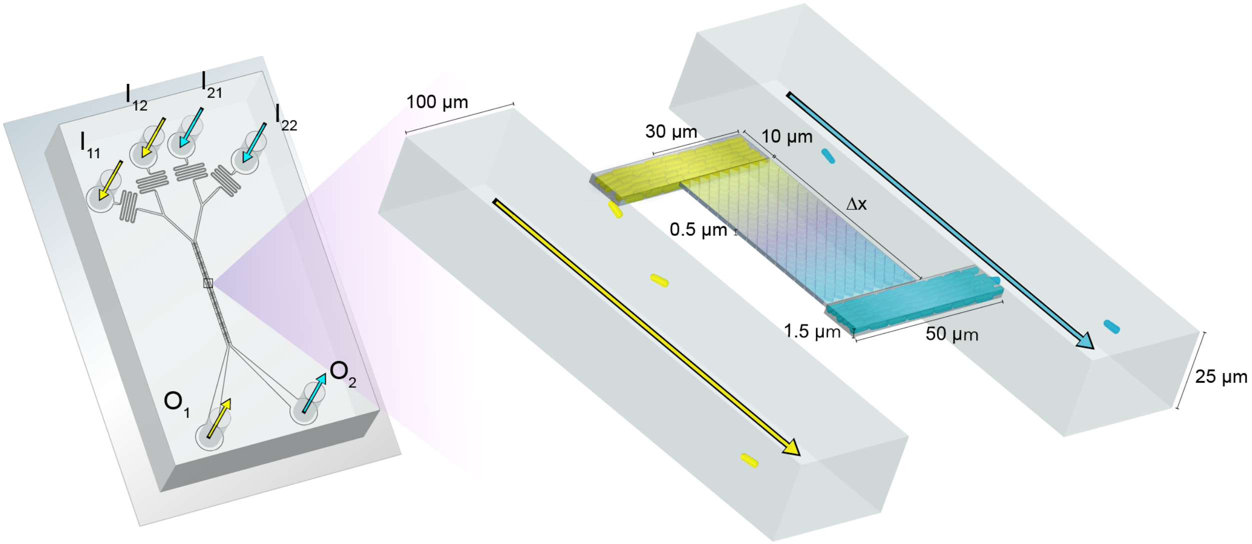

Figure 2.1: Design of a microfluidic platform to investigate the role of spatiotemporal parameters in microbial consortia. Schematic of the microfluidic device. The inlets I_{11}, I_{12} or I_{21}, I_{22} connect to the outlets O_1 or O_2, respectively, and allow temporal control of the environmental conditions. Cells are initially seeded into growth chambers and the continuous flow of media through the main channels removes excess cells. Pairs of growth chambers are separated by a lattice of pillars, defined as the interaction channel, which allows diffusion of biomolecules and prevents cells from entering the interaction channel. The device has ten pairs of growth chambers for each separation distance.

x_1. Since the concentration in each source chamber remains constant, we state that,

$$\dot{x_1} = 0\,. \tag{2.1}$$

The source chambers serve as the point of entry into the interaction channels. For $\gamma_F = 0$, the model exhibits linear chemical gradients that do not mirror the shape of the experimentally measured gradients. (**Figure 2.2**) We thus introduced a linear degradation term for fluorescein, γ_F, to recapitulate the steady-state experimental data. We assume that fluorescein degradation is due to absorption by PDMS or photobleaching. The concentration of fluorescein in each region of the interaction channel is given by,

$$\dot{x_l} = D_1(x_{l-1} + x_{l+1} - 2x_l) - \gamma_F x_l \text{ for } l = 2, 3, ..., L-1\,. \tag{2.2}$$

The ‘sink’ chambers are located on the opposite side of the interaction channels, through which fluorescein dilutes into the second main channel at a rate D_2. Fluorescein concentration in each ‘sink’ chamber is

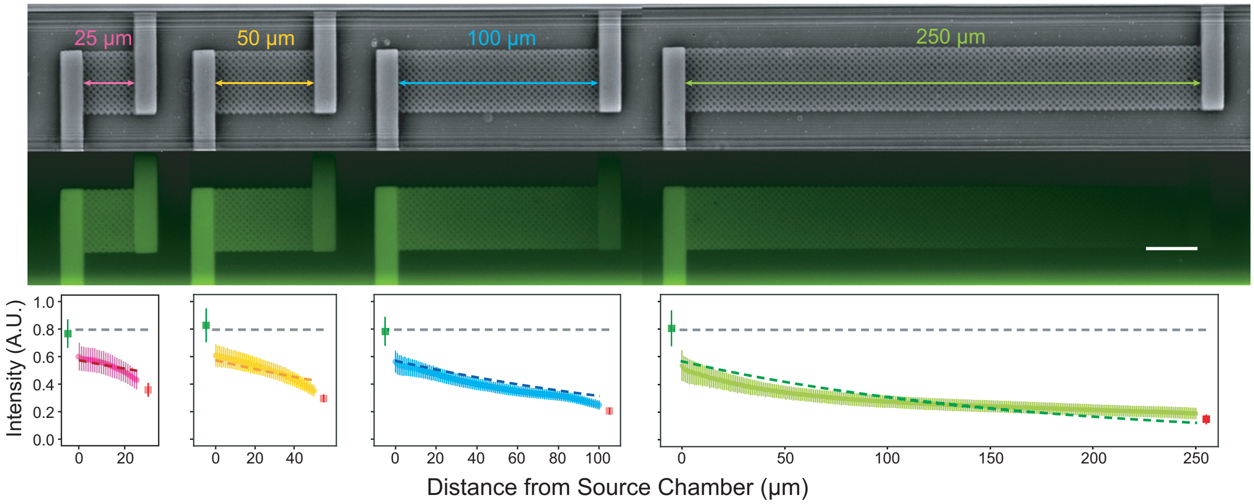

Figure 2.2: Fluorescein dye demonstrates chemical gradients established within MISTiC. Top: Phase contrast and fluorescence microscopy images of the microfluidic device. Fluorescein and water were continuously administered through separate main channels. The scale bar represents 25 μm. **Bottom:** fluorescence intensity in the growth chambers and interaction channels as a function of distance from the source chamber. Green and red squares represent the average intensity within three independent replicates of source and sink chambers, respectively. The difference in the average fluorescence intensity between the 25 μm and 250 μm source channel was not statistically significant ($P = 0.7539$) based on a two-sided t-test. The difference in the average fluorescence intensity between the 25 μm and 250 μm sink channels was statistically significant ($P = 0.0083$) based on a two-sided t-test. The grey dashed line represents the mean fluorescence intensity in the source chambers across the different interaction channel lengths. Dashed lines represent the model fit to the data. Data points represent average fluorescein concentration in 1 μm regions of the interaction channels. Error bars represent one standard deviation from the mean of three independent replicates in different regions of the device. This experiment was repeated twice using slightly different protocols, with similar fluorescein gradients observed across the interaction channels in both experiments.

represented by x_L and is given by the equation,

$$\dot{x_L} = D_1(x_{L-1} - x_L) - D_2 x_L - \gamma_F x_L \,. \tag{2.3}$$

The model parameters (**Table 2.1**) were fit to the fluorescence data within the interaction channel using a nonlinear programming solver (see **Methods** at the end of this chapter).

Parameter	**Description**	**Value**
D_1	Diffusion coefficient of fluorescein across the interaction channel	2.0016 x 10^5 time^{-1}
γ_F	Degradation rate of fluorescein	7.4466 time^{-1}
F_c	Fluorescein concentration in source chamber	0.9135 A.U.
D_2	Diffusion coefficient of fluorescein into main channel	1227.8 time^{-1}

Table 2.1: Estimated parameters for the fluorescein diffusion model.

2.3 FAIRY: Forwarding Amplified Information with RelaY

We designed the FAIRY platform to study relay signaling across spatially separated relay 'nodes' while allowing diffusion-mediated communication between them. Cells are cultured on the surface of 3% agar wells, 3 mm in diameter and 5 mm in depth (**Figure 2.3b**). The culturing wells, or nodes, are arranged in series 10 mm apart and connected to each other by an interaction channel filled with 3% agar of identical composition as the wells. The channel has cross-sectional dimensions of 3 × 2 mm and varying length, proportional to the number of wells. A glass slide seals the surface of the wells where cells are deposited, enabling real-time observation of cell growth and gene expression (**Figure 2.3a**). The FAIRY platform was designed to enable rapid prototyping and testing of relay strains with desired properties at the expense of the dynamic control enabled by microfluidics setups. The geometry of the device and the combinations of strains cultured across the nodes can be readily altered to efficiently characterize various relay signaling configurations and execute spatially programmed logic (**Figure 2.3c**).

2.4 Methods

Microfluidic silicon master fabrication. A three-layer device was designed in AutoCAD that consisted of interaction channels, growth chambers, and main channels. The microfluidic master was patterned in three stages of photolithography using a laser micropattern generator (Heidelberg Instruments μPG 101). Unlike centrifuges, the spin coater protocol used for microfabrication is specified by an rpm. For the first layer, the silicon wafer was baked for 10 min at 200 °C and spin-coated at 4000 rpm using SU-8 2000.5 photoresist (MicroChem) to generate a layer less than 0.5 μm in height. This layer was exposed to the interaction channels micropattern at 58 mW with a 47 % dwell time using a 4 mm writehead, followed by a post-exposure bake for 30 min at 95 °C. The second layer was spin-coated at 3000 rpm using a 26:1 mixture of SU-8 2000.5 to SU-8 3005, to create a height of 1.5 μm. After aligning to the first layer, the wafer was exposed to the second patterning layer consisting of the growth chambers. Following an additional post-exposure bake, a third layer of SU-8 3025 photoresist was spin-coated at 3000 rpm to generate a height of 25 μm. The wafer

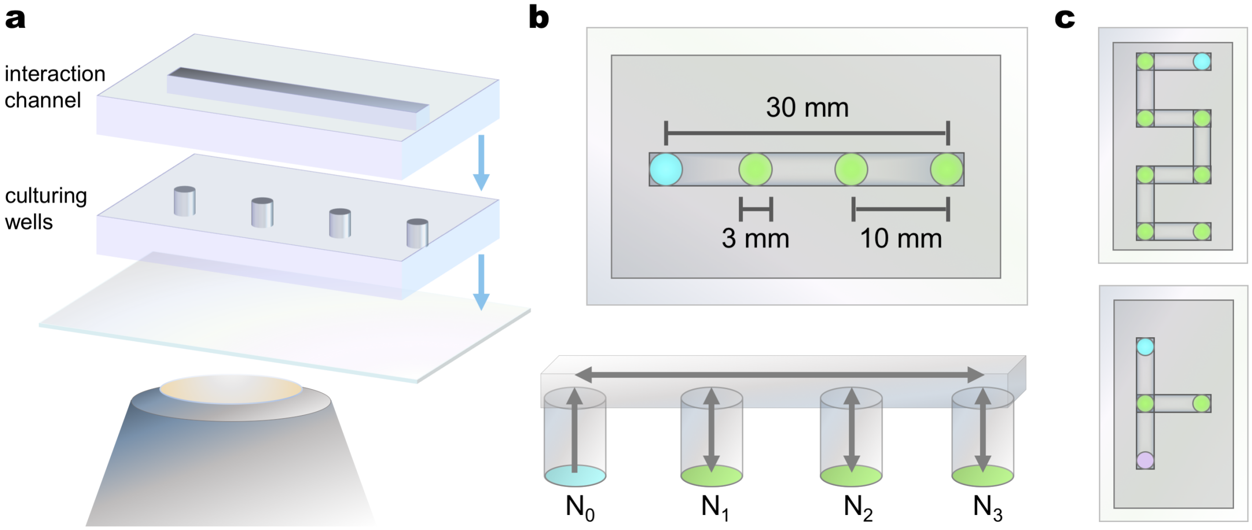

Figure 2.3: A patterned agar device to study diffusion-mediated relay signaling in microbial consortia. **(a)** Depicts the microscopy setup of a FAIRY device. The interaction channel is affixed to one end of the culturing wells, with cells inoculated on the other side of the wells, sandwiched between the agar pad and the glass slide. **(b)** Top- and side-view perspectives of a 4-node relay device in which the signaling cascade is triggered at N_0 and propagates to each subsequent node. Cells, cultured on the bottom of the well, both send and receive information across nodes via signal diffusion through the interaction channel. **(c)** Top: A 7-node relay device to extend the spatial range of microbial interaction. Bottom: A decode-and-forward signaling cascade in which a center node weighs two competing inputs and decides accordingly whether to propagate the signal to a third node.

was exposed to the final layer's pattern consisting of the main channels, resistors, and inlets. Following a final post-exposure bake, the features were developed using SU-8 developer (MicroChem). The master was treated overnight with vapor phase (tridecafluoro-1,1,2,2-tetrahydrooctyl) tri-chlorosilane (Gelest) at room temperature.

Microfluidic chip fabrication. To fabricate each device, a 7:1 mixture of polydimethylsiloxane (Sylgard 184) to curing agent (Sylgard 184) was used to coat the master. After curing overnight at 100 °C, inlet and outlet holes were punched using a biopsy corer (WellTech). The surfaces were exposed to air plasma (Harrick Plasma PCD-32G) for 23 s to ionize the surface of the device to bond to the glass coverslips (ThermoFisher). Finally, the surfaces were bonded and baked for 1 h at 100 °C to seal the device channels. For each experiment, the microfluidic device was flushed with 0.5 % Tween 20 (Sigma-Aldrich) to prevent cells from adhering to the device. To load the cells into the growth chambers, a vacuum pressure of 330 mm Hg was applied.

Fluorescein dye gradient characterization. The chemical gradients in the interaction channels were analyzed by administering 10 μM fluorescein (Sigma-Aldrich) and water at a flow rate of 200 μL/h into individual main channels. Paired growth chambers (n = 3) connected by each interaction channel length were continuously imaged using a 600 ms exposure time. Fluorescence and phase-contrast Images were collected using a Ti-E Eclipse inverted microscope (Nikon) using the GFP filter (Chroma) 470 nm/40 nm (ex), 525/50 nm (em). To analyze the images, the fluorescence of each growth chamber at 1 μm increments along the length of each interaction channel at steady-state were determined.

Model design and fitting. Custom code (MATLAB) was used for computational modeling. The general mathematical form of the equations describing the concentration of fluorescein in each discretized spatial region is

$$\dot{x_i} = D(x_{i-1} + x_{i+1} - 2x_i) - \gamma x_i \, ,$$

where x_i and x_{i+1} represent concentrations in adjacent regions of the device. The parameters D and γ denote the diffusion and degradation rates of the diffusible molecule, respectively. Parameter fitting was performed using the *fmincon* function in MATLAB.

Fabrication of patterned agar devices. The first layer of the device, consisting of the interaction channel pattern, was designed in AutoCAD and 3D-printed with a PETG filament (Prusa i3 MK2). The device was treated overnight with vapor phase ((tridecafluoro-1,1,2,2-tetrahydrooctyl) tri-chlorosilane (Gelest) at room temperature. To fabricate each device, a 9:1 mixture of polydimethylsiloxane (Sylgard 184) to curing agent (Sylgard 184) was poured onto the 3D-printed mold and cured overnight at 65 °C. A clean petri dish was also filled with the same mixture to a height of 0.5 cm and cured overnight at 65 °C. The unpatterned PDMS was cut to fit onto a glass coverslip (ThermoFisher) and punched with a 3 mm biopsy corer (Harris Uni-Core) at measured points designating the locations of the culturing wells. The patterned PDMS mold was aligned and adhered to the PDMS layer embedded with the culturing wells (Gorilla Glue) and allowed to cure for an hour at room temperature. Ultrapure low melting point agarose (ThermoFisher) was dissolved in LB media (Lennox, Sigma-Aldrich) at a concentration of 3%. Upon cooling to approximately 40 °C, the media was supplemented with additional media components required for each experiment and pipetted into the device such that the interaction channel and relay nodes were filled to the brim. Once the media solidified, excess agarose gel protruding from wells was excised. 1 μL of cells at OD 0.05 was spotted onto the surface each well, with strains and configurations varying across experiments. A glass coverslip (ThermoFisher) was placed on top of the wells with gentle pressure applied to adhere it to the PDMS and form a seal around each well.

Chapter 3

Programming Spatial Perception in Microbial Interactions

The spatial proximity of community members is a major determinant of the costs and benefits of microbial interactions, and shapes the evolution of ecological networks [67, 104, 105]. Spatial structure has been shown to provide ecological benefits, such as promoting population survival through local public good production [106, 107], balancing metabolic interdependence [70], and optimizing the ecological productivity of a community [107]. Spatial heterogeneity can also enable coexistence among members of a community by modulating the distribution of positive and negative interactions [97, 108]. The spatial organization of a community can further enhance its resilience by preventing invasion of non-resident strains [109] or enhancing the structural features of biofilms [107]. We do not fully understand the effects of microbial spatial distributions on community functions and stability, or how to manipulate spatial and temporal dynamics to program community properties.

The physical transport of biomolecules mediates the spatial distributions and temporal dynamics of these ecological interactions. Microbes communicate via chemical signals to monitor their population size, coordinate gene expression, and efficiently allocate intracellular resources [80, 83, 110, 111]. The majority of microbial interactions are mediated by diffusible compounds [112], which can enhance or inhibit community member's growth rates [63], as well as modify the activities of intracellular networks [62]. Our microfluidic platform provides a controlled environment to investigate these diffusive processes and their effects on gene expression and community behavior. This experimental data is the basis for a computational analysis through which we aim to identify the important variables involved in encoding spatiotemporal information in microbial gene expression.

3.1 Gene expression profiles of a spatially separated sender-receiver consortium

We investigated the impact of spatial separation on the dynamics of quorum sensing mediated communication between engineered *E. coli* populations. This community consists of a sender strain that produces a quorum sensing signal 3-oxo-C6-HSL (AHL) and a receiver strain that senses the signal and activates a red fluorescent reporter (RFP) (**Figure 3.1**). The sender strain is encoded with an arabinose-inducible AHL synthetase, LuxI, transcriptionally fused to a green fluorescent protein (GFP) to provide a visual readout of AHL synthesis. The receiver strain contains an anhydrotetracycline (aTc)-inducible AHL receptor, LuxR, which binds to AHL to form an activated transcription factor. This complex prompts RFP expression by acting on its cognate promoter, pLuxI (see **Appendix B**).

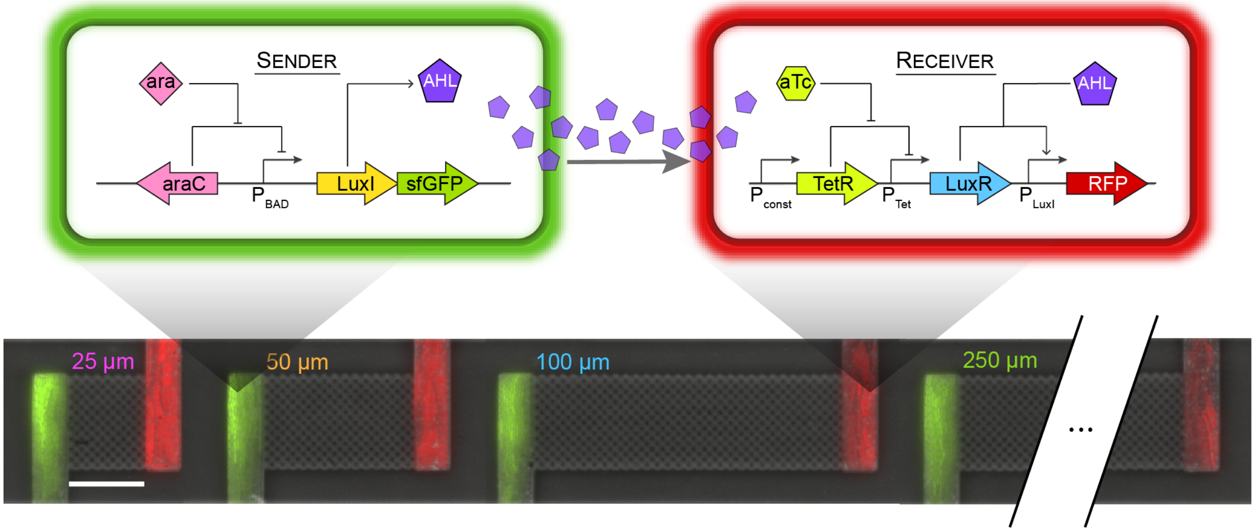

Figure 3.1: Sender and receiver strains communicating within the MISTiC microenvironment. Top: schematic of the genetic circuit in the *E. coli* sender and receiver strains. In the sender strain, the operon containing the synthetase, LuxI, and GFP is induced in response to arabinose. LuxI produces the acyl-homoserine lactone (3-oxo-C6-HSL or AHL), which diffuses through the interaction channel into the receiver strain growth chamber. In the receiver strain, AHL binds to LuxR to form an activated LuxR–AHL complex, which in turn activates expression of RFP driven by a LuxR-regulated promoter. Bottom: overlaid representative fluorescence and phase-contrast microscope images of the sender and receiver strains in the device for each interaction channel length. The scale bar represents 25 μm.

We seeded MISTiC growth chambers with the sender and receiver strains and monitored their gene expression using time-lapse fluorescence microscopy as a measure of inter-strain communication (see Experiment 1, **Appendix A**). After an initial growth phase to allow cells to reach the maximum capacity of each growth chamber, arabinose was administered via the main channel connected to the sender cells. Sender and receiver gene expression dynamics are shown in **Figure 3.2**. Steady-state GFP expression remained unchanged across the length of the microfluidic device with no dependence on the spatial separation of the strains, indicating uniformity in arabinose concentrations within sender growth chambers throughout the device (**Figure 3.2a**). In contrast, the receiver populations' steady-state RFP expression decreased as a function of distance from the sender strain, demonstrating that the receiver gene expression profiles encode positional information at the length scales tested (**Figure 3.2b**).

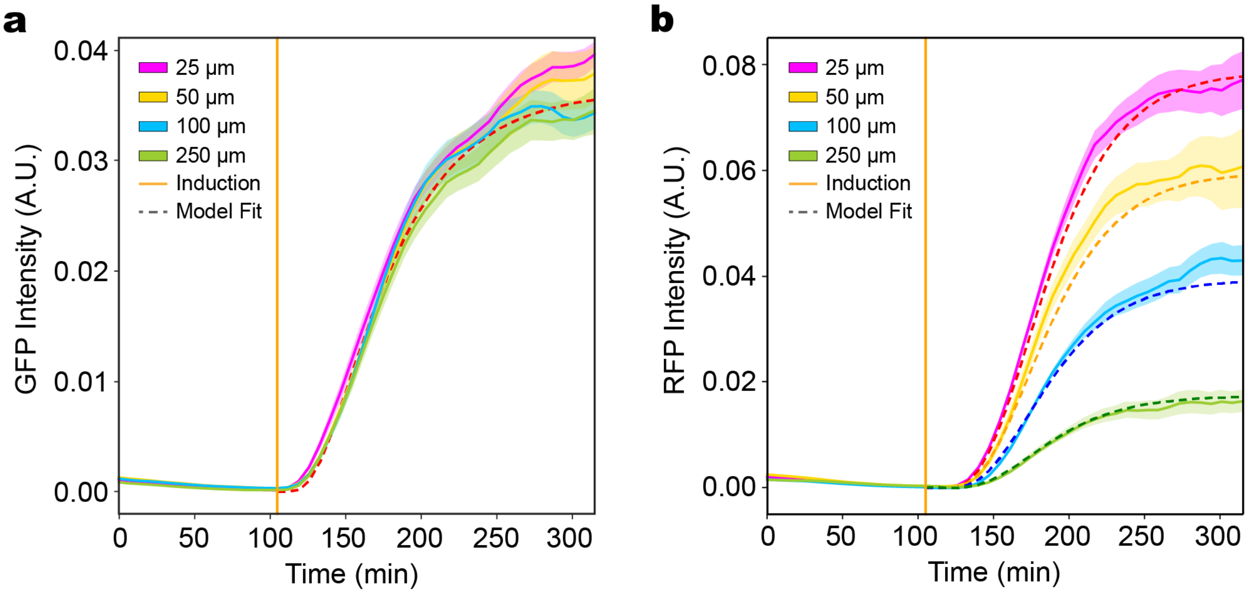

Figure 3.2: Sender and receiver gene expression dynamics. **(a)** GFP fluorescence in sender growth chambers as a function of time. The vertical line indicates the time at which arabinose was introduced. Shaded regions represent one standard deviation from the mean. The dashed line denotes the model fit. **(b)** RFP fluorescence over time in the receiver growth chambers. The vertical line indicates the time at which arabinose was introduced. Shaded regions represent one standard deviation from the mean. The dashed line denotes the model fit.

We measured the time at which RFP expression reached half its maximum value to determine whether delays in RFP dynamics occurred as a function of spatial separation. The RFP response time did not vary significantly with the length of the interaction channel (**Figure 3.3a**). However, this measurement is limited by the frequency of imaging, such that only delays greater than 7 min could be temporally resolved.

To ensure that these results were not influenced by convective flow within the interaction channel or pressure imbalances across the device, the experiment was repeated with inverted orientations of sender and receiver strains (see Experiment 2, **Appendix A**). Similar GFP and RFP dynamics between the experiments (**Figure 3.4**), indicating that the MISTiC microenvironment eliminates confounding variables that may otherwise bias quantitative measurements of circuit behavior.

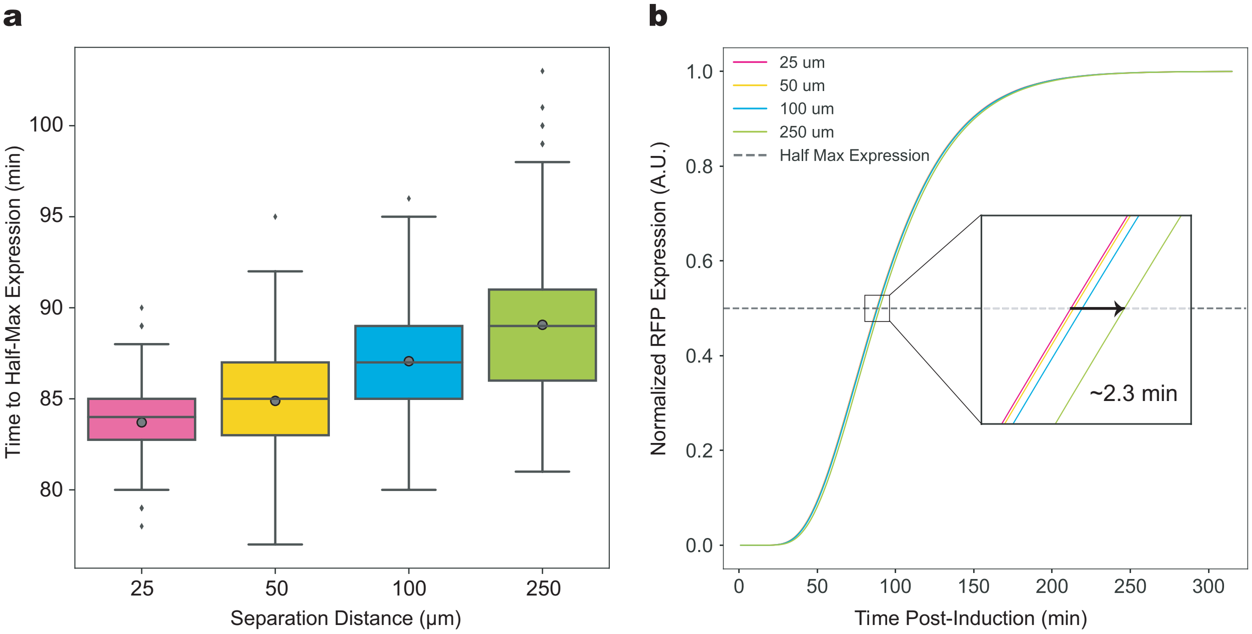

Figure 3.3: Characterization of time delays in quorum-sensing chemical signal communication. (a) Experimentally measured time delays for the quorum-sensing synthetic community as a function of the distance separating the sender and receiver strains. The distributions were computed by bootstrapping the RFP fluorescence as a function of time (1000 resampled curves) (see **Methods**). For each resampled curve, the time delay was calculated by normalizing the curve between 0 and 1 and determining the time to reach half-maximum. Lines and circles within the boxes represent the median and mean of the distributions, respectively. Upper and lower box edges represent upper and lower quartiles, respectively. Upper and lower whiskers represent the 95th and 5th confidence intervals, respectively. **(b)** Normalized model simulations of RFP_p over time for different distances from the sender strain. Increasing the distance from 25 μm to 250 μm resulted in a 2.3 min time delay, computed as the time to reach the half-maximum RFP_p concentration (dashed line).

3.2 A dynamic computational model for inter-microbial communication across distance

To understand the impact of circuit parameters and environmental variables in the diffusion-mediated communication between senders and receivers, we developed an ordinary differential equation model to simulate gene expression dynamics (**Figure 3.5**). The model captures the sequential assembly of LuxI and GFP, followed by AHL synthesis in the senders, and LuxR-AHL binding and the resulting RFP activation and

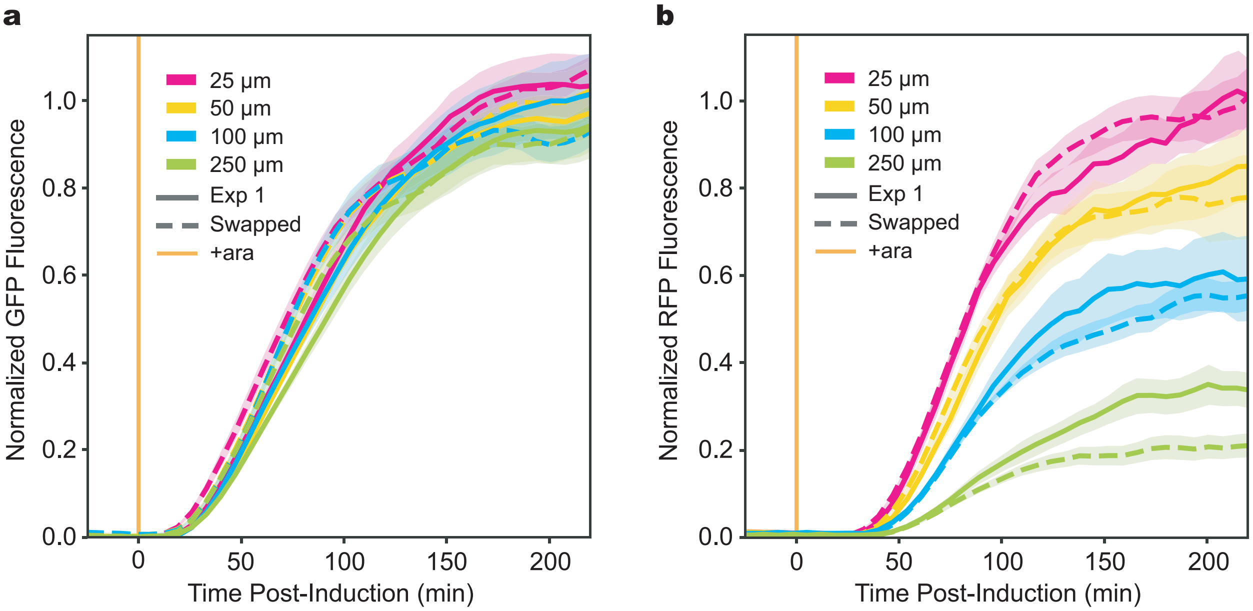

Figure 3.4: Effects of inverting the positions of sender and receiver strains on gene expression profiles. (a) GFP fluorescence in sender growth chambers as a function of time for original (dashed line) and inverted (solid line) chamber positions. The vertical orange line indicates the time at which arabinose was introduced. Shaded regions represent one standard deviation from the mean. Fluorescence intensities are normalized between 0 and 1 to aid direct comparison between experiments. A two-sided t-test demonstrated no statistically significant difference between GFP values observed at steady-state (215 min post-induction) across all separation distances ($P > 0.05$) between the two experiments (see **Appendix A**). **(b)** RFP fluorescence over time in the receiver growth chambers for original (dashed line) and inverted (solid line) chamber positions. Fluorescence intensities are normalized between 0 and 1 to aid direct comparison between experiments. A two-sided t-test demonstrated no statistically significant difference ($P > 0.05$) between RFP values observed at steady-state (215 min post-induction) at 25, 50, and 100 μm distances. A statistically significant difference was observed ($P = 0.01014$) between the two experiments at a separation distance of 250 μm (see **Appendix A**). Potential factors contributing to the difference in steady-states in the 250 μm condition include minor differences in initial growth conditions or experimental setup.

assembly in the receivers. AHL diffusion from senders to receivers is modeled as a one-dimensional process by discretizing space in the interaction channels into 1 μm regions, building on the chemical diffusion model in the previous chapter. In addition, dynamical delays were used to model sequential biochemical reactions and transport of arabinose from the inlets to the growth chambers from time of induction. We used a genetic algorithm to estimate parameters based on time-series fluorescent reporter measurements (see **Methods** at the end of this chapter). Model species are listed in **Table 3.1**, and parameter definitions and values are given in **Table 3.2**.

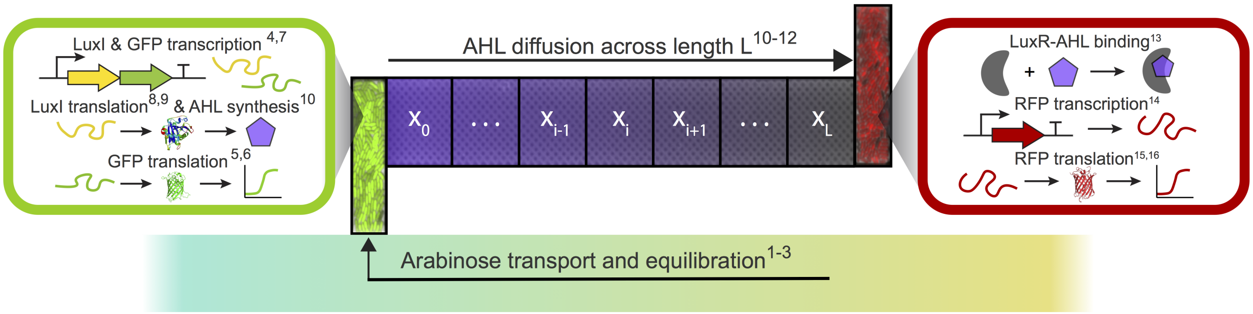

Figure 3.5: Computational model of inter-strain communication in defined spatial environments. Model schematic depicting the physical and biological processes represented by the model equations in this chapter, i.e. the subscript for arabinose transport maps to equations 3.1 - 3.3.

Communication between senders and receivers is chemically induced by switching the inlet supplying media to the main channel to one that contains arabinose. The transport of arabinose throughout the device and its diffusion into the sender growth chambers are represented by the following delay equations:

$$\dot{w_1} = a_1(ara - w_1)\,, \tag{3.1}$$

$$\dot{w_i} = a_1(w_{i-1} - w_i) \text{ for } i = 2 : N_1 - 1\,, \tag{3.2}$$

$$\dot{w_{N_1}} = D_0(w_{N_1-1} - w_{N_1})\,, \tag{3.3}$$

where w_{N_1} represents the concentration of arabinose in the sender growth channel, which prompts the transcription of LuxI and GFP. Because the distinct molecular properties of each protein are associated with a different set of parameters, we model their sequential assembly separately. We begin with the trancription of GFP mRNA, GFP_m, given by the equation,

$$GF\dot{P}_m = \alpha_{LuxI}\frac{w_{N_1}^{n_{LuxI}}}{K_{LuxI}^{n_{LuxI}} + w_{N_1}^{n_{LuxI}}} - \gamma_{GFP}GFP_m\,. \tag{3.4}$$

Species	**Description**
$w_i, i = 1, 2, ..., N_1$	Arabinose concentration in different regions of the device
GFP_m	GFP mRNA
$v_i, i = 1, ..., N_2$	GFP protein intermediates
v_{N_2}, GFP_p	Mature GFP protein
$LuxI_m$	LuxI mRNA transcript
$u_i, i = 1, ..., N_3$	LuxI protein intermediates
$u_{N_3}, LuxI_p$	LuxI protein
$x_i, i = 1, 2, ..., L - 1$	AHL concentration in each region of the interaction channel
x_L, AHL	AHL concentration within the receiver chamber
$LuxRAHL$	Activated complex of $LuxR$ bound to AHL
RFP_m	RFP mRNA
$z_i, i = 1, ..., N_4$	RFP protein intermediates
z_{N_4}, RFP_p	RFP protein

Table 3.1: Species descriptions for diffusion-mediated sender-receiver communication model.

The following equations account for time delays associated with sequential assembly and maturation of GFP:

$$\dot{v_1} = a_2(GFP_m - v_1)\,, \tag{3.5}$$

$$\dot{v_j} = a_2(v_{j-1} - v_j) \text{ for } j = 2 : N_2\,. \tag{3.6}$$

The species v_{N_2} represents the concentration of mature GFP protein in the sender strain. Similarly, LuxI mRNA, $LuxI_m$ was modeled as

$$\dot{LuxI_m} = \alpha_{LuxI}\frac{w_{N_1}^{n_{LuxI}}}{K_{LuxI}^{n_{LuxI}} + w_{N_1}^{n_{LuxI}}} - \gamma_{LuxI}LuxI_m\,, \tag{3.7}$$

with the time delays associated with the translation and maturation of LuxI represented by the equations,

$$\dot{u_1} = a_3(LuxI_m - u_1)\,, \tag{3.8}$$

$$\dot{u_k} = a_3(u_{k-1} - u_k) \text{ for } k = 2 : N_3\,. \tag{3.9}$$

The species u_{N_3} denotes the concentration of $LuxI_p$ in the sender strain. LuxI synthesizes AHL at a rate p_{AHL}, which diffuses into the interaction channel with a diffusion coefficient of D_1 and into the main channel with a diffusion coefficient of D_2. D_2 is significantly lower than D_1 since the diffusion rate through the cells is slower than the diffusion through the media (**Table 3.2**). As AHL is synthesized by LuxI, its concentrations in the sender growth chamber can be represented by the equation,

$$\dot{x_1} = D_1(x_2 - x_1) - D_2x_1 + p_{AHL}u_{N_3} - \gamma_{AHL}x_1 \,. \tag{3.10}$$

The interaction chamber of length L is discretized into approximately 1 μm units, with x_2 and x_{L-1} representing the region closest to the sender growth chamber or receiver growth chamber, respectively. The concentration of AHL in each region of the interaction channel is thus given by,

$$\dot{x_l} = D_1(x_{l-1} + x_{l+1} - 2x_l) - \gamma_{AHL}x_l \text{ for } l = 2, 3, ..., L-1 \,. \tag{3.11}$$

The concentration of AHL in the receiver growth chamber is a balance between diffusion from the interaction channel and diffusion into the main channel and is modeled as

$$\dot{x_L} = D_1(x_{L-1} - x_L) - D_2x_L - \gamma_{AHL}x_L \,. \tag{3.12}$$

In the receiver strain, we assume that the binding of AHL to LuxR is significantly faster than the timescales of transcription and translation. Therefore, based on the quasi-steady-state assumption, the concentration of activated LuxR is modeled as an algebraic equation

$$LuxRAHL = LuxR_{tot}\frac{x_L}{K_{LuxR} + x_L} \,. \tag{3.13}$$

The activated complex $LuxRAHL$ prompts the transcription of RFP mRNA, RFP_m, given by the following equation:

$$\dot{RFP_m} = \alpha_{RFP}\frac{LuxRAHL^{n_{RFP}}}{K_{RFP}^{n_{RFP}} + LuxRAHL^{n_{RFP}}} - \gamma_{RFP}RFP_m \,. \tag{3.14}$$

Finally, we model the time delays associated with the translation and maturation of RFP_p using the equations,

$$\dot{z_1} = a_4(RFP_m - z_1)\,, \tag{3.15}$$

$$\dot{z_m} = a_4(z_{m-1} - z_m) \text{ for } m = 2 : N_4 \,. \tag{3.16}$$

The species z_{N_4} denotes the concentration of mature RFP_p in the receiver strain.

The model accurately recapitulates the dynamics of GFP and RFP across all interaction channel lengths tested (**Figure 3.2**). By running model simulations across a wide range of distances, we characterized the spatial range to be approximately 1000 μm for the signal generated by a population size of approximately 150 sender cells (**Figure 3.6a**). We define the spatial range as the distance at which the RFP_p steady-state falls below 1% of its value when it is unseparated from the senders. The simulations additionally predict that receiver steady-states are highly sensitive to spatial variation when the separation distance is less than 100 μm. The model further enabled a calculation of distance-dependent time delays that could not be

Parameter	Description	Value
ara	Arabinose concentration	0.0619 A.U.
a_1	Time-varying rate coefficient	1.3187 min^{-1}
N_1	Number of delay equations (arabinose)	6
D_0	Diffusion coefficient into growth chamber	0.057 min^{-1}
α_{LuxI}	$LuxI_m$ maximum transcription rate	264.53 A.U. min^{-1}
n_{LuxI}	LuxI Hill coefficient	2.02
K_{LuxI}	$LuxI_m$ half-maximum concentration	33.42 A.U.
γ_{LuxI}	$LuxI_m$ degradation rate	0.046 min^{-1}
N_3	Number of delay equations for LuxI translation & maturation	6
γ_{GFP}	GFP mRNA degradation rate	0.022 min^{-1}
a_2	Time-varying rate coefficient	1.2690 min^{-1}
N_2	Number of delay equations for GFP translation and maturation	15
a_3	Time-varying rate coefficient	0.5607 min^{-1}
D_1	Diffusion coefficient for AHL diffusion into interaction channel	7677.8 min^{-1}
D_2	Diffusion coefficient for AHL diffusion into main channels	251.0 min^{-1}
p_{AHL}	AHL production rate	564.5 min^{-1}
γ_{AHL}	AHL degradation rate	0.086 min^{-1}
$LuxR_{tot}$	Total concentration of LuxR protein	9.5 A.U.
K_{LuxR}	Half-maximum concentration for $LuxRAHL$	54.2 A.U.
α_{RFP}	Maximum transcription rate for RFP_m	184 A.U. min^{-1}
n_{RFP}	Hill coefficient for RFP transcription	1.04
K_{RFP}	Half-maximum concentration for RFP_m	101.3 A.U.
γ_{RFP}	RFP_m degradation rate	0.037 min^{-1}
a_4	Time-varying rate coefficient	0.9195 min^{-1}
N_4	Number of delay equations for RFP translation/maturation	4

Table 3.2: Parameter values for quorum-sensing model. Time delays can be computed as the ratio of the number of delay equations to the time-varying rate coefficient. This yields 6.0 min for arabinose transport from the inlets into the sender growth chambers, 11.8 min for GFP translation and maturation and 4.4 min for RFP translation and maturation.

experimentally resolved. Increasing the separation distance from 25 to 250 μm resulted in a 2.3 min RFP_p response time delay (**Figure 3.3b**), consistent with the expectation of a time delay less than 7 min.

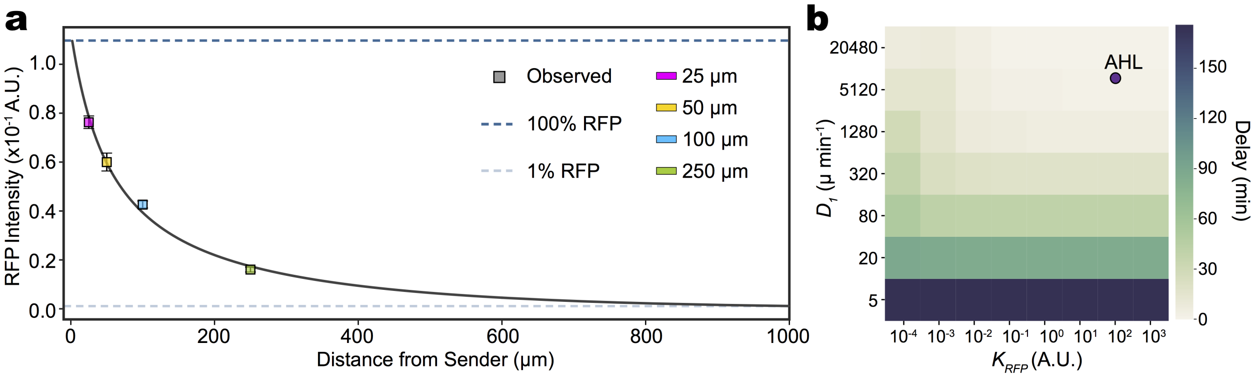

Figure 3.6: Computational predictions for spatial range and temporal delays. (a) The model RFP_p steady-states decrease with the distance from the sender strain. The blue dashed line represents the maximum RFP_p steady-state concentration for a 2 μm interaction channel. The gray dashed line denotes 1% of the maximum steady-state RFP_p concentration. Data points (squares) represent experimental measurements and error bars denote one standard deviation from the mean. **(b)** Heat map of the simulated RFP_p time delays for diffusible signal molecules spanning a broad range of diffusion rates (D_1) and binding affinities of LuxRAHL to the RFP_p promoter (K_{RFP}). The circle represents the estimated parameters based on experimental data.

The diffusion rate of AHL into the main channel, D_2 and the degradation rate of AHL, γ_{AHL}, influence the AHL concentration gradient established within the interaction channel. We used the model to investigate the effects of these parameters on the distance-dependent gene expression pattern (**Figure 3.7**). The absence of AHL dilution considerably altered absolute RFP_p steady-state concentrations and their relative differences across distance. While the absence of AHL degradation alone did not significantly impact receiver gene expression profiles, the simulations indicate that setting both D_2 and γ_{AHL} to zero prevents AHL concentrations from reaching steady-states, thereby saturating gene expression in the receivers and eliminating the spatial differential in RFP gene expression at steady-state. These results demonstrate how the stability of the chemical signal and the physical properties of the environment together dictate the response of a microbial community to spatial separation.

In response to temporally changing environmental stimuli, the allocation of intracellular resources can be optimized by modulating the response times of intracellular networks [113, 114]. Therefore, we explored how the RFP_p response time varies with two key parameters: the diffusion coefficient of AHL through the interaction channel, D_1, and the binding affinity of LuxR-AHL to the RFP promoter, K_{RFP}. The delay in RFP_p increases with decreasing D_1 and remains relatively constant as a function of K_{RFP} (**Figure 3.6b**).

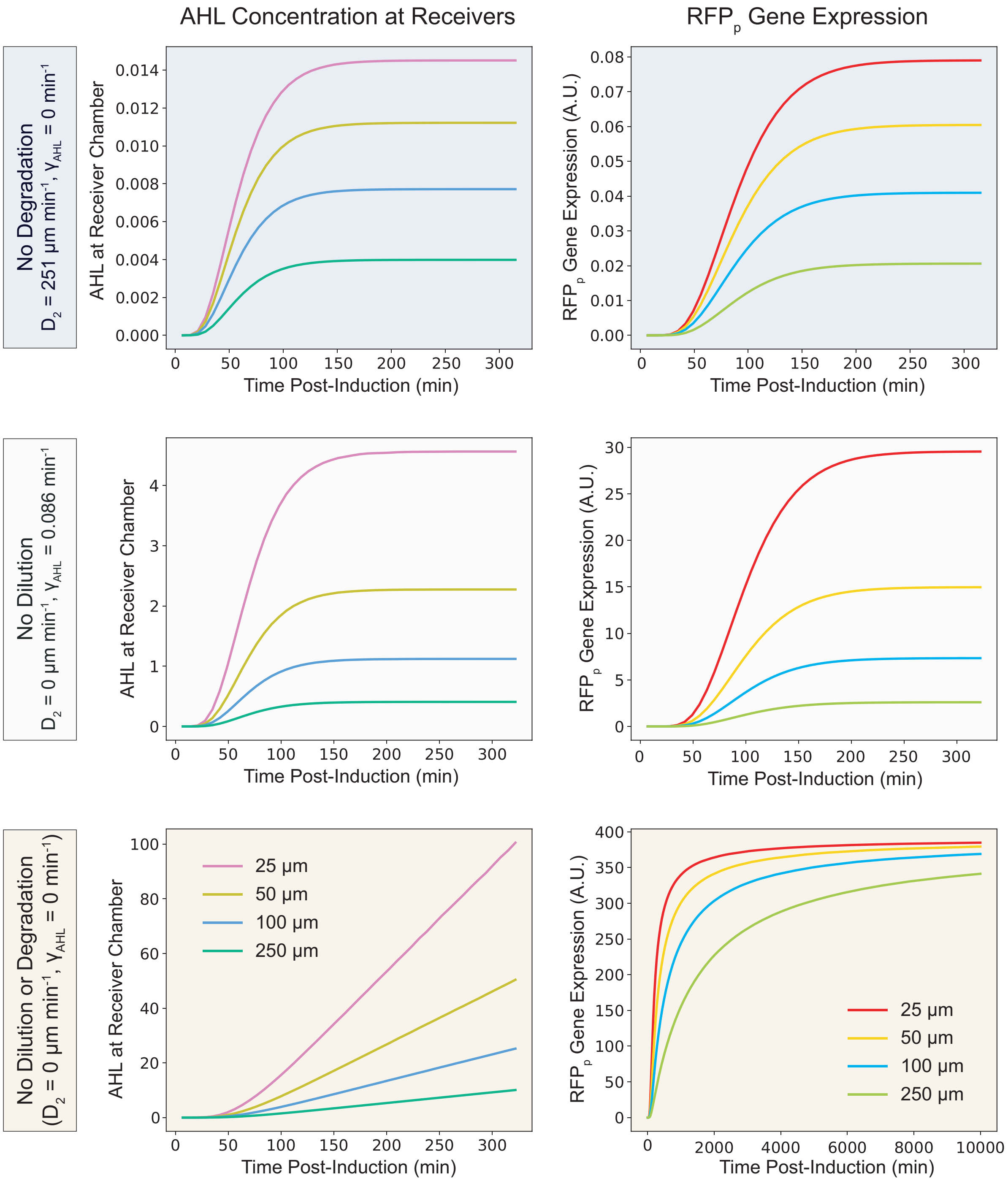

Figure 3.7: Parameter dependence of simulated AHL and RFP_p. Top row: model time-responses of AHL (left column) and RFP_p (right column) where the degradation rate of AHL in the interaction channel is set to zero ($\gamma_{AHL} = 0$). **Middle row:** model time-responses where the diffusion constant of AHL away from the growth chambers into the main channel is set to zero ($D_2 = 0$). **Bottom row:** model time-responses of AHL and RFP_p where $D_2 = 0$ and $\gamma_{AHL} = 0$.

At intermediate values of D_1, the delay is inversely related to K_{RFP}. The estimated parameters for the sender-receiver consortium map to a regime that display small time delays, indicating that a measurable time delay between the 25 and 250 μm conditions would require a large change in D_1.

We analyzed the effects of biochemical parameters on the relative changes in steady-state RFP_p as a function of spatial separation, defined here as distance sensitivity. Changing the binding affinity of LuxR to AHL, K_{LuxR}, and/or K_{RFP} shifted RFP_p expression between the linear and saturated regimes of the AHL dose response curve (**Figure 3.8a**). In response to increasing n_{RFP}, the Hill coefficient for RFP_p production, steady-state RFP_p values exhibit larger relative differences as a function of spatial separation (greater distance sensitivity) (**Figure 3.8b**). This suggests that ultrasensitive circuits could be leveraged to create spatial boundaries in gene expression.

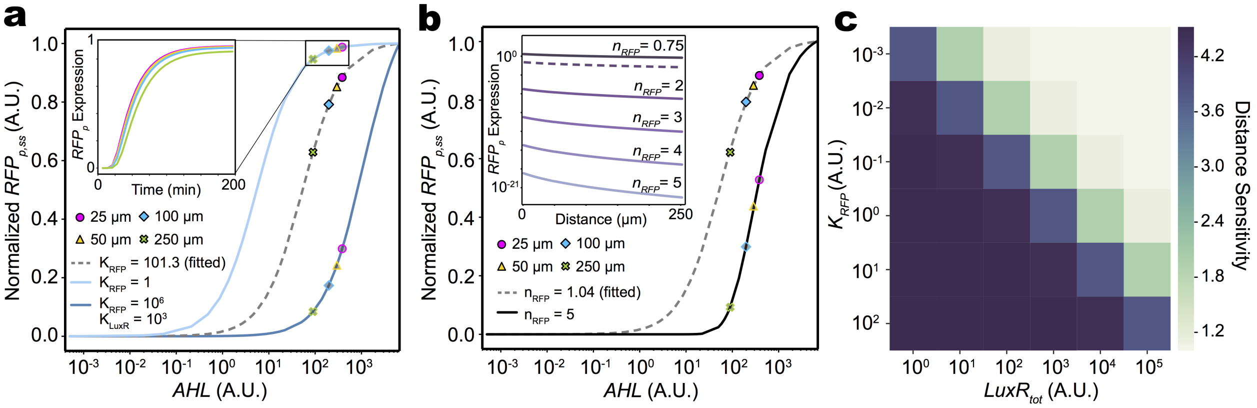

Figure 3.8: The effect of circuit parameters on spatial sensitivity. **(a)** RFP_p steady-state dose response as a function of AHL for different K_{RFP} and K_{LuxR} values. The dashed curve represents the dose response of the parameterized model based on the experimental data. Inset denotes representative simulations of RFP_p for different interaction channel lengths. The RFP_p steady states for each interaction channel length (colored marker styles) were computed for ara = 10. **(b)** Steady-state RFP_p dose response as a function of AHL for two different n_{RFP} values in the model. The dashed curve represents the dose response for the parameterized model based on experimental data. The RFP_p steady-states for each interaction channel length (colored marker styles) were computed for $ara = 10$. Inset: relationship between distance and steady-state RFP_p concentration for a range of n_{RFP} values. **(c)** Heatmap of distance sensitivity across a broad range of total LuxR concentrations ($LuxR_{tot}$) and binding affinities of the activated LuxR complex to the RFP_p promoter (K_{RFP}). Distance sensitivity is defined as the ratio of steady-state RFP_p concentration in a 25 - 250 μm condition.

Model simulations further indicate a correlation between K_{RFP} and $LuxR_{tot}$ with regards to preserving distance sensitivity (**Figure 3.8c**). Whereas the binding affinity, K_{RFP}, is not readily tunable, the correlation indicates that exogenously supplied aTc, which modulates the total amount of LuxR in the cell, can alter differential gene expression across distance. Overall, these results suggest that circuits could be programmed to realize different spatial patterns by modifying distance sensitivity via ultrasensitivity [35,115], the affinity of transcription factors to promoters or a chemical inducer [81], or the concentration of molecular factors within the circuit.

3.3 Methods

Device fabrication. Microfluidic devices for Experiments 1 and 2 were fabricated according to the methods elaborated in **Chapter 1**. Prior to each experiment, the devices were flushed with 0.5% Tween 20 (Sigma-Aldrich) to prevent cells from adhering to the device.

Cell culturing. Sender and receiver plasmids (see **Appendix B**) were constructed using standard Gibson assembly protocols with primers synthesized by Integrated DNA Technologies and verified by Sanger Sequencing (Functional Biosciences). The sender (A6c_LuxI_GFP) and receiver (E2c_LuxR_RFP or pJH9-35) plasmids were transformed into *E. coli* strains BW27783 [116] and MG1655Z1 [117], respectively (see **Appendix B**). An initial set of cultures were inoculated into LB media (Lennox, Sigma-Aldrich) containing 25 μg/mL chloramphenicol (Sigma-Aldrich) and cultured overnight at 37 °C with shaking. After approximately 16 h, 1 μL of the cultures were diluted into 3 mL LB media containing 25 μg/mL chloramphenicol and incubated at 37 °C with shaking to early stationary phase (OD600 0.7–1.1). Next, we measured the OD600 of these cultures and centrifuged 1 mL at 3500 × g. The supernatant was removed and the pellet was resuspended to a final OD600 of approximately 20.

MISTiC setup. To load the cells into the growth chambers, the resuspended pellet was connected to the inlets and a vacuum pressure of 330 mm Hg was applied to the outlets. Cells were loaded into the device such that each growth chamber had at least two to three cells at the beginning of the experiment. In each experiment, the device was connected to three syringes (5 mL) containing LB media supplemented with 25 μg/mL chloramphenicol, 0.1% Tween 20 (Sigma-Aldrich), and 62.5 ng/mL anhydrotetracycline hydrochloride (Cayman Chemicals), as well as a fourth syringe (5 mL) containing the same media supplemented with 0.1% arabinose (Sigma-Aldrich). During the microscopy experiment, the microfluidic device was incubated at 37 °C in a custom-designed temperature incubation chamber. The main channels were flushed at a rate of 300 μL/h to wash away excess cells from the growth chamber. The flow rate of the inlet containing arabinose (I_{22}, **Figure 2.1**) and the corresponding inlet on the opposite side (I_{11}) were set to 10 μL/h to prevent cell growth and clogging within the inlet and resistor and to reduce pressure differences across the device. Fluorescence and phase-contrast images were collected using a Ti-E Eclipse inverted microscope (Nikon) every 7 min at 21 different positions. Fluorescence was imaged using the following filters (Chroma): GFP: 470 nm/40 nm (ex), 525/50 nm (em) or RFP: 560 nm/40 nm (ex), 630/70 nm (em). The device was incubated for a period of time to allow cells to grow and divide. After the growth chambers had filled with cells, the media was switched to test conditions described in **Appendix A**. For Experiments 1 and 2, the outer inlets I_{22} and I_{11}, one of which contained arabinose, were switched to 200 μL/h and the flow rate through the remaining inlets, I_{12} and I_{21} were set to 0 μL/h (**Figure 2.1**).

Image segmentation. For Experiment 1, individual growth chambers were segmented in DeepCell [118]. Five neural networks were trained on 21 randomly selected images and binary masks (made using FIJI image analysis software [119]), which specified the growth chamber positions. The trained model was used to analyze the remaining microscopy images. The results of the trained networks (two to five depending on segmentation accuracy) were averaged to improve segmentation accuracy. For Experiment 2, growth chambers were segmented using custom code in Python that aligned each growth chamber across all time points. A binary mask denoting the growth chambers was applied to all time points. The DeepCell and alignment methods generated nearly identical fluoresence time-series data.

Image analysis. In each analyzed image, custom code (Python) was used to label the binary mask with the growth chamber positions and total areas and compute the average fluorescence intensity of each growth chamber. Segmented regions less than or greater than 1000 and 3500 pixel area were eliminated from the data set. Specific criteria were used to eliminate outliers from the datasets including (1) infrequent pressure fluctuations leading to loss of cells from the growth chambers, (2) device bonding issues leading to collapsed interaction channels or cells that enter the interaction channels, (3) growth chambers with unoccupied regions, (4) abnormal cell growth that significantly altered the total number of cells in the growth chamber, or (5) cell growth in the main channels that may have generated different media diffusion rates into the growth chambers. In all experiments with interacting physically separated cell populations, the connected chamber was excluded from the data set if a growth chamber was identified as an outlier based on these criteria (see **Appendix A**). In Experiment 1 and 2, background fluorescence was eliminated by subtracting the minimum RFP fluorescence intensity across all growth chambers for model fitting and time-series data was normalized to facilitate comparisons between experiments.

Statistical analysis. P-values for bootstrapped datasets were computed by bootstrap hypothesis testing. Here, the null hypothesis H_0 assumes that a sample of size n with mean x^*_{obs} and a sample of size m with mean y^*_{obs} are derived from the same population. This test is performed as follows:

1) Calculate the sample mean difference, t^*_{obs} as $t^*_{obs} = x^*_{obs} - y^*_{obs}$

2) Merge two samples into one set of $n + m$ observations.

3) Draw a bootstrap sample of $n + m$ observations with replacement from the merged set.

4) Calculate the mean of the first n observations, x^* and compute the mean y^* for the remaining m observations in the bootstrap sample. The test statistic t^* is evaluated as $t^* = x^* - y^*$.

5) Repeat steps 3 and 4 B times where $B \geq 1000$.

6) Evaluate the P-value as: P-value = number of times where $t^* > t^*obs$ divided by B.

7) Reject H_0 if P-value $\geq \alpha$, where $\alpha = 0.05$.

Computational modeling. Custom code (MATLAB) was used for computational modeling. The general mathematical form of the equations describing the concentration of AHL or fluorescein in each discretized spatial region is

$$\dot{x_i} = D(x_{i-1} + x_{i+1} - 2x_i) - \gamma x_i \,,$$

where x_i and x_{i+1} represent concentrations in adjacent regions of the device. The parameters D and γ denote the diffusion and degradation rates of the diffusible molecule, respectively. For the gene expression model, the general mathematical form for modeling transcription is

$$\dot{B_m} = \alpha_B\left(\frac{A^n}{K^n + A^n}\right) - \gamma B_m \,,$$

where A and B_m represent a transcription factor and its regulated transcript, respectively. The parameters α_B, n, K, and γ denote the maximum transcription rate, Hill coefficient, half-maximum concentration or binding affinity and mRNA degradation rate, respectively. The general mathematical form for representing time delays due to sequential protein assembly, fluorescent protein maturation or media switching is

$$y_j = a(y_{j-1} - y_j) \text{ for } j = 1 : N \,.$$

The species y_N represents the time-delayed species y_1 and the delay time is computed by $N \cdot a^{-1}$.

Parameter estimation. The model was simulated using *ode23s* (MATLAB). A model with a variable number of delay equations was fit to the data using a genetic algorithm. The algorithm identified a best estimate for the parameter values and an optimal model structure by adjusting the number of delay equations to minimize the L^2-norm between the model and the data. First, 100 parameter sets were randomly sampled using an upper and lower bound for each parameter. For each parameter set, the model was simulated and the L^2-norm between the model and the data was computed. The parameters were ranked from lowest to highest L^2-norm. The first parameter set (lowest L^2-norm) was averaged with parameter sets 2-10, generating 9 new parameter sets. These parameter sets were combined with 81 randomly sampled parameter sets using an upper and lower bound for each parameter. This procedure was repeated until the L^2-norm did not change significantly with additional iterations. The best estimates for the parameters are listed in **Table 3.2**.

Chapter 4

Transferring Information with Oscillatory Dynamics

Periodic signals are a frequent occurrence in biological systems on every scale, from the molecular [120] to the ecological [121]. Oscillatory behavior allows cells to simultaneously encode several layers of information into a single signaling mechanism. For instance, using fold-change detection cells can respond to changes in a signal rather than its baseline magnitude [122]. By transducing the duration of a signal to different levels and types of output responses, cells can selectively expend energy to respond only to sustained signals [123]. Information can also be encoded in the frequency domain to generate noise-gated, thresholded responses and to synchronize gene expression across many components [124, 125]. Periodic gene expression patterns can also carry functional information that reflects the spatiotemporal patterning of upstream processes [126]. In this chapter, I characterize the periodic behavior of a dual-feedback oscillator to determine how the spatial separation of gene circuit components impacts the temporal coordination of gene expression across the two strains.

Beyond their signaling functions, oscillations in gene expression may simply be a consequence of circuit topology [19]. As such, the dynamic gene expression profile can be analyzed to infer the logic of the underlying gene regulatory network [120]. Notably, the same principle applies even when oscillatory behavior is not an intrinsic feature of the system, but is instead externally driven [127]. In either case, the input signal is compared to the dynamics of the output to deduce the regulatory processes responsible for the observed signal transformation [128]. The advantage of driving oscillations externally is that the input signal can be crafted to ‘scan’ regimes that can reveal the bounds, or the processing limits, of the system. For instance, it is known that protein concentrations fluctuate over the course of a cell cycle [94], and that gene expression is prone to sporadic bursts in transcription [129] and translation [130]. The time-scales of these potential sources of interference can define the limits of the temporal responsiveness of the system. In this chapter, forced oscillations are applied to the sender-receiver consortia at different frequencies to determine the effects of spatial separation on the speed and accuracy of signal processing in the system.

4.1 Forced oscillations in a sender-receiver consortium

We applied a periodic input to the sender-receiver consortium to characterize how distance impacts information transmission in fluctuating environments. We used the computational model fit to the step-wise response in the previous chapter to simulate system behavior with square wave oscillations in arabinose (ara) with a period of 2 h. Model predictions show the steady-state amplitude and mean RFP_p decreasing with increasing spatial separation (**Figure 4.1a**). We tested these predictions by exposing the sender-receiver consortium to alternating arabinose concentrations between 0 % and 0.1 % with a period of 2 h (see Experiment 3, **Appendix A**). In response to the oscillatory signal, both GFP and RFP mean intensities increased over time and reached a steady-state oscillatory phase (**Figure 4.1b,c**). The periods of GFP and RFP were synchronized with the arabinose input and therefore did not vary with distance (**Figure 4.2a**). The GFP mean and amplitude did not vary across distance (**Figure 4.1b** and **Figure 4.2b**). Mirroring the model prediction, the RFP mean and amplitude decreased as a function of distance (**Figure 4.1c** and **Figure 4.2b**). At steady-state, the mean activation and decay response times of GFP and RFP were 30 - 40 min across all distances (**Figure 4.3**). These response times are slightly greater than the exponential phase doubling time of *E. coli* in Luria Broth (LB) media [131], suggesting that fluorescent protein dilution due to cell division influences the observed decay rate.

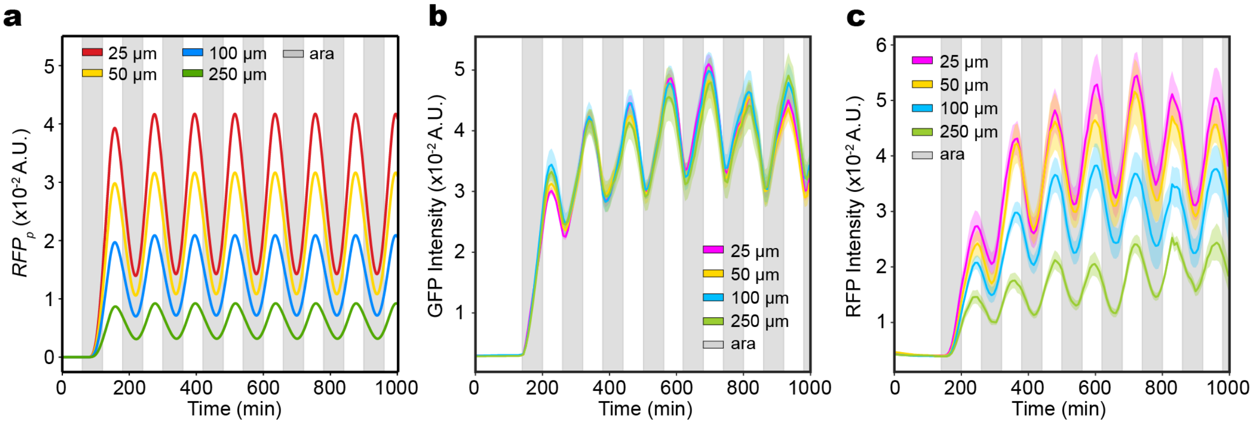

Figure 4.1: Forced sender-receiver oscillations at a period of 2 h. **(a)** Model simulations of RFP_p in response to a periodic arabinose input (2 h period). Gray shaded regions denote the presence of arabinose. **(b)** GFP as a function of time in response to an oscillatory arabinose input (2 h period). Gray shaded regions denote the presence of 0.1% arabinose. Colored shaded regions represent one standard deviation from the mean. **(c)** RFP as a function of time in response to a periodic arabinose input (2 h period).

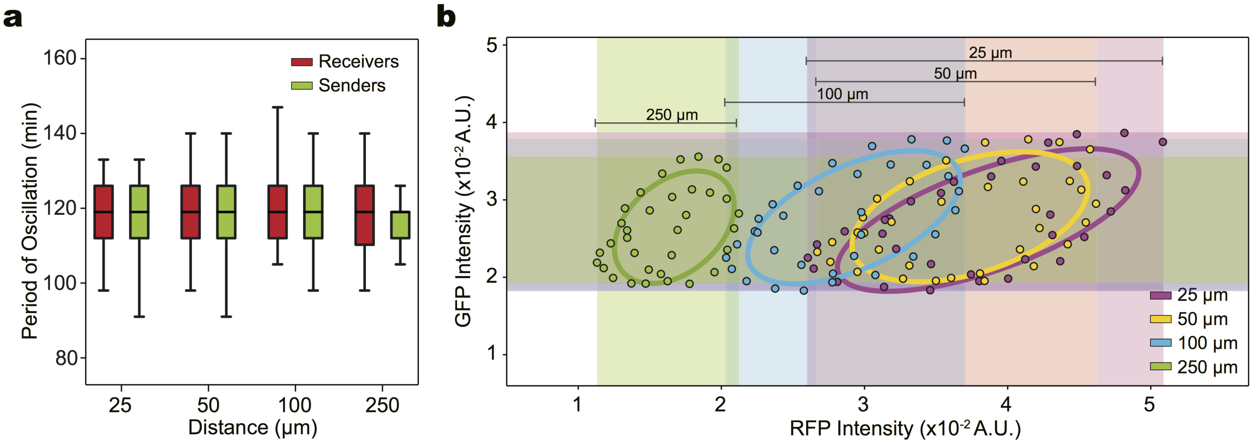

Figure 4.2: Effects of spatial separation on the period and amplitude of forced oscillations in the sender-receiver system. **(a)** Box plots of the experimentally measured distribution of oscillatory periods, determined by applying a peak finding algorithm to time-series RFP (receivers) or GFP (senders) data for all cell growth chambers. The period was measured as a 2 h oscillation (defined as 1 h exposed to arabinose and 1 h in the absence of arabinose) between 304 to 1004 min. Horizontal lines within boxes indicate the median and upper and lower box edges represent the upper and lower quartiles, respectively. Upper and lower whiskers represent the 95th and 5th confidence intervals, respectively. A two-sided t-test of oscillatory periods across distance showed no statistical significance ($P > 0.05$) **(b)** Phase plot of RFP vs. GFP for two oscillatory periods from 580 to 700 min for a forced oscillation experiment with an arabinose period of 2 h.

The aggregation of various sources of noise within cells creates significant fluctuations in protein production rates over the time scale of a cell cycle, suggesting a tradeoff between the accuracy and speed of information processing in transcriptional responses [94]. Given that the GFP and RFP periods matched that of the driving input, the GFP and RFP outputs at a 2 h period may reflect the temporal averaging of stochastic processes within the cells. We hypothesized that driving oscillations near a critical input frequency might corrupt information propagation within the sender-receiver system [94]. To test this, we measured gene expression in senders and receivers in response to an alternating arabinose input with a period of 1 h (see Experiment 4, **Appendix A**). Model simulations for these conditions predicted a distance-dependent change in steady-state RFP_p with lower means and amplitudes than those predicted for the 2 h periodic input (**Figure 4.4a**). Experimentally applying arabinose at a 1 h period yielded steady-state GFP oscillations at lower amplitudes compared to those observed in the 2 h oscillator. No trend in mean GFP expression was

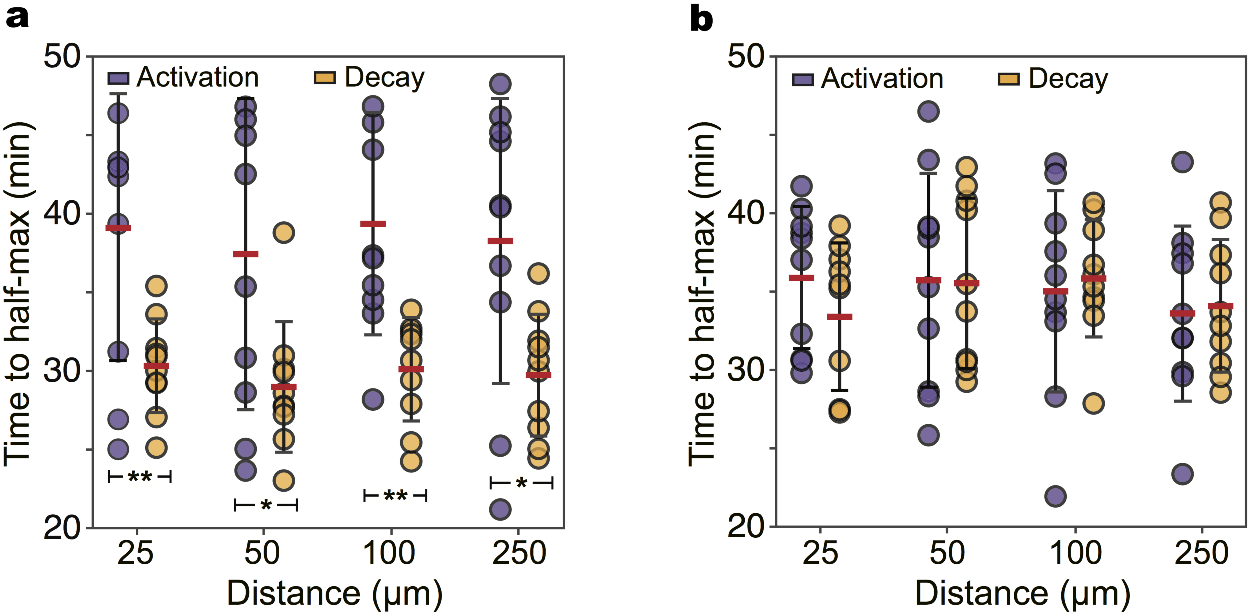

Figure 4.3: Response times of sender-receiver strains during forced oscillations with a period of 2 h. **(a)** Activation and decay response times for GFP (sender strain). Activation response time is defined as the time to reach half-maximum from the minimum to the maximum of each period. The decay response time is defined as the time to reach half-minimum from the maximum to the minimum of each period. Error bars represent one standard deviation from the mean. Horizontal bars with stars indicate a statistically significant difference ($P < 0.05$) based on a two-sided t-test. One star (*) indicates $P < 0.05$, two stars (**) indicate $P < 0.01$, and three stars (***) indicate $P < 0.001$. The P-values for the 25, 50, 100 and 250 μm conditions are 0.0064, 0.0229, 0.0015 and 0.0135, respectively. **(b)** Activation and decay response times for RFP (receiver strain). Error bars represent one standard deviation from the mean. A two-sided t-test between activation and decay times showed no statistical significance ($P > 0.05$)

observed as a function of spatial separation (**Figure 4.4b**). RFP expression displayed a distance-dependent change in steady-state fluorescence intensity, as well as lower amplitudes and irregular variability around the mean during steady-state oscillations compared to the 2 h oscillator (**Figure 4.4c**).

Taken together, the model simulations and both sets of experimental data show that distance or higher input frequencies attenuate the amplitude of RFP expression (**Figure 4.5a**). In the 1 h experiment, RFP amplitudes no longer varied as a function of distance, indicating that at higher frequencies, positional information is encoded in the mean of the signal and is not resolvable by differences in amplitude. Assuming

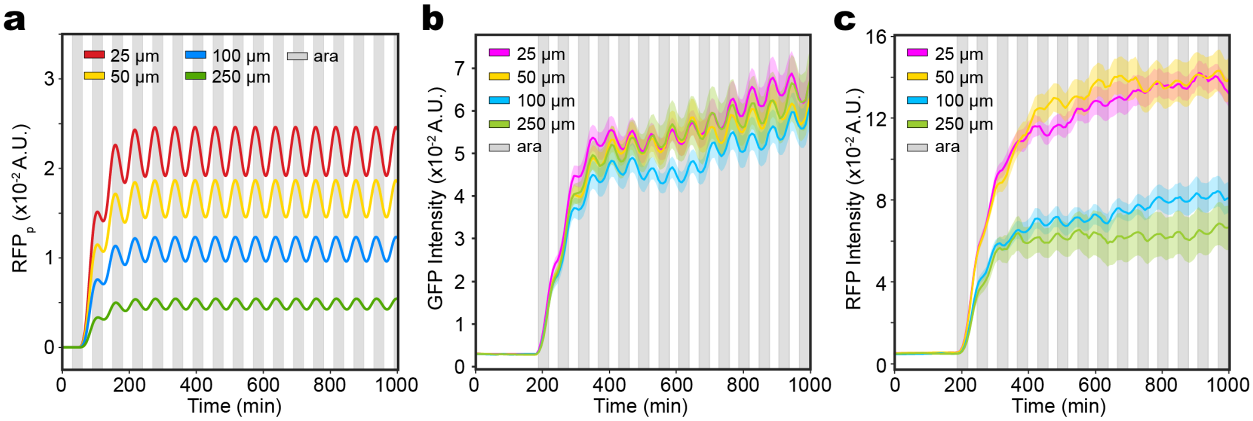

Figure 4.4: Forced sender-receiver oscillations at a period of 1 h. **(a)** Model simulations of RFP_p in response to a periodic arabinose input (1 h period). Gray shaded regions denote the presence of arabinose. **(b)** GFP as a function of time in response to an oscillatory arabinose input (1 h period). Gray shaded regions denote the presence of 0.1% arabinose. Colored shaded regions represent one standard deviation from the mean. **(c)** RFP as a function of time in response to a periodic arabinose input (1 h period).

that fluctuations in a signal can be detected only above a threshold amplitude, A_c, RFP amplitudes of low frequency fluctuations will remain above this threshold at longer distances compared to higher frequency fluctuations (**Figure 4.5a**). These results indicate that distance establishes a low-pass filter in diffusion-mediated signal propagation and can insulate the system from transient signal fluctuations. Our model further shows that increasing n_{RFP} augments the relative differences in RFP amplitudes across distance as a function of the input period (**Figure 4.5b**), sharpening the cut-off point of the low-pass filter. Every gene regulatory network has an inherent speed limit for signal processing [93]. Our results show that the frequency limit for signal processing within a GRN can be tuned by varying the spatial arrangement of its components.

Communication between physically separated populations is impacted by extracellular noise due to diffusion [95] and noise from intracellular processes such as transcriptional [129] or translational bursting [130]. Forced oscillations near a critical input frequency can also interfere with intracellular fluctuations, contributing to noise in gene expression [94]. For insight into these contributions to signal dynamics we investigated how information is encoded in the frequency domains of the gene expression responses. The power spectrum represents how the variance in gene expression is distributed across frequencies. For a forced oscillator at constant frequency, we expect to see a peak in the power spectrum at the frequency of the driving input. The power spectrum for GFP and RFP displayed prominent peaks at the frequency of the input signal for both

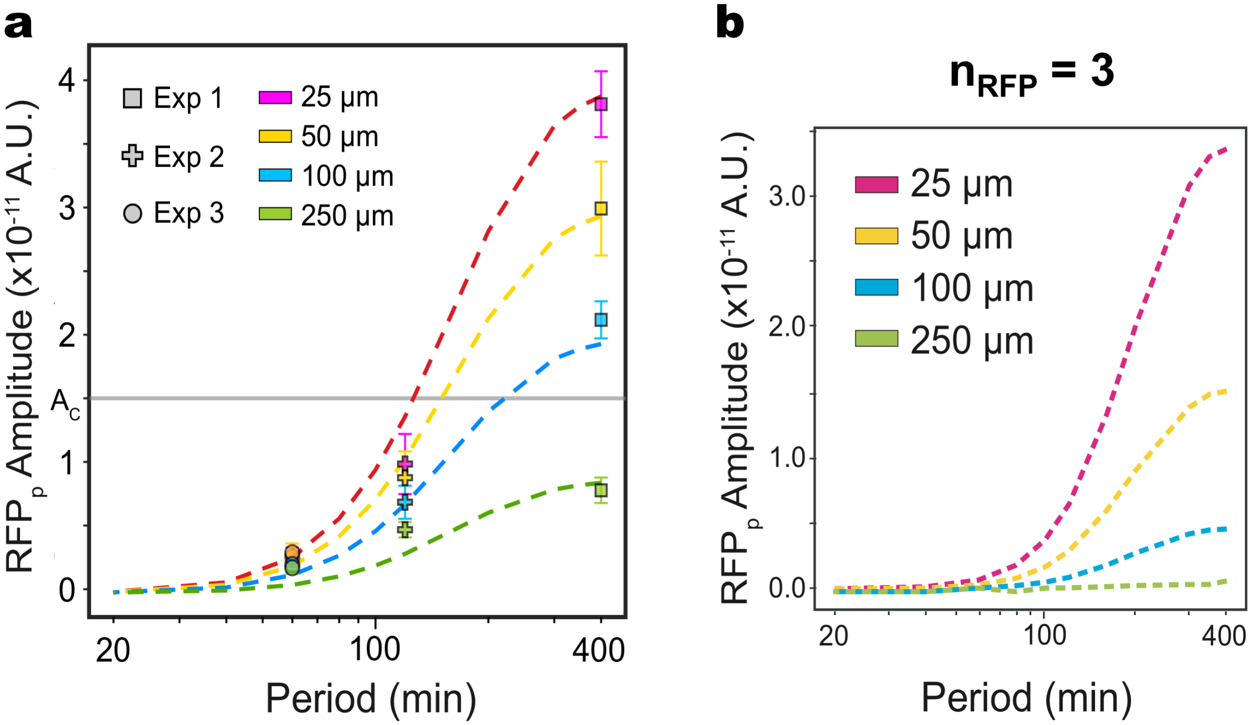

Figure 4.5: RFP amplitude as a function of the input period at different distances. **(a)** Square, plus, and circular data points represent the amplitudes in the step response, 2 h and 1 h forced oscillator experiments, respectively. Error bars represent one standard deviation from the mean amplitude. Dotted lines represent model simulations of RFP_p steady-state amplitude in the model with fitted parameters for different distances from the sender strain. **(b)** Dotted lines represent model simulations of RFP_p steady-state amplitude in the model for $n_{RFP} = 3$ for different distances from the sender strain.

experiments (**Figure 4.6a** and **Figure 4.7a**). The peak corresponding to the input frequency in the GFP power spectra for both experiments showed no trend with distance (**Figure 4.6a**). The major peak in the RFP power spectrum at the input frequency decreased with distance in the 2 h forced oscillation experiment (**Figure 4.7a,** top), reflecting the trend in amplitude across distance, with no trends observed outside the signal bandwidth. In response to a 1 h period, the RFP power spectrum shows a distance-dependent trend in power spectrum frequencies outside the signal bandwidth (**Figure 4.7a,** bottom).

To evaluate the fidelity of information transmission across distance, we defined the signal-to-noise ratio (SNR) as the total power of the input signal bandwidth divided by the total power across all frequencies greater than the signal bandwidth (see **Methods** at the end of this chapter). The GFP SNR did not vary as a function of spatial separation in either of the forced oscillator experiments ((**Figure 4.6b** and

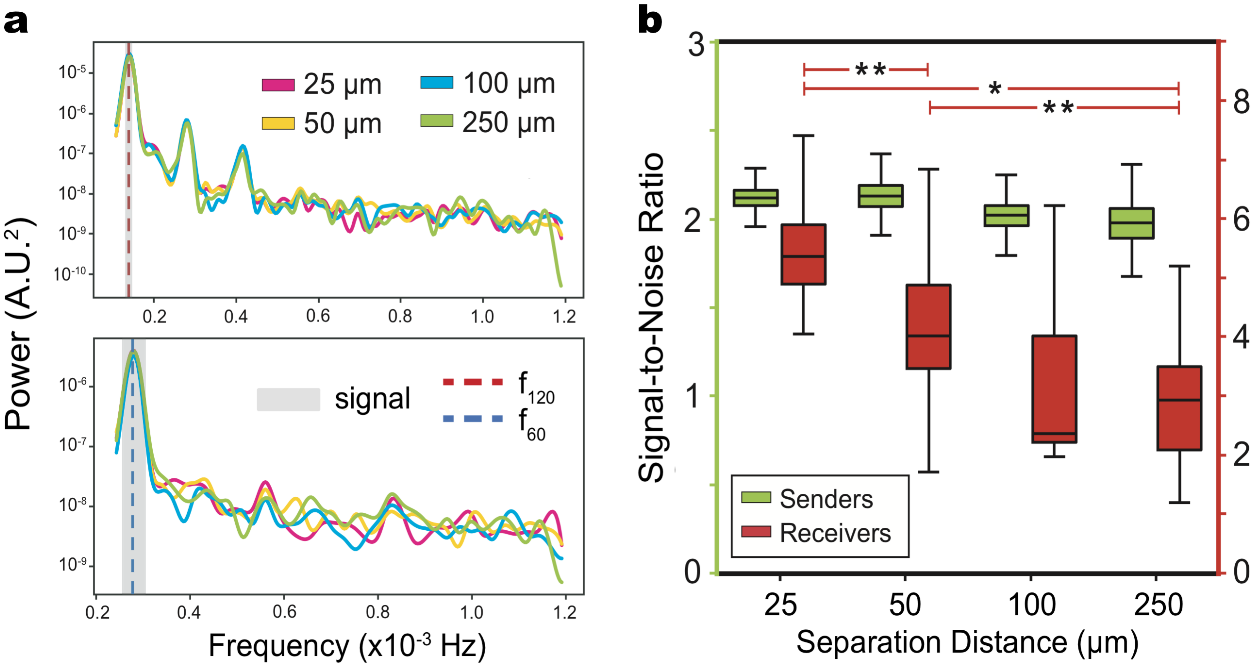

Figure 4.6: GFP power spectra and signal-to-noise trends for 2 h oscillator. **(a)** Top: Mean power spectra of GFP (sender strain) in response to an oscillating input with a period of 2 h (red dashed line). Power spectra were calculated using the Welch method with a Hamming windowing function at steady-state for 395–1536 min (see **Methods**). The gray shaded region denotes a bandwidth of ±10 min around the expected input frequency. Bottom: Mean power spectra of GFP (sender strain) for the forced oscillation experiment input period of 1 hr. Power spectra were calculated using the Welch method with a Hamming windowing function at steady-state for 500–1249 min. The arabinose frequency is represented by a dashed red line. The gray shaded region denotes a bandwidth of ±5 min around the expected input frequency. **(b)** Signal-to-noise (SNR) ratios computed using bootstrapped power spectra for GFP or RFP for each distance in the 2 h forced oscillator experiment. Left and right axes denote SNR for GFP and RFP, respectively. Horizontal lines within boxes denote the median and upper and lower edges represent the upper and lower quartiles, respectively. Upper and lower whiskers represent the 95th and 5th confidence intervals, respectively. Horizontal lines with stars denote a statistically significant difference ($P < 0.05$) based on one-tailed bootstrap hypothesis testing. $*P < 0.05, **P < 0.01$, and $***P < 0.001$ (see **Appendix A**).

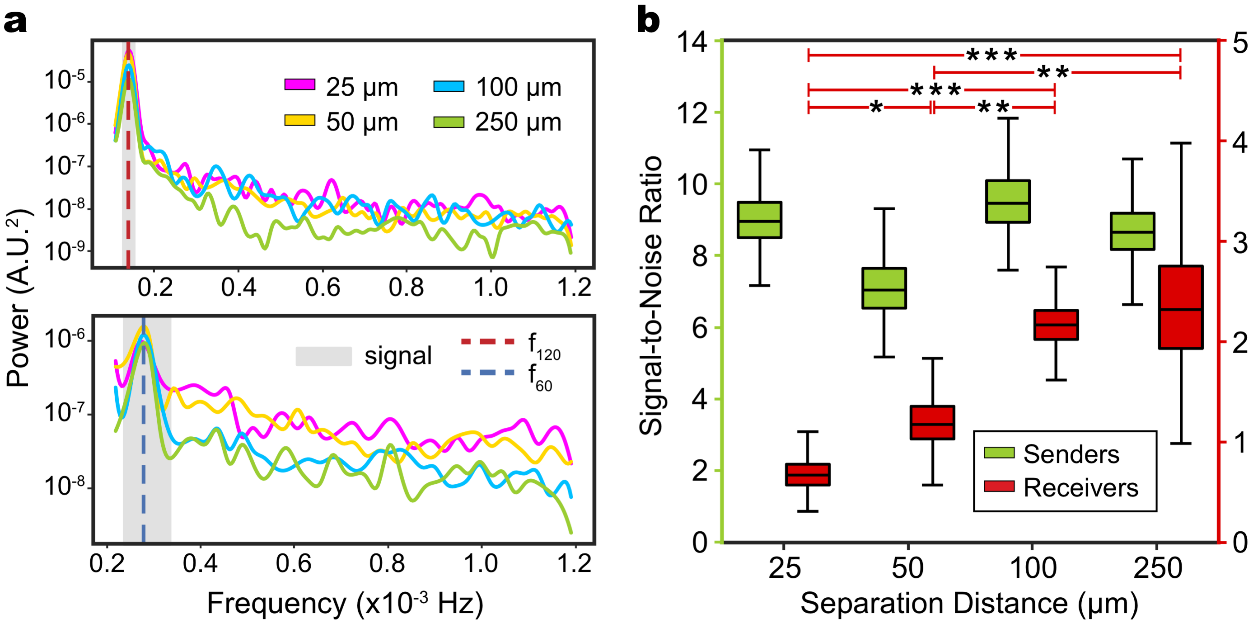

Figure 4.7: RFP power spectra and signal-to-noise trends for 1 h oscillator. **(a)** Top: Mean RFP power spectra (receiver strain) in response to an oscillating input with a period of 2 h (red dashed line). Power spectra were calculated using the Welch method with a Hamming windowing function at steady-state for 395–1536 min (see **Methods**). The gray shaded region denotes a bandwidth of ±10 min around the expected input frequency. Bottom: Mean RFP power spectrum (receiver strain) in response to an input period of 1 h (blue dashed line) for 500–1249 min. The gray shaded region denotes a bandwidth of ±5 min around the expected input frequency. **(b)** Signal-to-noise (SNR) ratios computed using bootstrapped power spectra for GFP or RFP for each distance (**Methods**) in the 1 h forced oscillator experiment. Left and right axes denote SNR for GFP and RFP, respectively. Horizontal lines within boxes denote the median and upper and lower edges represent the upper and lower quartiles, respectively. Upper and lower whiskers represent the 95th and 5th confidence intervals, respectively. Horizontal lines with stars denote statistically significant differences ($P < 0.05$) based on one-tailed bootstrapped hypothesis testing. $*P < 0.05, **P < 0.01$, and $***P < 0.001$ (see **Appendix A**).

Figure 4.7b). In response to a 2 h period, the RFP SNR was inversely related to spatial separation from the senders (**Figure 4.6b**), since it is dominated the distance-dependent profile within the signal bandwidth of the power spectrum. Notably, the RFP SNR increased with distance in the 1 h forced oscillation experiment (**Figure 4.7b**). The overall lower amplitude in the 1 h oscillations produced low power within the signal bandwidth. Hence, the RFP SNR is dominated by the distance-dependent trend in the noise at higher input frequencies.

The noise reduction observed as a function of distance warrants further investigation, particularly as it seems to cohere with previous theoretical work on the role of diffusional dissipation in cell signaling [95,132]. For instance, it is known that diffusion of biomolecules between cells can reduce concentration fluctuations [132, 133], such as those generated during transcriptional bursting. Specifically in the context of quorum sensing, diffusional dissipation is shown to attenuate extrinsic noise [95,132], which often dominates total noise in gene expression [94]. We thus speculate that diffusional dissipation of a signal over a greater distance damps fluctuations in signal synthesis.

Our analysis demonstrates that in the regime of a critical input frequency the fidelity of inter-strain communication is diminished at short distances due to elevated noise. However, diffusible signals can also have limited range over long distances [134], as evidenced by the observed amplitude attenuation over distance. Together, these results suggest that the reliability of information transmission in bacterial signal communication can vary non-monotonically with distance in response to inputs near a critical frequency. Additionally, distance can function as a low-pass filter to allow cells to selectively respond to prolonged environmental fluctuations. Above a critical input frequency where cellular noise dominates, spatial separation can modify a trade-off between the reliability of information transmission and the magnitude of the output response.

4.2 The effect of spatial separation on the behavior of a dual-feedback oscillator

The intracellular networks mediating microbial interactions can comprise of interlinked feedback loops and bidirectional communication. Some GRNs can produce oscillations in the absence of external driving inputs [55]. We sought to understand the effects of spatial separation on the dynamics of a distributed gene circuit oscillator consisting of an *E. coli* activator strain that produces C4-homoserine lactone (C4-HSL), which induces the enzymatic synthesis of 3-OHC14-HSL in an *E. coli* repressor strain (positive inter-strain interaction) [56]. The activator also autoregulates its activity via a positive feedback loop in the circuit controlling C4-HSL production (**Figure 4.8a**). The signal 3-OHC14-HSL, produced by the repressor strain, induces the expression of a quorum-quenching lactonase, AiiA, in the activator and repressor strains, which degrades both signals. 3-OHC14-HSL further executes a second layer of negative feedback by decreasing transcription via a synthetic inverter, mediated by the repressor, LacI (see **Appendix B**). Identical promoters driving the synthetases in the activator and repressor strains also regulate the expression of cyan fluorescent protein (CFP) and yellow fluorescent protein (YFP), respectively, which enables real-time monitoring of circuit activity within MISTiC (**Figure 4.8b**).

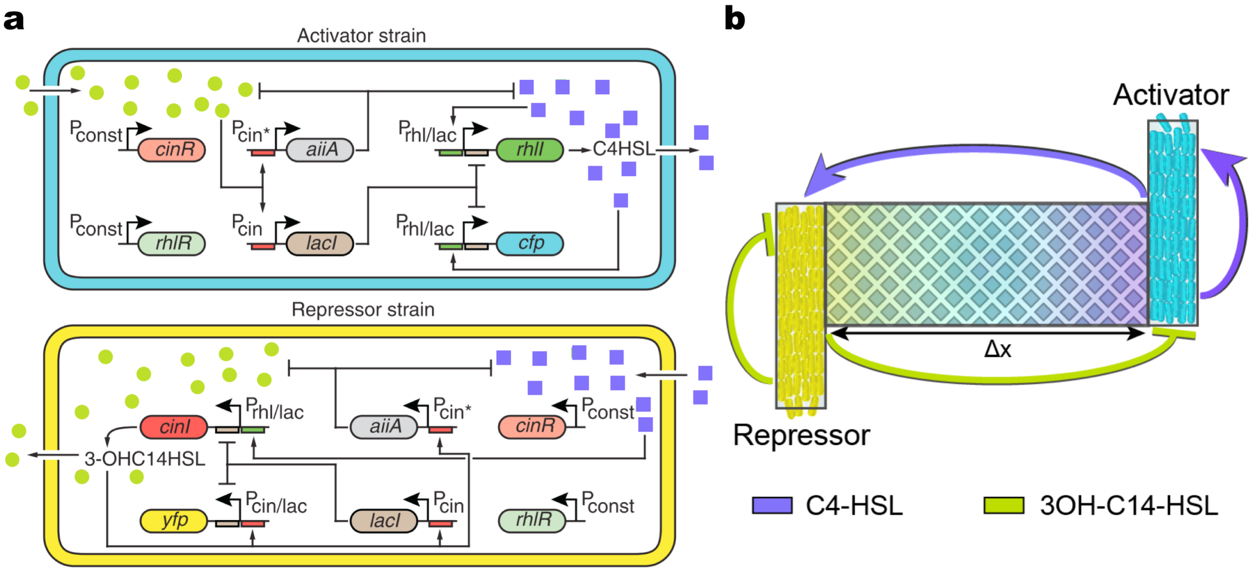

Figure 4.8: Gene regulatory network of a dual-feedback oscillator. **(a)** C4-HSL, produced the activator strain, prompts gene expression in the activator and repressor. 3-OHC14-HSL, produced by the repressor strain, quenches quorum-signals in both strains through AiiA activity and activates a *lac*-mediated inverter. Both strains constitutively express the receptors cinR and rhlR, which bind to 3-OHC14-HSL and C-HSL, respectively. The promoters $P_{cin/lac}$ and $P_{rhl/lac}$ are hybrid promoters regulated both by their respective signals and by LacI. This schematic is adapted from [56] with minor alterations. **(b)** Global topology of activator and repressor strains within the MISTiC microenvironment.

When co-cultured without spatial constraints, the activator and repressor strains synchronize long-term oscillations with a period of approximately 120 min, and display no oscillations when cultured separately [56]. Within the MISTiC microenvironment, spatial separation between activator and repressor strains impacts the oscillatory dynamics of both strains, and consequently their temporal synchronization (**Figure 4.9**) (see Experiment 5, **Appendix A**). The CFP amplitude increased with distance whereas the YFP amplitude displayed the reverse trend (**Figure 4.10a**), signifying that spatial separation modified the relative impacts of positive and negative feedback on each strain. The number of activator peaks moderately increased and number of repressor peaks substantially decreased with distance (**Figure 4.10b**), indicating that the oscillatory behavior of the repressor is highly sensitive to variations in the interaction range. Our data shows that the activator amplitudes vary non-monotonically with distance; the amplitudes were diminished by stronger repression at short distances, increased at intermediate distances, and disappeared at long distances as the activator expression approached a constitutive ON state (**Figure 4.9**). Conversely, the

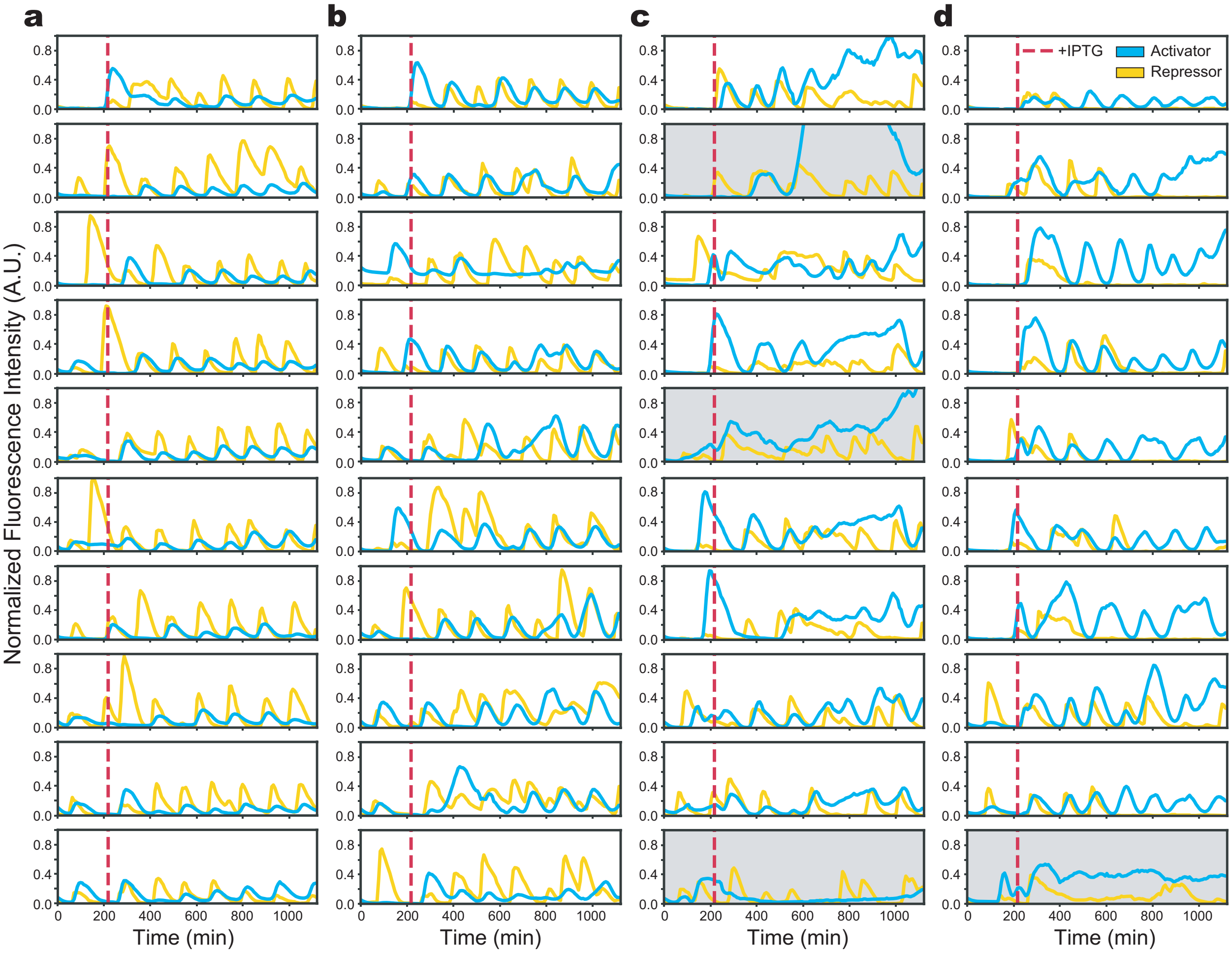

Figure 4.9: Fluorescence intensity over time of spatially separated dual-feedback oscillators. **(a)** Normalized CFP (activator) and YFP (repressor) fluorescence intensity as a function of time for a separation distance of 25 μm. The red dashed line indicates the time when IPTG was introduced. For each fluorescence reporter, the fluorescence intensity was normalized between the global minimum and maximum excluding the outliers (gray shaded boxes). **(b)** Normalized CFP (activator) and YFP (repressor) fluorescence intensity as a function of time for a separation distance of 50 μm. **(c)** Normalized CFP (activator) and YFP (repressor) fluorescence intensity as a function of time for a separation distance of 100 μm. **(d)** Normalized CFP (activator) and YFP (repressor) fluorescence intensity as a function of time for a separation distance of 250 μm.

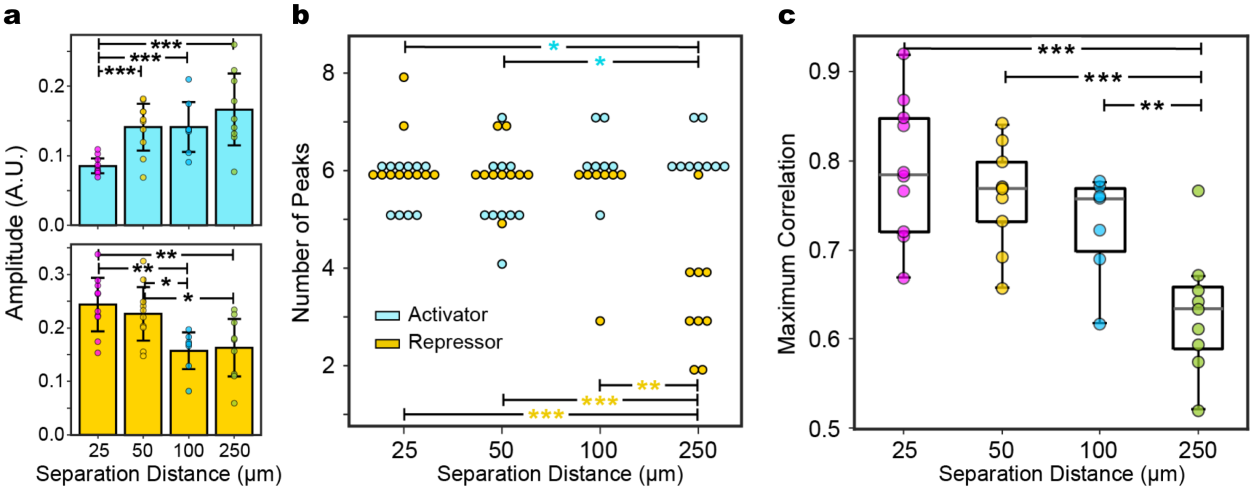

Figure 4.10: Amplitude, peak number, and maximum correlation of dual-feedback oscillators across distance. **(a)** Amplitude of peaks in the mean-subtracted CFP (top) and YFP (bottom) fluorescence intensities across distances. Error bars represent one standard deviation from the mean. Horizontal lines with stars denote a statistically significant difference ($P < 0.05$) based on a two-sided t-test. **(b)** The number of peaks as a function of distance for activator and repressor strains, detected using a peak-finding algorithm. Horizontal lines denote a statistically significant difference ($P < 0.05$) based on a two-sided t-test. **(c)** Maximum cross-correlation between paired CFP and YFP time-series measurements for each distance. The horizontal lines within boxes denote the median and upper and lower edges represent the upper and lower quartiles, respectively. Upper and lower whiskers represent the 95th and 5th confidence intervals, respectively. Horizontal lines with stars denote a statistically significant difference ($P < 0.05$) based on a two-sided t-test. $*P < 0.05, **P < 0.01$, and $***P < 0.001$ (see **Appendix A**).

repressor amplitudes decreased with distance and displayed an abrupt loss of oscillatory behavior at a spatial separation of 100 - 250 μm from the activator strain.

Synchronization of oscillatory function may exhibit as phase-shifted behavior, observed in time-keeping GRNs such as the repressilator [19]. To account for this possibility, we quantified the synchronization between activators and repressors by computing the maximum cross-correlation between their gene expression dynamics (**Figure 4.10c**). Our results show that spatial separation diminished the maximum cross-correlation between activators and repressors, signifying that the loss of coordinated behavior is not solely a consequence of phase-shifts. While the time-lag required for maximum correlation increases with distance (**Figure 4.11a**), the distribution of data points indicates that this trend may be influenced by the diminishing number of repressor peaks at longer distances, obfuscating potential phase-shifts between CFP and YFP. We thus

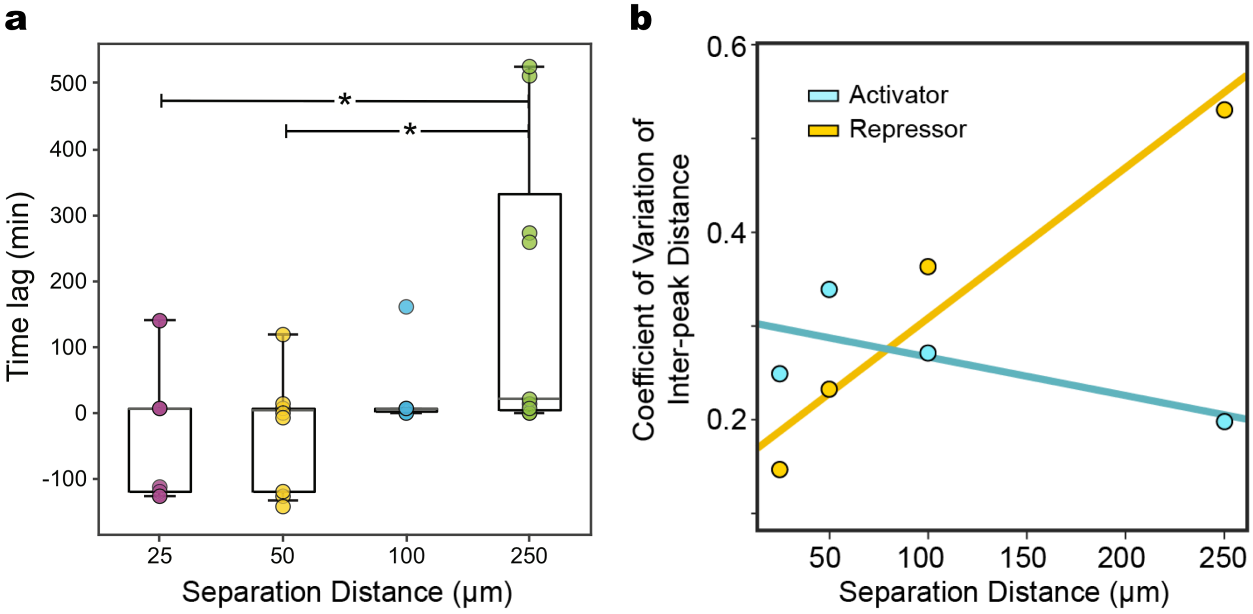

Figure 4.11: Amplitude, peak number, and maximum correlation of dual-feedback oscillators across distance. (a) Amplitude of peaks in the mean-subtracted CFP (top) and YFP (bottom) fluorescence intensities across distances. Error bars represent one standard deviation from the mean. Horizontal lines with stars denote a statistically significant difference ($P < 0.05$) based on a two-sided t-test. **(b)** The number of peaks as a function of distance for activator and repressor strains, detected using a peak-finding algorithm (Python). Horizontal lines denote a statistically significant difference ($P < 0.05$) based on a two-sided t-test. **(c)** Maximum cross-correlation between paired CFP and YFP time-series measurements for each distance. The horizontal lines within boxes denote the median and upper and lower edges represent the upper and lower quartiles, respectively. Upper and lower whiskers represent the 95th and 5th confidence intervals, respectively. Horizontal lines with stars denote a statistically significant difference ($P < 0.05$) based on a two-sided t-test. $*P < 0.05, ** P < 0.01$, and $***P < 0.001$ (see **Appendix A**).

quantified the variability in oscillations as an indicator of phase drift across distance [8] by mapping the distribution of inter-peak times for each strain (**Figure 4.12**). The coefficient of variation of the inter-peak distance distribution increased by more than three-fold for the repressor strain between the 25 μm and 250 μm separation, but did not change significantly for the activator strain (**Figure 4.11b**).

Our results demonstrate divergent effects of spatial separation on the activity of the activator and repressor strains, indicating that distance skewed the influence of inter-strain feedback relative to autoregulation. The increase in peak amplitudes along with a negative trend in oscillation variability suggests that distance increased the influence of positive feedback on activator behavior, whereas increased variability in oscillation

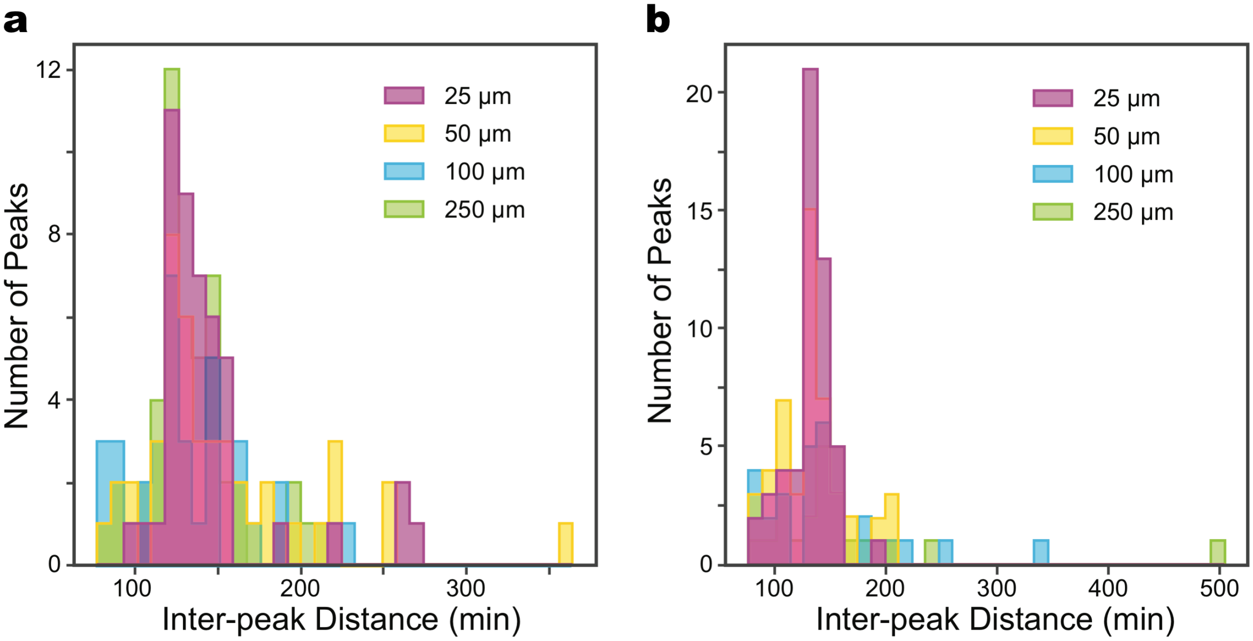

Figure 4.12: Distributions of inter-peak distances for the dual-feedback oscillator consortium. **(a)** Histogram of inter-peak distances for CFP (activator). A peak-finding algorithm (Python) was used to determine the peaks in the normalized CFP fluorescence intensity as a function of time. CFP was normalized by subtracting a moving mean. The inter-peak distance was computed as the difference in the times corresponding to each peak for all replicates of a given interaction channel length. **(c)** Histogram of inter-peak distances for YFP (repressor).

and the progressive loss in the number of peaks implicates the growing dominance of negative feedback with distance. Overall, this study underscores the importance of spatial organization on the behavior of distributed gene regulatory circuits, and microbial interactions more generally.

4.3 Methods

Device fabrication. Microfluidic devices for Experiments 3-5 were fabricated according to the methods elaborated in **Chapter 2**. Prior to each experiment, the devices were flushed with 0.5% Tween 20 (Sigma-Aldrich) to prevent cells from adhering to the device.

Forced oscillator experimental setup. Sender and receiver strains were cultured and prepared for experiments using the methods described in **Chapter 3**. The setup for the MISTiC device was identical to that of the sender-receiver experiments in **Chapter 3**, with the exception of the syringe pump program used to alternate arabinose induction. The forced oscillation experiments used 10 mL syringes to extend the duration of the experiment. Oscillations were applied once the growth chambers were filled with cells (see **Appendix A**). Flow rates of the 0.1% arabinose (inlet I_{22}) and 0% arabinose (inlet I_{21}) were alternated out of phase between 200 and 0 μL/h for a period of time. One of the receiver inlets (I_{11}) flowed continuously at a rate of 200 μL/h and the other inlet (I_{12}) was set to 0 μL/h for the duration of the experiment.

Data analysis for forced oscillator experiments. For Experiment 3, DeepCell [118] was used for image segmentation. Experiment 4 was processed with custom Python code for image alignment and segmentation. Both of these methods are elaborated in **Chapter 3** and produce identical results. The methods for computing the average fluorescence intensity for each growth chamber and excluding outliers were identical to those described in **Chapter 3**. For both forced oscillator experiments, a peak finding algorithm (Python) was applied to the time-series gene expression data at steady-state with a minimum inter-peak threshold of 21 min. The amplitude was computed by subtracting the minimum and maximum of each oscillation and dividing this value by two. To calculate the SNR, a moving mean computed over 20 time points was subtracted from the data. The power spectra for each replicate was calculated using Welch's method (Python) with a Hamming window applied across the length of the time-series. The power spectra were filtered to exclude frequencies lower than the signal bandwidth. The signal was defined as the total power of the signal bandwidth. The noise was computed as the total power of frequencies larger than the signal bandwidth. The power spectra for all the replicates for a given interaction channel length were randomly sampled with replacement 10,000 times. For each iteration, the SNR ratio was computed by dividing the signal by the noise. Bootstrap hypothesis testing, as described in **Chapter 3**, was used to compute P-values.

Dual-feedback oscillator experimental setup. To construct the strains, the *E. coli* strain CY027 was transformed separately with plasmids pC220 and pC239 or pC236 and pC239 to construct the activator and repressor [56], respectively, using a standard chemical transformation protocol (see **Appendix B**). Overnight cultures were inoculated into LB media (Lennox) containing 50 μg/mL kanamycin and 100 μg/mL spectinomycin and incubated overnight at 37 °C with shaking. After approximately 16 h, 1 μL of the overnight cultures was diluted into 3 mL LB media and incubated at 37 °C with shaking to early stationary phase (OD600 0.7–1.1). Cells were loaded into the device following the procedure specified in **Chapter 1**. Following cell loading, the microfluidic chip was placed in the custom-designed temperature incubation chamber at 37 °C. All four inlets were connected to 10 mL syringes containing LB media with kanamycin (50 μg/mL), spectinomycin (100 μg/mL), and 0.1% Tween 20. Syringes connected to inlets I_{22} and I_{11} also contained 1 mM isopropyl β-D-1-thiogalactopyranoside (IPTG) (Sigma). The cells were initially grown in the device at 37 °C with inlets I_{12} and I_{21} flowing at 200 μL/h, and inlets I_{22} and I_{11} flowing at 10 μL/h to prevent cell growth and clogging. Phase-contrast and fluorescence images were collected every 7 min at 21 different positions. Once the growth chambers were filled with cells (see **Appendix A**), the inlets (I_{12} and I_{21}) containing the pre-culture media were set to 0 μL/h and the inlets (I_{11} and I_{22}) containing the test media were set to 200 μL/h.

Data analysis for dual-feedback oscillator experiment. The custom Python code for image alignment and segmentation, the fluorescence image analysis, and outlier exclusion method for Experiment 5 are elaborated in **Chapter 3**. The fluorescence intensity of each fluorescent reporter was normalized by subtracting the global minimum of the reporter across all replicates, dividing by the global maximum of fluorescence across all replicates, and applying a moving mean of 20 time points to the data. A peak finding algorithm (Python) was applied to detect peaks with a minimum inter-peak distance of 70 min and a minimum peak height of 0.015 by analyzing the data after the media switch. The number of peaks detected, the amplitude of expression at each peak, and the distance between subsequent peaks were computed for each replicate.

Chapter 5

Engineering Relay Signaling in Microbial Consortia

In contrast to signal transport via passive diffusion, relay signaling refers to a mode of active signal propagation wherein cells generate a signaling molecule upon detecting its presence in the environment [135]. In our sender-receiver experiments, the concentration gradients of AHL from the sender population across the interaction channel resulted in a graded, distant-dependent profile of RFP expression. A relayed signal is unlikely to maintain concentration gradients over time as signal amplification rapidly increases local concentrations and advances a diffusible wavefront in space, facilitating long-range communication and coordination [135]. The spatial range is a critical parameter that governs range expansion in microbial communities [69]. Whereas steady-state gene expression reflected the spatial orientation of the receiver strain relative to the senders, we expect that positional information will be encoded in the dynamics of gene expression in the repeaters instead of the steady-states. Relay communication is more robust to variations in cell density or population size than direct signaling; if the signal concentration in any local region exceeds a critical threshold, the amplify-and-forward relay mechanism ensures an all-or-nothing response across the population [136]. In this chapter, I characterize the relay activity of an amplify-and-forward sender-repeater consortium in the FAIRY platform, and compare the long-range spatial profiles of gene expression to that of the sender-receiver system which lacks the capacity for relay.

The spatial range of diffusible signals is also a key variable governing spatial patterns in gene expression [43, 59]. The differential response to relative concentrations of signals, established by their overlapping concentration gradients, is the basis of morphogenesis [41, 137]. Turing patterns can be produced by imposing differences in the spatial range of activating and inhibiting signals [40]. A sufficient disparity in the diffusion coefficients of these signaling molecule presents a practical limitation for engineering pattern formation, which is often constrained by niche parameter regimes [6]. However, in a relay mechanism, the rate of signal propagation can be theoretically tuned by intervening in the positive feedback loop governing synthesis of the signal. In this chapter, the rate of signal amplification in the receivers is modulated by introducing mutations to the pLuxI promoter in the repeater strain. We aimed to generate traveling pulses by introducing an inhibitory mechanism with a higher activation threshold in the repeaters. We explore how the circuit parameters underlying the relay mechanism influence excitable dynamics on the population level.

5.1 Design and characterization of an amplify-and-forward repeater.

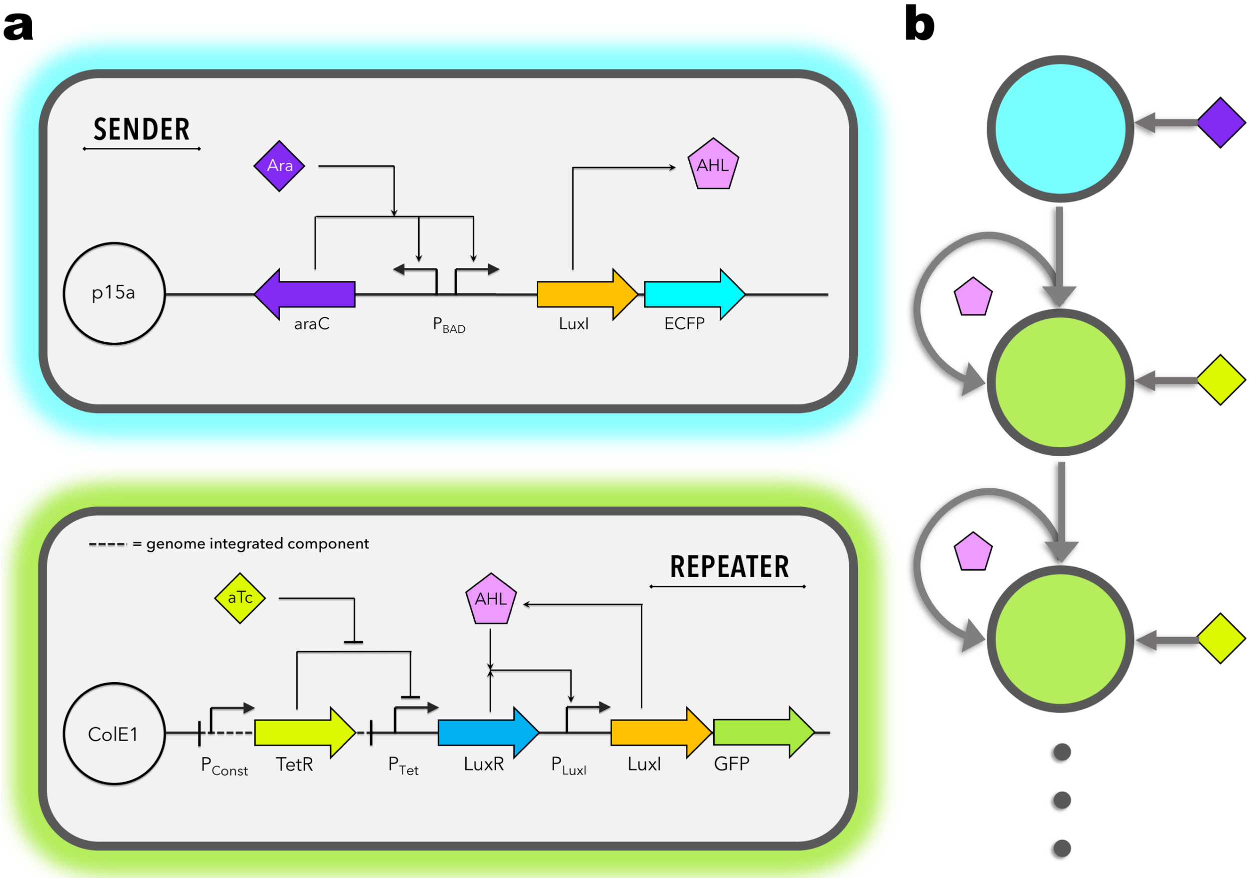

Figure 5.1: Gene regulatory network of a synthetic sender-repeater consortium. (a) In response to arabinose, the sender strain expresses LuxI, which synthesizes AHL, and CFP which provides a readout of signal . The repeater strain expresses LuxR in response to exogenous aTc. Incoming AHL binds to LuxR to drive a positive feedback loop for further AHL synthesis. **(b)** Schematic of senders and repeaters in a spatially separated relay configuration. The receivers amplify the signal and diffusion propagates it forward.

To investigate diffusion-mediated relay signaling, we engineered an amplify-and-forward GRN in an *E. coli* community consisting of a sender strain that produces the quorum sensing signal 3-oxo-C6-HSL (AHL) and a repeater strain that senses the signal and responds by auto-activating AHL synthesis (**Figure 5.1**).

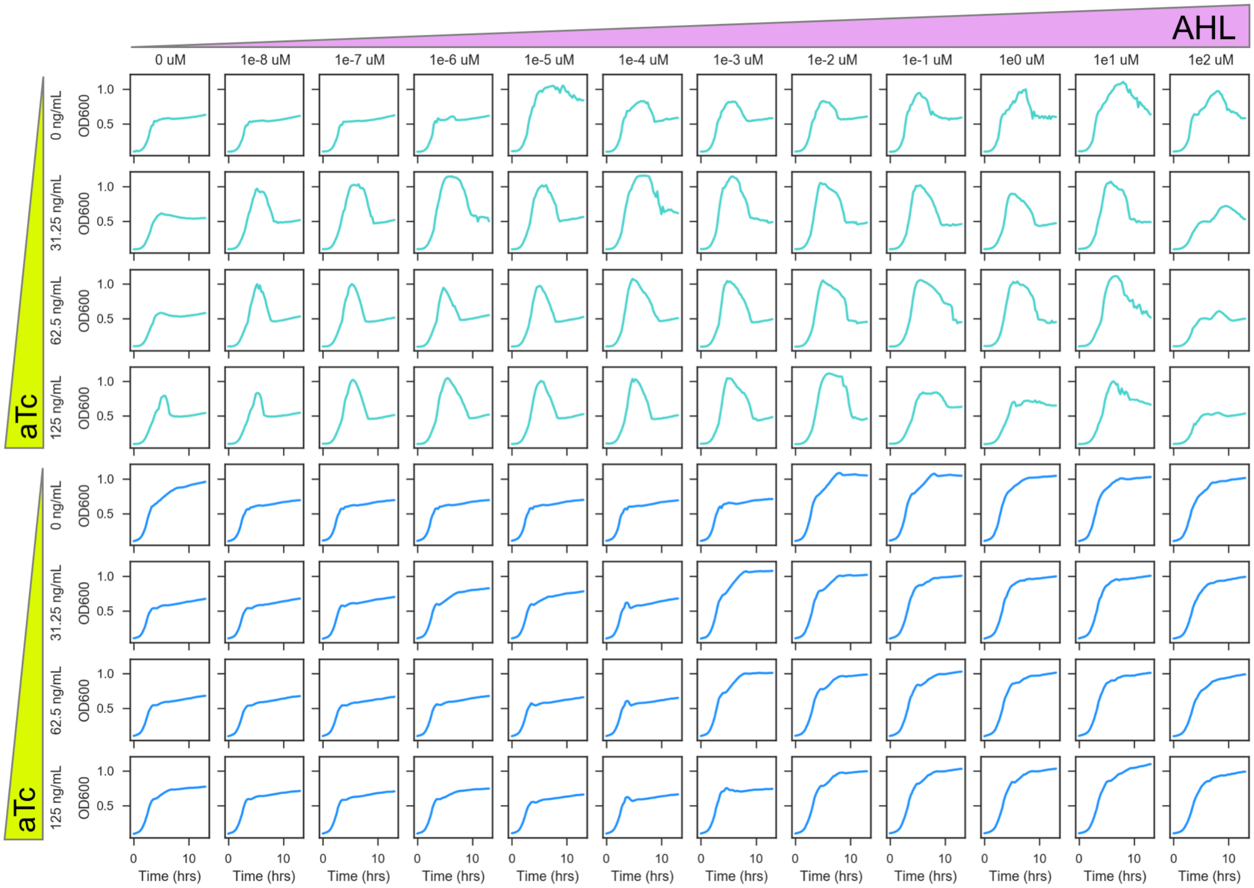

Figure 5.2: Receiver and repeater growth curves over time across a range of aTc and AHL concentrations. The first four rows (turquoise) depict repeater growth dynamics, and the bottom four rows depict receiver growth dynamics. AHL is titrated on the x-axis from 0 to 100 μM with a 10-fold serial dilution per column. aTc is titrated on the y-axis for each strain from 0 to 125 ng/mL with a 2-fold serial dilution per row. Growth defects are observed across all conditions with the exception of aTc = 0 ng/mL, AHL $\leq 10^{-7}$ μM and AHL = 0 μM, aTc $\leq$ 62.5 ng/mL. At 100 μM AHL, an overall lower OD600 is noted, likely as a result of AHL toxicity.

The sender strain is identical to that used in the sender-receiver experiments (see **Chapter 3**), with the exception of its fluorescent reporter, which was swapped to a cyan fluorescent protein (CFP). The repeater strain contains an anhydrotetracycline (aTc)-inducible AHL receptor, LuxR, which complexes with AHL to activate the synthesis of LuxI, an AHL synthetase, transcriptionally fused to a green fluorescent protein, GFP (see **Appendix B**).

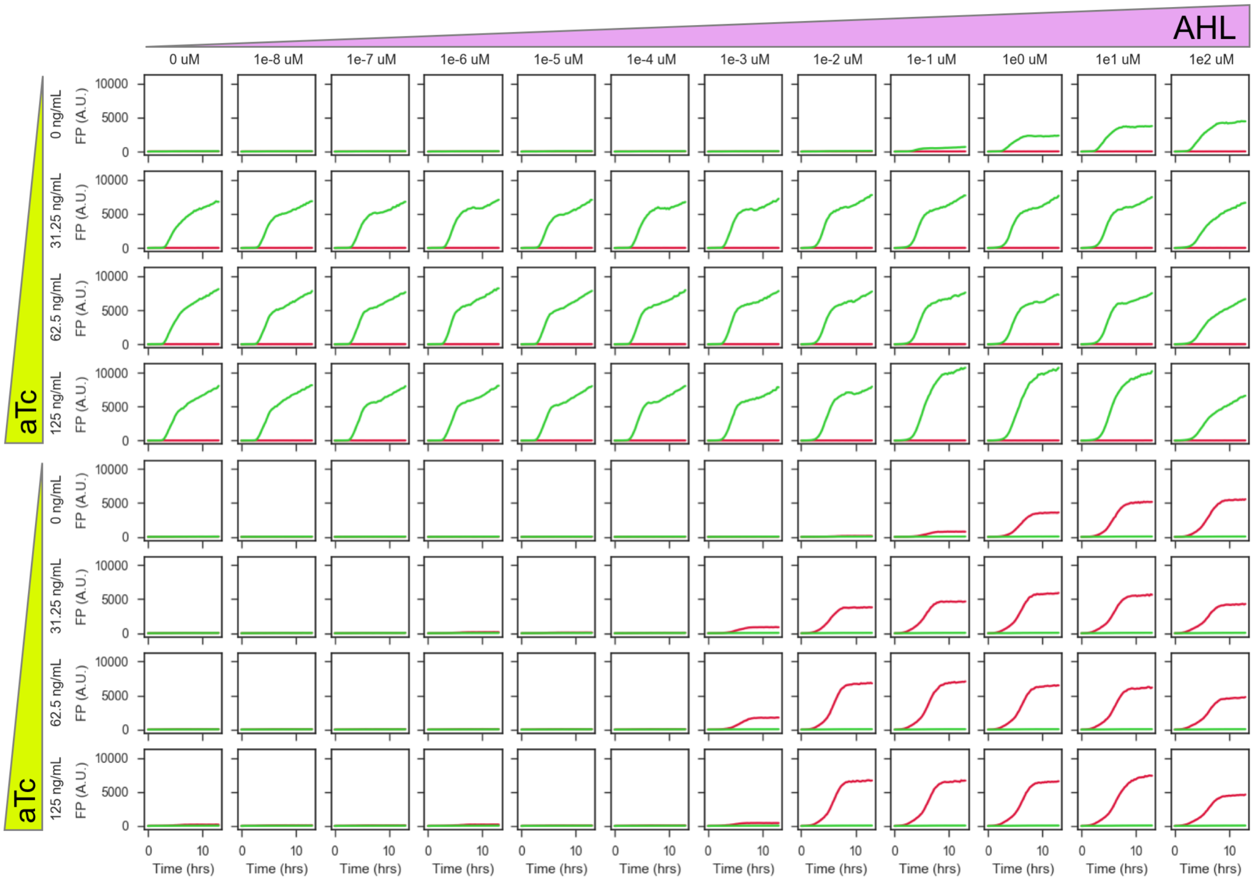

Figure 5.3: Receiver and repeater gene expression dynamics across a range of aTc and AHL concentrations. The first four rows depict repeater microwells and the bottom four rows show repeater microwells. RFP and GFP expression was measured for both strains. AHL is titrated on the x-axis from 0 to 100 μM with a 10-fold serial dilution per column. aTc is titrated on the y-axis for each strain from 0 to 125 ng/mL with a 2-fold serial dilution per row.

To assess the impact of positive feedback on the dynamics of the repeater strain, its growth and gene expression responses were compared to that of the receiver strain. Both strains were cultured in microwell plates with concentrations of aTc ranging from 0 to 125 ng/mL on one axis and AHL titrated from 0 to 100 μM on the other. In contrast to the receiver populations, growth curves for the repeater strain display a death phase when both inducers were present in any amount, suggesting that the positive feedback loop presents a significant metabolic burden for the cells (**Figure 5.2**). Auto-activation was observed in the repeater's gene regulatory circuit even in the absence of either inducer, indicating leakiness in expression of both LuxR and LuxI (**Figure 5.3**). Dose-response curves depicting steady-state expression as a function of

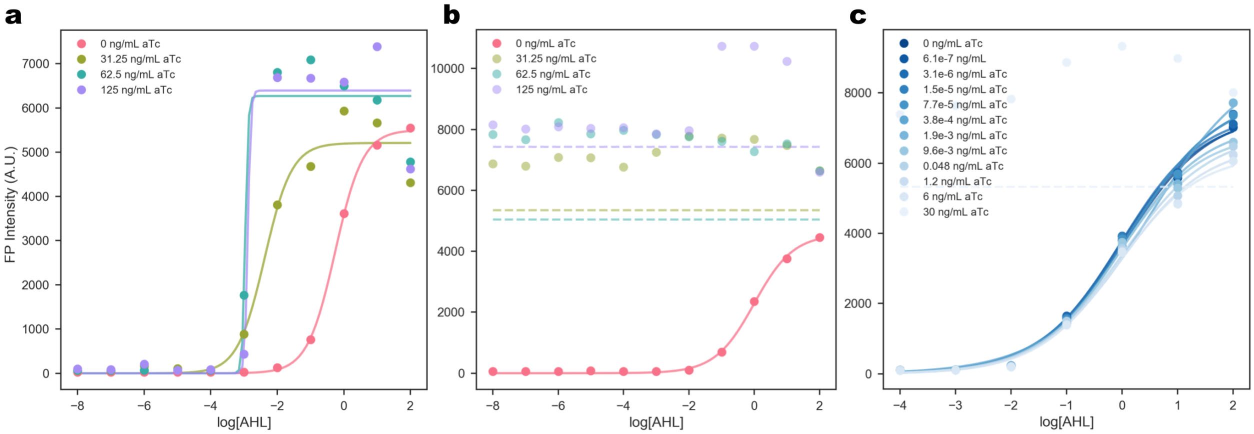

Figure 5.4: Dose-response curves for receivers and repeaters. **(a)** AHL dose-responses of the receivers at various aTc concentrations. Circles represent measured RFP expression at steady-state. Lines represent Hill equations fit to the data for each aTc condition (see **Table 5.1** for parameters and the coefficient of determination (R^2) of the fit). **(b)** AHL dose-response curves of the repeaters at various aTc concentrations. Circles represent GFP expression measured at steady-state. Increased transparency was used to plot data points for conditions in which a sigmoidal dose response was not observed. Lines represent Hill equations fit to the data for each aTc condition (see **Table 5.1** for parameters and R^2 score). Dotted lines represent model fits for which the R^2 score was less than 0.5. **(c)** AHL dose-response curves for repeaters at lower concentrations of aTc. Circles represent GFP expression measured at steady-state. Increased transparency indicates conditions in which a sigmoidal dose response was not observed. Lines represent Hill equations fit to the data for each aTc condition. Dotted lines represent model fits for which the R^2 score was less than 0.5.

AHL demonstrate that, in both strains, leaky LuxR expression (denoted by the absence of aTc) generates a measurable response only at high concentrations of AHL ($\geq 0.1\ \mu$M) (**Figure 5.4a,b**). Whereas the presence of aTc sensitizes the dose-response to AHL by 100-fold in the receivers, it all but eliminates the threshold in the repeaters, triggering auto-activation to saturation even in the absence of AHL. We assayed repeater dose-responses at lower aTc concentrations and confirmed that aTc acts as a switch, prompting an all-or-nothing response at concentrations of AHL ($\leq 10^{-2}\mu$M) (**Figure 5.4b,c**). These results indicate sufficient leakiness at the LuxI-GFP regulatory site that a critical concentration of LuxR (corresponding to aTc concentrations between 6 and 30 ng/mL) enables uninhibited signal amplification. At aTc concentrations ≤ 6 ng/mL, LuxR presents a bottleneck to signal amplification, as illustrated by the linear dose-response to high concentrations of AHL ($\geq 0.1\ \mu$M) (**Figure 5.4c**).

aTc = 0 ng/mL					**aTc = 31.25 ng/mL**				
Strain	α	n_{FP}	K_{FP}	R^2	**Strain**	α	n_{FP}	K_{FP}	R^2
Rec	5.50e+03	1.04e+00	5.51e−01	0.99	Rec	5.21e+03	1.07e+00	4.18e−03	0.97
WT	4.56e+03	7.25e−01	9.91e−01	0.99	WT	5.35e+03	1.05e+00	5.62e−16	< 0
V_1	3.83e+03	5.16e−01	1.56e+00	0.99	V_1	3.56e+03	3.78e−01	7.39e−26	< 0
V_2	4.18e+03	3.57e−01	1.24e+03	0.99	V_2	2.61e+03	7.03e−01	1.57e−01	0.99
V_3	1.50e+02	2.50e−01	1.00e+04	0.53	V_3	8.00e+03	7.00e−01	5.00e+00	0.94
V_4	2.94e+03	4.09e−01	5.77e+00	0.99	V_4	6.06e+03	9.84e−01	1.44e−08	0.60

aTc = 62.5 ng/mL					**aTc = 125 ng/mL**				
Strain	α	n_{FP}	K_{FP}	R^2	**Strain**	α	n_{FP}	K_{FP}	R^2
Rec	6.27e+03	1.01e+01	1.10e−03	0.97	Rec	6.39e+03	9.89e+00	1.30e−03	0.96
WT	5.05e+03	1.10e+00	3.89e−16	< 0	WT	7.44e+03	9.24e−01	3.68e−17	< 0
V_1	3.23e+03	5.51e−01	1.28e−23	< 0	V_1	2.51e+03	2.97e−01	3.63e−30	< 0
V_2	6.82e+03	1.02e+00	3.25e−02	0.99	V_2	7.20e+03	5.67e−01	1.38e−02	0.99
V_3	8.70e+03	7.50e−01	5.00e+00	0.94	V_3	1.00e+04	5.00e−01	7.00e+00	0.94
V_4	6.56e+03	5.84e−01	7.70e−08	0.63	V_4	6.51e+03	4.74e−01	1.21e−07	0.41

Table 5.1: Parameter values and scores for Hill equation fits to AHL dose-responses for receivers and repeaters. Note that model fitting functions yielded $R^2 < 0$ for several sets of experimental data that did not conform to a sigmoidal response (see **Figure 5.4** and **Figure 5.9**). A negative R^2 score indicates that a horizontal line is better than the model fit to the data. While initial parameter guesses for this variant were able to achieve $R^2 > 0.90$, the fitting function was unable to finish the optimization process for V_3 as its dose response curve does not saturate for the AHL range tested.

We tested communication between sender and receiver strains within the FAIRY platform in order to establish a reference point for signaling dynamics across relay nodes in the absence of an amplify-and-forward motif. 0.1% arabinose and 62.5 ng/mL aTc were added to the agar media to induce LuxI-CFP and LuxR expression in the sender and repeater strains, respectively. The CFP-expressing sender strain was inoculated in the first well of the series, denoting the sender node, N_0. Receiver strains were cultured in all subsequent wells, N_{1-3}, of the 3-node device (**Figure 5.6,**inset). Only the sender node reached steady-state gene expression over the course of the 16 h experiment (**Figure 5.5a**). The average RFP expression for each node at the final time-point decreased as a function of distance from the sender node, indicating the presence of an AHL concentration gradient across the interaction channel of the device (**Figure 5.6**). The average RFP expression at each node crosses a threshold intensity only after the node before it, qualitatively showing time delays. These results demonstrate that the FAIRY device can resolve population-level gene expression dynamics and time delays in long-range diffusion-mediated signaling.

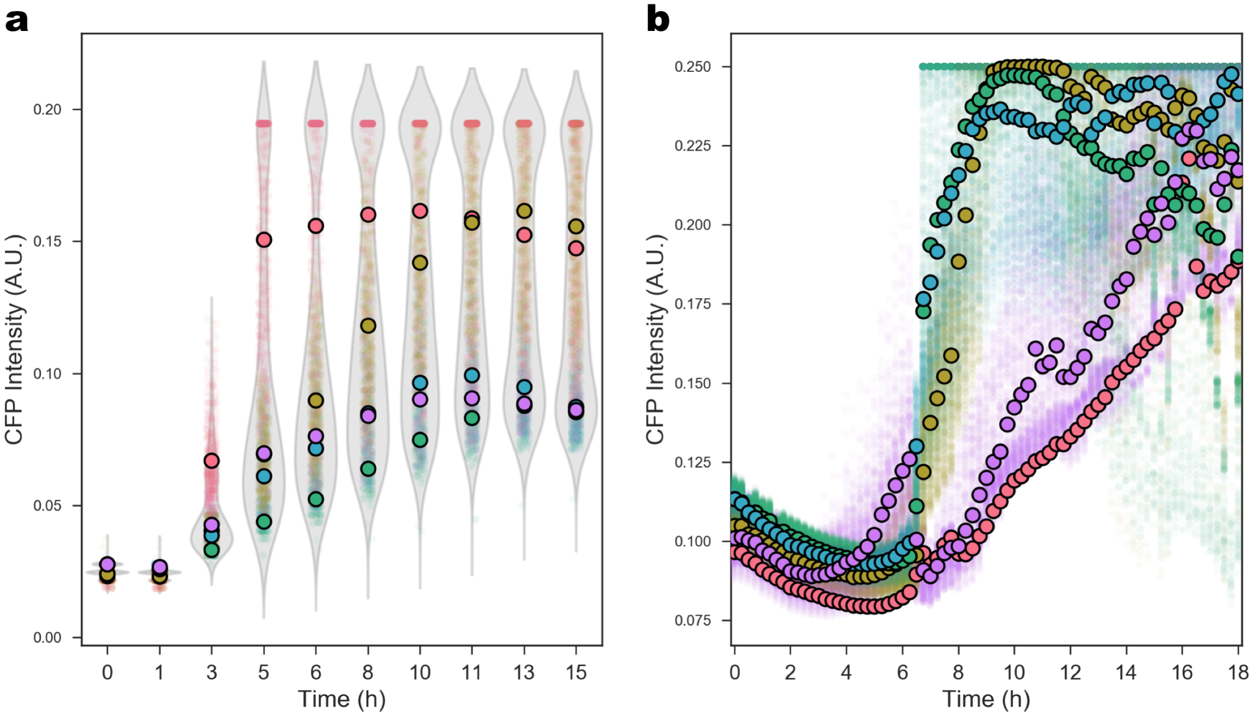

Figure 5.5: CFP gene expression at the sender node in FAIRY experiments. **(a)** CFP expression at N_0 in the sender-receiver experiment. Five technical replicates were collected for each node throughout the experiment. Each replicate is assigned a unique color, with the average fluorescence across the entire replicate shown by large bordered circles, and the intensity across distinct 330 μm^2 regions within each replicate shown by small transparent circles. The distributions of these circles are quantified using a kernel density estimation shown by the gray violin plots for each time-point as an indicator of the spatial variation in gene expression within each node. **(b)** CFP expression at N_0 in the sender-repeater experiment. Five technical replicates were collected for each node throughout the experiment. Each replicate is assigned a unique color, with the average fluorescence across the entire replicate shown by large bordered circles, and the intensity across distinct 330 μm^2 regions within each replicate shown by small transparent circles.

Since microbial community behaviors can vary significantly between liquid cultures and structured environments [66, 73, 97, 107] we tested the influence of the FAIRY environment on the population-level gene expression dynamics of the repeater strain. Media conditions remained unchanged between the receiver and repeater experiments in order to isolate the influence of circuit topology on relay signaling dynamics. The

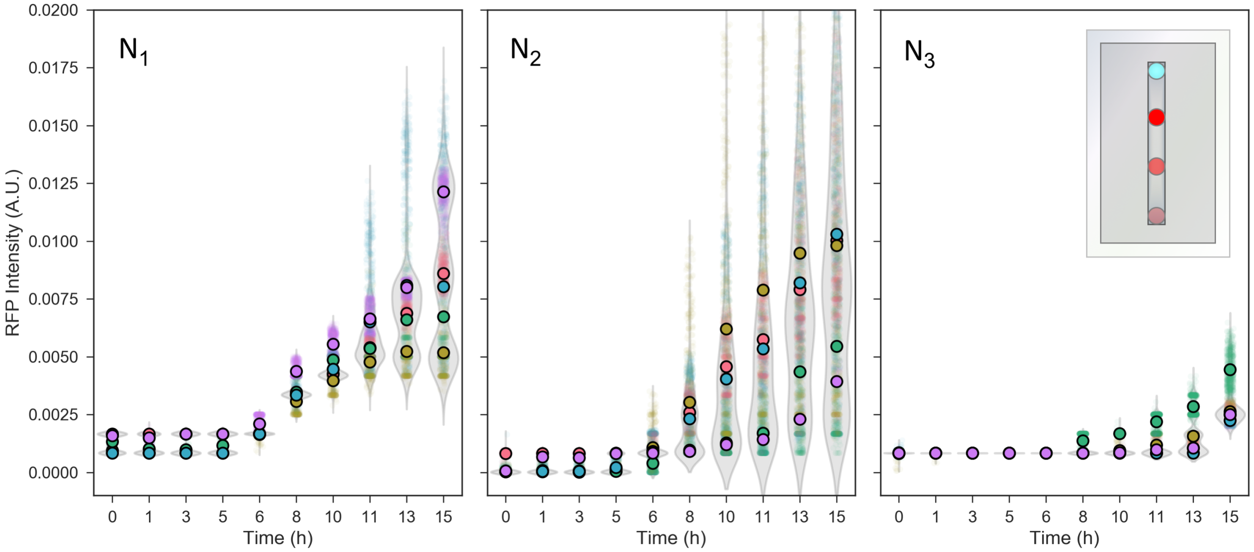

Figure 5.6: RFP gene expression across nodes N_{1-3} for sender-receiver communication in the FAIRY device. Five technical replicates were collected for each node throughout the experiment. Each replicate is assigned a unique color, with the average fluorescence across the entire replicate at each time point shown by large bordered circles, and the intensity across distinct 330 μm^2 regions within each replicate shown by small transparent circles. The distributions of these circles are quantified using a kernel density estimation shown by the gray violin plots for each time-point as an indicator of the spatial variation in gene expression within each node. Abrupt variations in fluorescence, as seen in the purple replicate, were due to distortions by liquid droplets at the agar-glass interface. The inset shows a schematic of the relay setup of the device.

sender strain was cultured in the first node, N_0, with repeater strains occupying all subsequent nodes, N_{1-6} in the 7-node series (**Figure 5.5b**).[1] All nodes reached steady-state gene expression over the course of the 18 h experiment (**Figure 5.7**). No delays in CFP expression were observed as a function of distance even though the sender-receiver experiment indicates detectable delays due to AHL diffusion across nodes. Juxtaposed with the significant delays observed in the sender-receiver experiment, our results suggest that signal propagation across nodes is not a dominant effect in the gene expression dynamics observed in the sender-repeater experiment. Eliminating auto-activation in the repeaters due to leaky gene expression is therefore necessary in order to compel relay communication across nodes.

---

[1] While this experiment was performed in both the 3-node and 7-node FAIRY device, only the data from the latter experiment is reported here to avoid redundancy. In this experiment, the final node was removed from consideration due to a loss of focus during overnight microscopy imaging.

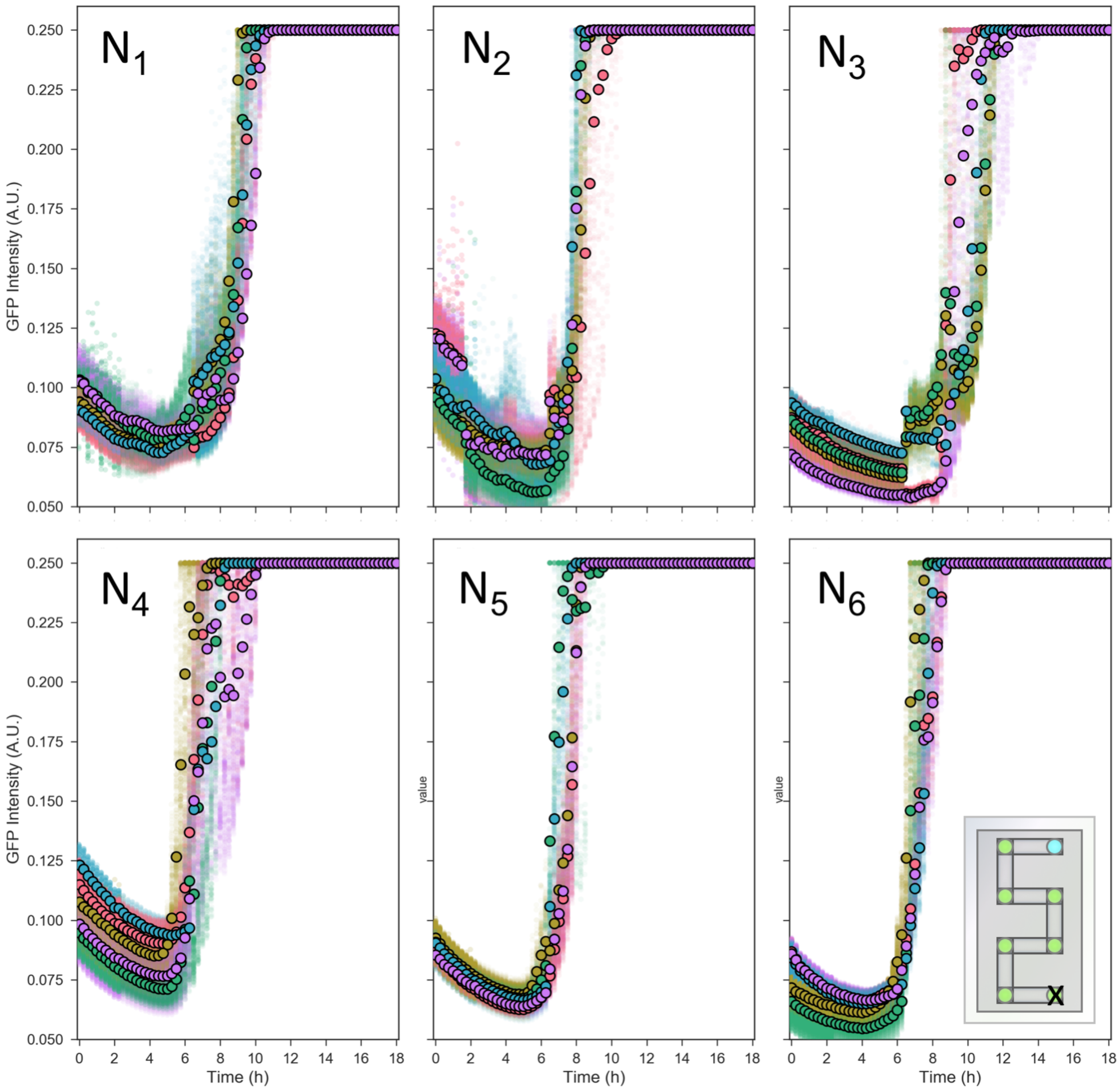

Figure 5.7: GFP gene expression across nodes N_{1-6} for sender-repeater communication in the FAIRY device. Five technical replicates were collected for each node throughout the experiment. Each replicate is assigned a unique color, with the average fluorescence across the entire replicate at each timepoint shown by large bordered circles, and the intensity across distinct 330 μm^2 regions within each replicate shown by small transparent circles. The rapid saturation of the curves indicates that the exposure time used for GFP in this experiment may have obfuscated the full dynamic range of the response. The inset shows a schematic of the relay setup of the 7-node device. The relay node furthest from the sender was removed from consideration due to loss of focus during microscopy imaging.

5.2 Promoter Variants

Our analysis of repeater strain dose-response curves demonstrated that LuxR leakiness is operative only at high AHL concentrations, whereas leakiness in LuxI expression triggers auto-activation in the absence of signal and imposes a fitness cost to the cells. Rather than attempting to decrease LuxI gene expression below an unknown threshold using strategies such as varying the plasmid copy number, adding protein degradation tags, or encoding lactonases to degrade AHL (the latter two may ultimately increase the metabolic burden due to post-translational intervention), we sought to intervene in LuxI regulation by introducing mutations to its promoter, pLuxI.

Based on previous studies that characterized the activity of pLuxI promoter variants [138, 139] using both mutational analysis [136, 140, 141] and rational design [115], we chose four candidates with varying regulatory features (**Figure 5.8**). The first pLuxI mutant, V_1, has a point mutation at the -36 site that lowers leakiness while retaining gene expression [115, 140]. The second variant, V_2, adds three mutations to V_1 at the -11 to -9 sites to further lower leakiness but with significant attenuation of maximum gene expression. We reasoned that the signal amplification built in to the circuit would compensate for this loss in gene expression. The third variant, V_3, has two point mutations to the *lux* box, which defines a region of the promoter that directly interacts with the activated LuxR-AHL complex [140]. The mutations in this region are thought to alter the threshold of the dose-response while maintaining expression at wild-type (WT) pLuxI levels. A final variant, V_4, denoting a point mutation at the -11 site, has been used to reduce leakiness in gene expression [139].

We constructed repeater variants in which the WT pLuxI promoter was replaced with each of the four mutant promoters and transformed them into *E. coli* populations of the same strain background as that of the WT pLux repeater (see **Appendix B**). Dose-response curves for all mutant pLuxI repeaters across varying aTc and AHL concentrations are shown in **Figure 5.9**. The expected reduction in the leakiness of the V_1 repeater was not observed as the effect was likely eclipsed by amplification within the ciruit. The V_1 strain also displayed a prominent death phase across most conditions, reflecting the cost of maintaining gene expression levels close to the WT promoter. The additional mutations conferred by V_2 eliminated auto-activation at low AHL concentrations and altered the threshold of activation as a function of aTc concentrations. A moderate increase with aTc in the fitted Hill coefficient, n_{FP} for the V_2 dose-response indicates that the rate of signal amplification can be tuned in this strain (**Table 5.1**). Notably, the lowest threshold observed in the dose-response for V_2 was similar to that of the receiver strain (approximately 10^{-4} AHL). In contrast, V_3 increased the threshold of activation by 100-fold uniformly across all aTc concentrations, and completely suppressed auto-activation below this new AHL threshold. V_3 also eliminated all detectable gene expression in the absence of aTc, making it unique in its ability to switch the system to the ON state only once both inducers

Strain	pLuxI sequence
WT	ACCTGTAGGATCGTACAGGTTTACGCAAGAAAATGGTTTGTTACAGTCGAATAAA
V_1	ACCTGTAGGATCGTACAG**T**TTTACGCAAGAAAATGGTTTGTTATAGTCGAATAAA
V_2	ACCTGTAGGATCGTACAG**T**TTTACGCAAGAAAATGGTTTGTTA**CTT**TCGAATAAA
V_3	ACC**G**GTAGGAT**T**GTACAGGTTTACGCAAGAAAATGGTTTGTTATAGTCGAATAAA
V_4	ACCTGTAGGATCGTACAGGTTTACGCAAGAAAATGGTTTGTTA**C**AGTCGAATAAA
	lux box -36 -10

Figure 5.8: Sequences for variants of the pLuxI promoter used to tune amplify-and-forward gene circuit activity. WT refers to the wild-type promoter used in the sender-receiver circuit. Mutations made the the WT promoter are highlighted in pink. The *lux* box refers to the region of the pLuxI promoter that directly binds to LuxR.

exceed critical concentrations. One likely explanation is that the *lux* box mutations in V_3 (**Figure 5.8**) lowered the affinity of the pLuxI promoter to LuxR, thereby increasing the threshold concentration of LuxR needed to drive the positive-feedback loop. The strong linear trend of the dose-response may also indicate that amplification in V_3 is bottlenecked by low LuxR affinity to its cognate promoter. Neither the V_2 nor V_3 growth curves display a death phase indicating some relief from metabolic burden, but significant variability in stationary phase OD was observed at higher AHL concentrations in V_2. Finally, the V_4 variant has a dose-response curve similar to that of the WT promoter, with leakiness moderately attenuated only at the lowest AHL levels tested. Death phase dynamics and higher variability in OD were also observed in V_4.

We tested communication between senders and the V_3 repeaters within the FAIRY platform, with the sender cells at node N_0 and the V_3 strain in nodes N_{1-3} of the 4-node device (**Figure 5.10**). CFP expression in N_0 reached steady-state, exhibiting similar dynamics to the receiver and WT repeater experiments (**Figure 5.10a** and **Figure 5.5**). GFP expression in N_1 exhibited steady-state fluorescence approximately five-fold greater than its minimum, whereas N_2 and N_3 remained at baseline GFP expression levels (**Figure 5.10b**). Steady-state expression in N_1 may not correspond to saturated GFP production since a five-fold dynamic range is a fraction of the maximum observed GFP fold-change in V_3 in liquid culture. The lack of signal propagation from N_1 to subsequent nodes suggests that AHL is synthesized at N_1 at a lower rate than at the sender node, N_0. This is further supported by the restrained amplification indicated by the linear dose-response for V_3. We speculate that a lowered affinity between LuxR and pLuxI functions as a

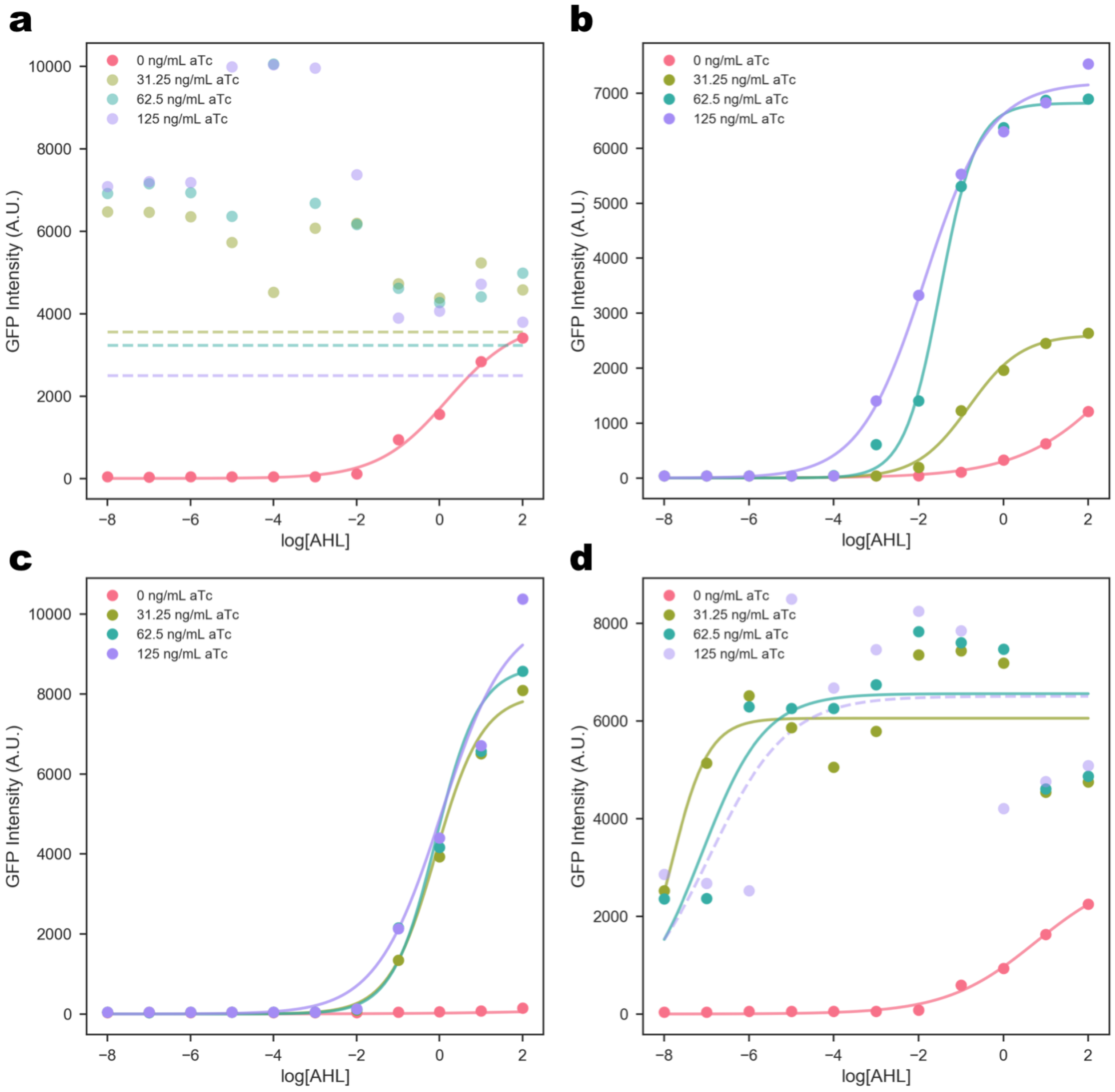

Figure 5.9: Dose-responses to AHL for all synthetic variants of the pLuxI promoter. **(a)** AHL dose-responses of the repeater variant V_1 at various aTc concentrations. Circles represent GFP expression measured at steady-state. Lines represent Hill equations fit to the data for each aTc condition (see **Table 5.1** for parameters and the coefficient of determination (R^2) of the fit). Increased transparency was used to plot data points for conditions in which a sigmoidal dose response was not observed. Dotted lines represent model fits for which the $R^2 < 0.5$. **(b)** AHL dose-responses of the repeater variant V_2 at various aTc concentrations (see **Table 5.1** for parameters and R^2 score). **(c)** AHL dose-responses of the repeater variant V_3 at various aTc concentrations (see **Table 5.1** for parameters and R^2 score). **(d)** AHL dose-responses of the repeater variant V_4 at various aTc concentrations (see **Table 5.1** for parameters and R^2 score).

rate-limiting step in the positive feedback; this can potentially act as a spatial 'bottleneck' in relay signaling within a series arrangement of nodes.

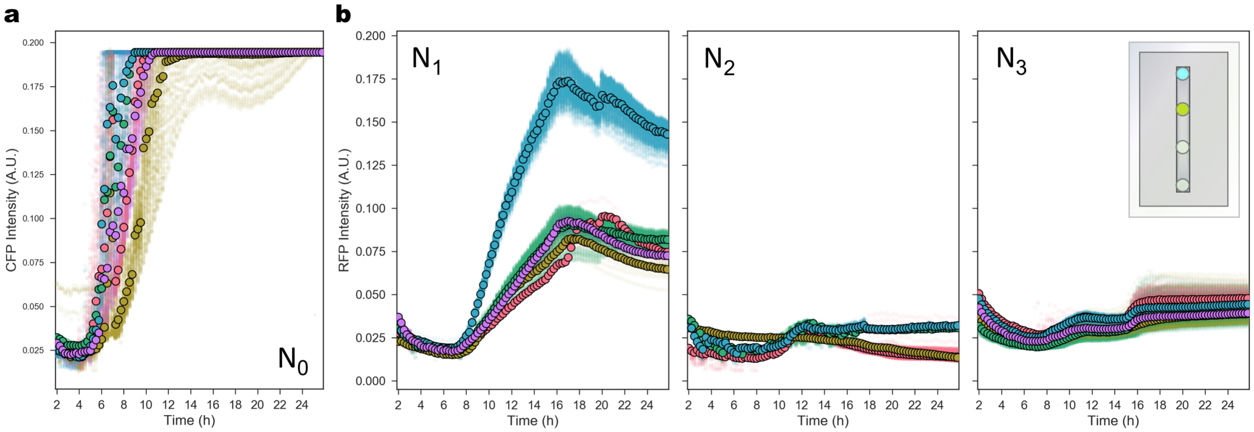

Figure 5.10: Gene expression dynamics for sender-V_3 repeater communication across nodes in the FAIRY device. **(a)** CFP expression at N_0 in the sender-V_3 experiment. Five technical replicates were collected for each node throughout the experiment. Each replicate is assigned a unique color, with the average fluorescence across the entire replicate shown by large bordered circles. The intensity across distinct 330 μm^2 regions within each replicate is shown by small transparent circles as an indicator of spatial variation across the node. **(b)** GFP expression at nodes N_{1-3} in the sender-V_3 experiment. Five technical replicates were collected for each node throughout the experiment. Each replicate is assigned a unique color, with the average fluorescence across the entire replicate shown by large bordered circles. The intensity across distinct 330 μm^2 regions within each replicate is shown by small transparent circles as an indicator of spatial variation across the node. The inset shows a schematic of the relay setup of the device.

To determine the temporal responsiveness of the V_3 strain, we subjected the sender-V_3 consortium to forced oscillations within the MISTiC device (see Experiment 15, **Appendix A**). Arabinose was pulsed first at a period of 1 h, followed by a period of 2 h, and finally continuously supplied towards the end of the experiment. The sender strain demonstrated oscillations that matched the period of the input for both phases of the experiment (**Figure 5.11a**). Curiously, the sender response displayed a slight inverse trend with distance, which not observed in the other experiments, indicating some pressure bias across the device. The receiver strain displays very low mean levels of gene expression and amplitudes compared to the sender. Nevertheless, the oscillations track with the input period and display similar amplitudes across all distances. We processed the power spectrum of the sender and receiver gene expression data to determine the signal-to-noise (SNR) ratio as elaborated in **Chapter 4**. Power spectra for the senders indicate no trend in CFP SNR in either the 1 h or 2 h forced oscillations (**Figure 5.12a,**top and **Figure 5.13a,**top). The power spectra for the V_3 repeaters don't display qualitative trends across separation distance for either experiment (**Figure 5.12a,**bottom and **Figure 5.13a,**bottom). However, at both oscillation frequencies, the V_3 repeaters demonstrate a non-monotonic trend across distance, with the SNR of the 50 μm distance significantly higher than at the other positions (**Figure 5.12b,**bottom and **Figure 5.13b,**bottom). The experiment needs to be repeated to verify the non-monotonic trend in SNR. The MISTiC experiment demonstrates that the 100-fold greater threshold of the V_3 strain lowers the gain of the signal substantially but maintains a temporal response. The slow increase in gene expression for the 100 μm and 250 μm distances indicates that some degree of signal amplification could be attenuating the effects of spatial separation over time. Further experiments that account for these factors are necessary to determine whether the high threshold of the V_3 confers a noise-filtering function.

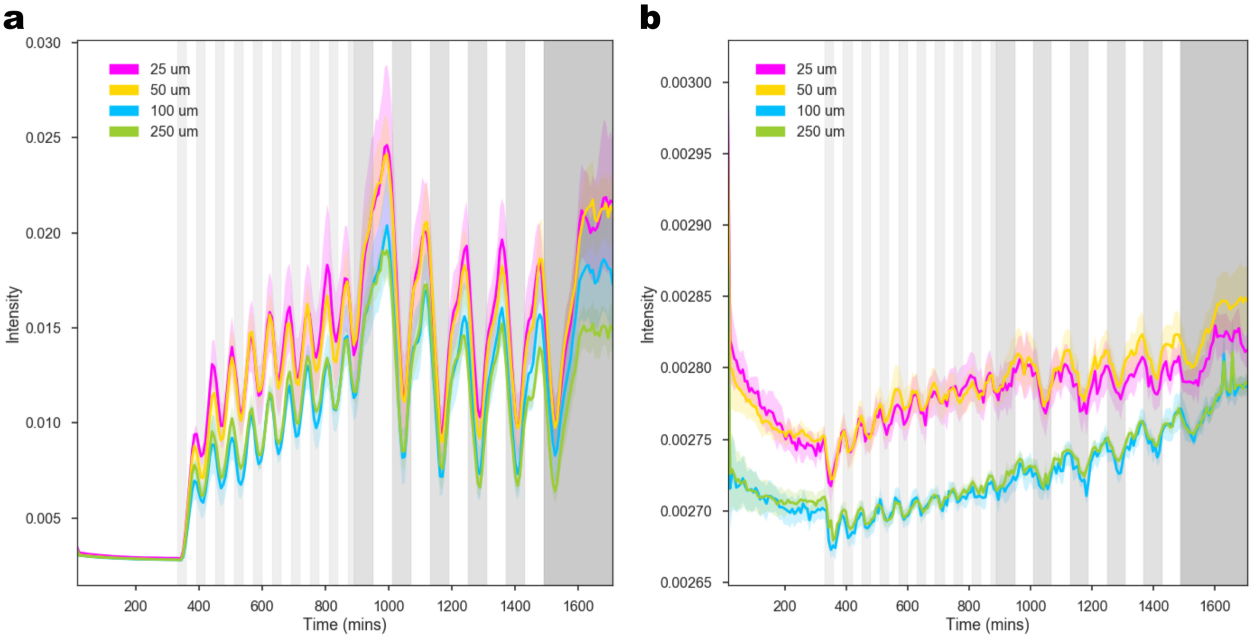

Figure 5.11: Forced sender-V$_3$ oscillations at a period of 1 h. (a) CFP as a function of time in response to an oscillatory arabinose input. Grey shaded regions indicate pulses of 0.1% arabinose, first applied with a period of 1 h, and switched to a period of 2 h halfway through the experiment. Colored shaded regions represent one standard deviation from mean. (b) GFP as a function of time in response to an oscillatory arabinose input.

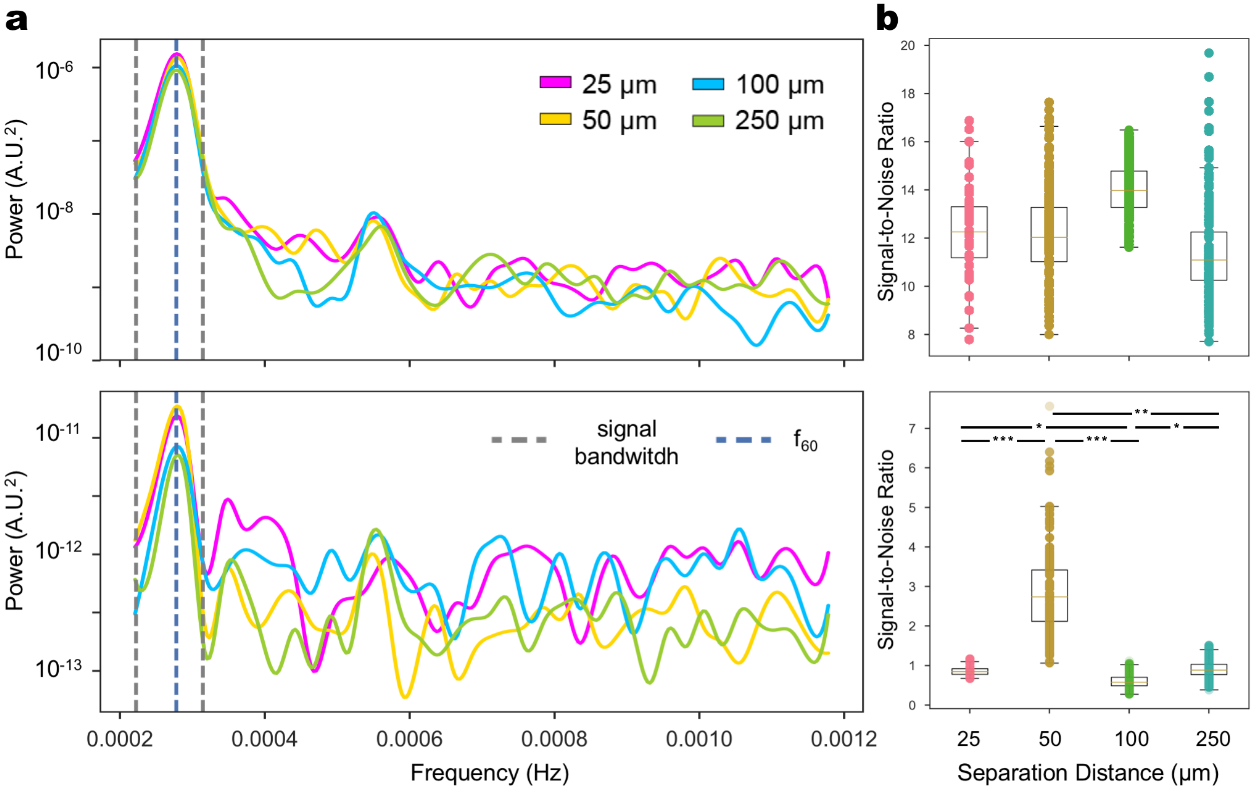

Figure 5.12: Sender and V_3 repeater power spectra and signal-to-noise trends for a 1 h forced oscillator. **(a)** Top: Mean CFP power spectra (sender strain) in response to an oscillating input with a period of 1 h (blue dashed line). Power spectra were calculated using the Welch method with a Hamming windowing function at steady-state for 399–798 min (see **Methods**). The region bound by gray dotted lines denotes a bandwidth of 53-75 min around the expected input period of 60 min. Bottom: Mean GFP power spectrum (V_3 strain) in response to an input period of 1 h (blue dashed line) for 399–798 min. The region bound by gray lines denotes a bandwidth of 53-75 min around the expected input frequency. **(b)** Signal-to-noise (SNR) ratios computed using bootstrapped power spectra for CFP (top) or GFP (bottom) for each distance (**Methods**) for a 1 h oscillator. Horizontal lines within boxes denote the median and upper and lower edges represent the upper and lower quartiles, respectively. Upper and lower whiskers represent the 95th and 5th confidence intervals, respectively. Horizontal lines with stars denote statistically significant differences ($P < 0.05$) based on one-tailed bootstrapped hypothesis testing. $*P < 0.05, **P < 0.01$, and $***P < 0.001$ (see **Appendix A**).

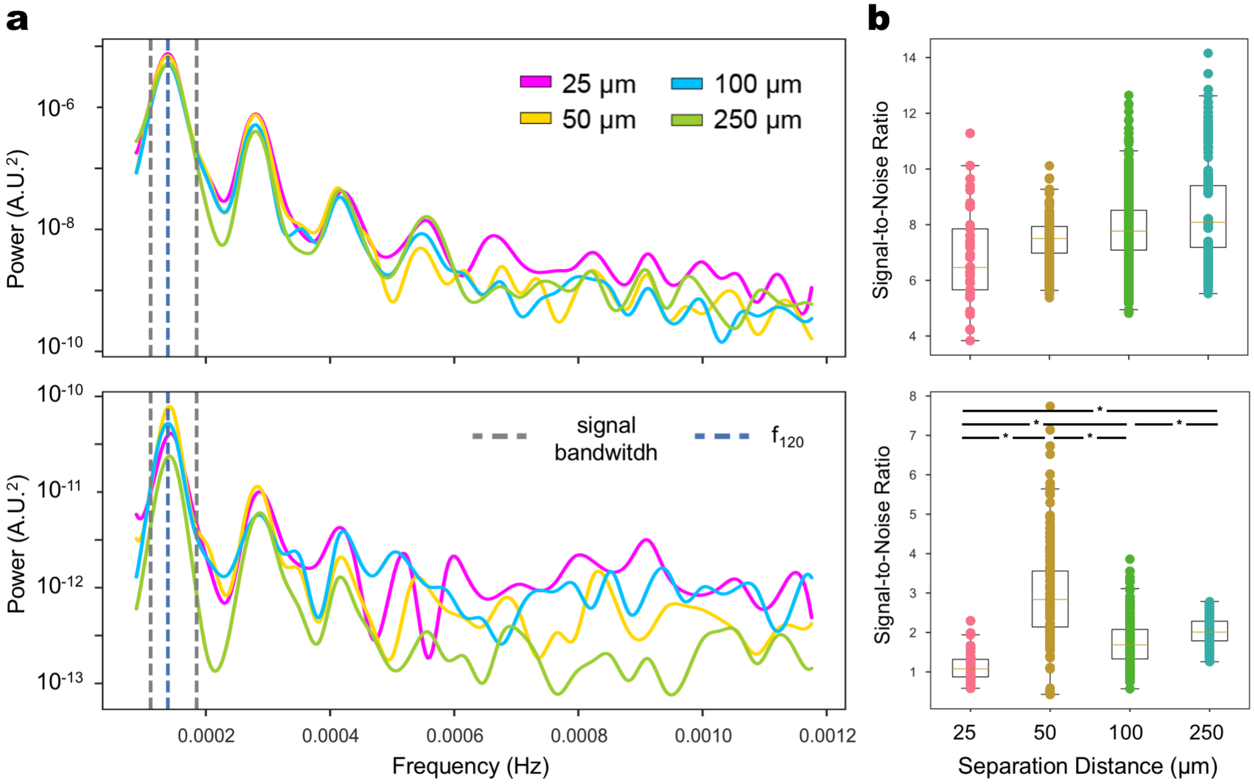

Figure 5.13: Sender and V_3 repeater power spectra and signal-to-noise trends for a 2 h forced oscillator. **(a)** Top: Mean CFP power spectra (sender strain) in response to an oscillating input with a period of 2 h (blue dashed line). Power spectra were calculated using the Welch method with a Hamming windowing function at steady-state for 994–1400 min (see **Methods**). The region bound by gray dotted lines denotes a bandwidth of 53-75 min around the expected input period of 60 min. Bottom: Mean GFP power spectrum (V_3 strain) in response to an input period of 1 h (blue dashed line) for 399–798 min. The region bound by gray lines denotes a bandwidth of 90-150 min around the expected input period of 120 min. **(b)** Signal-to-noise (SNR) ratios computed using bootstrapped power spectra for CFP (top) or GFP (bottom) for each distance (see **Methods**) for a 2 h oscillator. Horizontal lines within boxes denote the median and upper and lower edges represent the upper and lower quartiles, respectively. Upper and lower whiskers represent the 95th and 5th confidence intervals, respectively. Horizontal lines with stars denote statistically significant differences ($P < 0.05$) based on one-tailed bootstrapped hypothesis testing. $*P < 0.05, **P < 0.01$, and $***P < 0.001$ (see **Appendix A**).

5.3 Methods

Cell cloning. Sender and repeater plasmids (see **Appendix B**) were constructed using standard Gibson assembly protocols with primers synthesized by Integrated DNA Technologies and verified by Sanger sequencing (Functional Biosciences). The sender (A6c_LuxI_CFP) and repeater (E2c_LuxR_wtLuxI_GFP) plasmids were transformed into *E. coli* strains BW27783 [116] and MG1655Z1 [117], respectively (see **Appendix B**). Promoter variants V_{1-4} were made using inverse phosphorylation PCR that amplified from the pLuxI region using primers (Integrated DNA Technologies) designed with the appropriate mutations. The ligated plasmids were verified by Sanger sequencing (Functional Biosciences) and transformed into the *E. coli* strain MG1655Z1 [117].

Microwell experiments to determine dose-responses. An initial set of cultures were inoculated into LB media (Lennox, Sigma-Aldrich) containing 25 μg/mL chloramphenicol (Sigma-Aldrich) and cultured overnight at 37 °C with shaking. After approximately 16 h, the cells were diluted to an OD600 of 0.01 to make a 25 mL LB media solution containing 25 μg/mL chloramphenicol. For all experiments comparing receivers and repeater variatns, the microwell plate was split such that the top four rows corresponded to one strain, and the bottom four rows to another. For these experiments, a 10-fold serial dilution of 3-oxo-C6-HSL or AHL (Sigma-Aldrich) was prepared starting at 5000 μM AHL and proceeding for 10 steps, leaving the last step as a 0 μM AHL condition. A 2-fold serial dilution of anhydrotetracycline hydrochloride, or aTc, (Cayman Chemicals), was prepared starting at 6250 ng/mL and diluted for 2 steps, leaving the last as a 0 ng/mL aTc condition. 192 μL of the cell solution was pipetted into all 96 wells of a black, clear-bottom 96-well microwell plate (Greiner Bio-One). The four dilutions of aTc were pipetted across all columns for the top four rows, and repeated for the bottom four rows. The 12 dilutions of AHL were pipetted across all rows such that each AHL concentration corresponded to a single column. For the experiment assaying WT repeater activity at < 30 ng/mL aTc, every well on the plate was filled with 192 μL WT repeater cells. 10-fold AHL serial dilutions were prepared starting at 5000 μM proceeding for a total of 8 steps including the 0 μM condition, and pipetted across columns of the 96-well plate containing cells. 5-fold serial dilutions of aTc were prepared across a total of 12 steps including the 0 ng/mL condition, and pipetted down the rows of the plate. After setup, the plates were covered with a gas-permeable polyurethane sealing membrane (Breathe-Easy) and loaded into a plate-reader (Tecan, Spark). The instrument was programmed to incubate cells at 37 °C with continuous orbital shaking while measuring OD600 growth and emissions for GFP (488 nm (ex), 507 nm (em)), and/or RFP (589 nm (ex), 612 nm (em)) depending on the strains being assayed.

Dose-response curve fitting. Model fitting code was written in Python using *scipy.optimize* functions to fit experimental data to the standard Hill equation:

$$P = \alpha \frac{S^{n_{FP}}}{K_{FP}^{n_{FP}} + S^{n_{FP}}} \tag{5.1}$$

The parameter values for α, n_{FP}, and K_{FP} corresponding to the optimized fit for each dose-response curve are listed in **Table 5.1**.

Device fabrication. The MISTiC and FAIRY devices were fabricated according to the methods elaborated in **Chapter 1**. Prior to each experiment, the MISTiC device was flushed with 0.5% Tween 20 (Sigma-Aldrich) to prevent cells from adhering to the device.

Cell culturing. An initial set of cultures were inoculated into LB media (Lennox, Sigma-Aldrich) containing 25 μg/mL chloramphenicol (Sigma-Aldrich) and cultured overnight at 37 °C with shaking. After approximately 16 h, 1 μL of the cultures were diluted into 3 mL LB media containing 25 μg/mL chloramphenicol and incubated at 37 °C with shaking to early stationary phase (OD600 0.7–1.1). For MISTiC experiments, we measured the OD600 of these cultures and centrifuged 1 mL at 3500 × g. The supernatant was removed and the pellet was resuspended to a final OD600 of approximately 20. For FAIRY experiments, the cultures were diluted to an OD600 of approximately 0.05. Once agar pads were levelled in the FAIRY nodes, 1 μL of the cultures were pipetted onto each node.

Experimental setup for FAIRY devices. Once the agar pads of the FAIRY device were sealed with a glass slide (Thermo-Fisher), the device was transfered to a custom-designed incubation chamber that maintained the temperature at 37 °C for the duration of the experiment. Fluorescence and phase-contrast images were collected using a Ti-E Eclipse inverted microscope (Nikon) at periodic time intervals. Each node in the device was imaged in five different regions at 20 × magnification. Fluorescence was imaged using the following filters (Chroma): GFP: 470 nm/40 nm (ex), 525/50 nm (em) or RFP: 560 nm/40 nm (ex), 630/70 nm (em).

Data analysis for FAIRY experiments. Custom code in Python was written to segment the microscopy images into 475 slices, each corresponding to a region of approximately 330 μm^2. The fluorescence intensity was determined across each region for every timepoint. The coefficient of variation was then computed to determine the variability in fluorescence within each region over time. The bottom 10th percentile of the coefficient of variation across all 475 slices was logged for each replicate. Of this set, the lowest value was used as a threshold to omit regions that displayed lower coefficients of variation, indicating areas borders of the node, dark regions or artifacts, and other areas that remained without cells for the duration of the experiment, and which therefore saw no changes in fluorescence. Because this threshold is selected relative to the mean and variation in each node, it does not exclude cells that were present but which remained in the OFF state. The mean fluorescence for each replicate at each timepoint was determined by averaging over all the filtered slices.

Sender-V_3 forced oscillator experiment in MISTiC. The setup for the MISTiC device for the sender-V_3 experiment was identical to that of the sender-receiver experiments in **Chapter 3**, with the exception of the syringe pump program used to alternate arabinose induction. The forced oscillation experiments used 10 mL syringes to extend the duration of the experiment. Oscillations were applied once the growth chambers were filled with cells (see **Appendix A**). Flow rates of the 0.1% arabinose (inlet I_{22}) and 0% arabinose (inlet I_{21}) were alternated out of phase between 200 and 0 μL/h for a period of time. One of the receiver inlets (I_{11}) flowed continuously at a rate of 200 μL/h and the other inlet (I_{12}) was set to 0 μL/h for the duration of the experiment. We used custom Python code for image alignment and segmentation, as elaborated in **Chapter 3**. The methods for computing the average fluorescence intensity for each growth chamber and excluding outliers were identical to those described in **Chapter 3**. To calculate the SNR, a moving mean computed over 20 time points was subtracted from the data. The power spectra for each replicate was calculated using Welch's method (Python) with a Hamming window applied across the length of the time-series. The power spectra were filtered to exclude frequencies lower than the signal bandwidth. The signal was defined as the total power of the signal bandwidth. The noise was computed as the total power of frequencies larger than the signal bandwidth. The power spectra for all the replicates for a given interaction channel length were randomly sampled with replacement 10,000 times. For each iteration, the SNR ratio was computed by dividing the signal by the noise. Bootstrap hypothesis testing, as described in **Chapter 3**, was used to compute P-values.

Chapter 6

Spatiotemporal Influences on Metabolic interactions

In microbial communities, the transition to coordinated behaviors often occur when the collective benefits outweigh the cost of individuality [83, 90]. Collective benefits include allocation of specialized functions such as metabolite production or toxin breakdown [96, 107, 112], developing protective infrastructure such as biofilms [83, 107, 122], bet-hedging to lower risk [80], or exchanging genetic material for evolutionary advantages [88]. These coordinated functions reflect a global shift in gene regulation that can lower energetic costs and maximize fitness [66,90]. We sought to engineer microbial interactions that could regulate a global variable such as cell growth rate. To do this, we used synthetic auxotroph strains, each engineered to lack the ability to synthesize a different essential amino acid. This compels a mutualism between the strains as they must cross-feed to survive.

Cross-feeding, like various other microbial community functions, involves the diffusion of metabolites between cells. The spatiotemporal factors that govern the movement of metabolites and resources across microbial populations are closely intertwined with the ecological interactions mediated by these molecules [70]. For instance, mutualistic interactions between microbial species can spatially exclude ‘cheater’ populations [142], and the benefit gained from this spatial arrangement may even balance the otherwise puzzling cost of mutualism to individual microbes [66, 143]. Additionally, microorganisms constantly release and uptake nutrients and metabolites from their surroundings. These local variations in resources, signals, or toxins can over time shape the ecological interaction network [70, 134].

Here we use MISTiC to investigate the effects of spatial separation on the coordination of growth via cross-feeding in a two member auxotroph community. While the engineered mutualism between strains can be considered a positive feedback loop, it interfaces with an underlying GRN that regulates growth as a function of amino acid concentrations. In this scenario, the behavior of the positive feedback loop is contingent on both the environmental context and the intracellular requirements of the cell. By testing the system across varying environmental conditions and spatial configurations we attempt to abstract the logic of the underlying GRNs.

6.1 The effect of spatial separation on a cross-feeding mutualism

To investigate how spatial separation influences metabolic interactions in microbial communities, we studied a synthetic *E. coli* consortium composed of a phenylalanine ($\Delta pheA$) and methionine ($\Delta metA$) auxotroph strain. Phenylalanine (F) and methionine (M) auxotrophies are predicted to be prevalent in microbial communities and are two of the most energetically costly amino acids to synthesize in E. coli [144].

We characterized the community dynamics in batch culture by inoculating the strains at three initial ratios (50% $\Delta metA$, 50% $\Delta pheA$ or 90% $\Delta metA$, 10% $\Delta pheA$, or the reciprocal), in minimal media lacking M and F, and performed periodic transfers of the community to fresh media (see **Methods** at the end of this chapter). Irrespective of the initial strain proportion, the co-culture converged to a $\Delta pheA$ dominated steady-state (**Figure 6.1a**). For a sustained 24 h transfer time, the community exhibited a decreasing trend in OD600 and eventually collapsed after the third passage (**Figure 6.1b**). However, community growth was maintained over three passages by switching the final passage to a 48 h incubation time, suggesting that a critical cell density was required to achieve ecological stability (**Figure 6.1c**). Therefore, in a batch culture environment that preserves a critical population size, the community exhibited growth and stable coexistence over multiple passages with $\Delta pheA$ dominating the community.

In MISTiC, the population-level growth rate can be inferred by the rate of dilution of an inducible and stable fluorescent reporter due to cell growth [94,145]. We used this method to determine each strain's maximum growth rate in a spatially structured and continuous culture environment by labeling $\Delta metA$ and $\Delta pheA$ with isopropyl β-D-1-thiogalactopyranoside (IPTG)-inducible GFP and RFP, respectively (**Figure 6.2a**). An interaction was quantified as the fold change of each strain's maximum growth rate in the 25 to 250 μm condition. Microbial interactions are frequently deciphered by evaluating the difference of a strain's growth parameters in monoculture and co-culture conditions [76, 146]. In MISTiC, the sign and strength of the interaction could be deduced as a function of spatial separation. In the presence of all amino acids, $\Delta metA$ and $\Delta pheA$ exhibited similar average doubling times of 80 and 86 min, respectively, across all interaction channel lengths (**Figure 6.2b,c** and **Figure 6.3**), indicating a neutral interaction network (**Figure 6.10**) (see Experiment 6, **Appendix A**).

In the absence of M and F, $\Delta metA$ grew very slowly (1128 min doubling time) across all distances (**Figure 6.2b** and **Figure 6.4a,c**). By contrast, the doubling time for $\Delta pheA$ substantially increased with distance (**Figure 6.2c** and **Figure 6.4b,d**) (see Experiment 7, **Appendix A**). Therefore, the growth rate of $\Delta pheA$ was highly sensitive to distance from the $\Delta metA$ strain and not the reciprocal, highlighting a major difference in the strength and operating regime of the interactions (**Figure 6.10**). The maximum growth rate of $\Delta pheA$ was delayed by 43 min in the 25 to 250 μm condition (**Figure 6.2c**,inset), demonstrating that the timing of the transition from lag phase to growth was also distance-dependent.

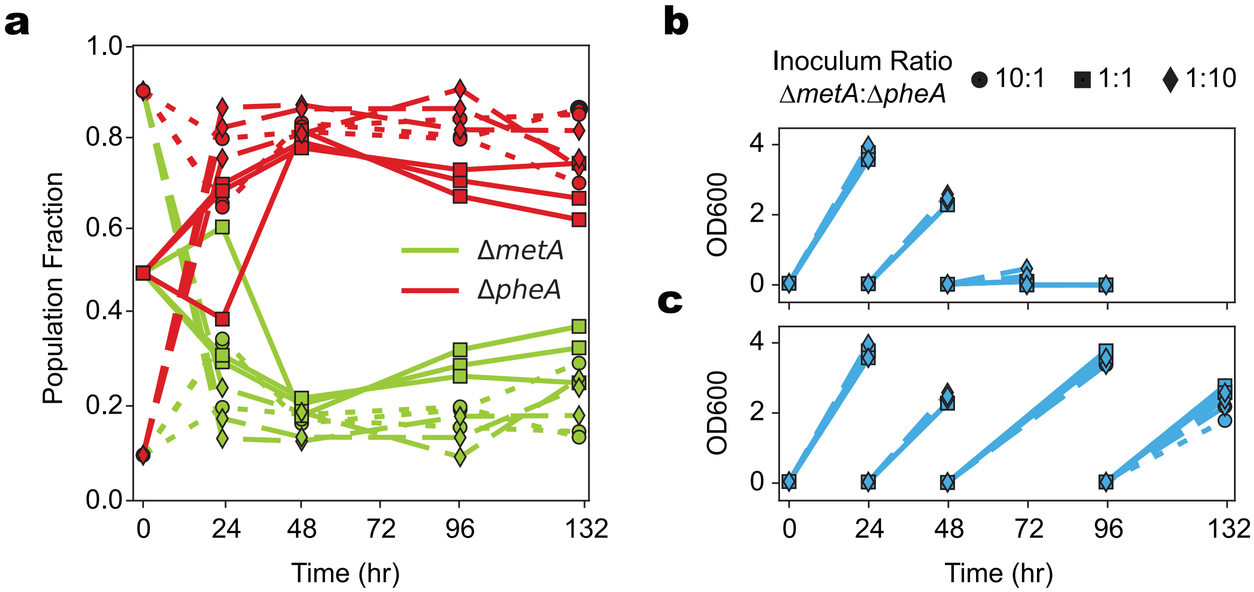

Figure 6.1: Population dynamics of the Δ*metA*-Δ*pheA* consortium in batch culture. **(a)** Fraction of each strain as a function of time. Marker and line styles correspond to different initial ratios of Δ*metA* to Δ*pheA*. Circles and dotted lines represent 10:1, squares and solid lines represent 1:1, and diamonds and dashed lines represent 1:10. **(b)** OD600 measurements as a function of time for a passaging period maintained at 24 hours. **(c)** OD600 measurements as a function of time for a second condition where the incubation period after the second passage was extended to 48 h. The number of cells counted for each condition ranged between 250-3960.

We next explored how titrating all amino acid concentrations influenced the inferred interaction network within MISTiC (see Experiments 12–14, **Appendix A**). The distance-dependent growth change of Δ*pheA* decreased with amino acid availability (**Figure 6.5b,d,f,h**), whereas this pattern was not evident for Δ*metA* (**Figure 6.5a,c,e,g**). These data demonstrate that trace amino acids were sufficient to eliminate the growth benefit provided by Δ*metA*.

6.2 Single-cell analysis of mixed auxotrophs

We next investigated the growth of Δ*pheA* and Δ*metA* in mixed conditions withing the MISTiC microenvironment for comparison to the spatially separated context. Equal proportions of Δ*metA* and Δ*pheA* were introduced into the growth chambers and cultured in the absence of M and F (see Experiment 8, **Appendix A**). Single-cell segmentation and tracking was performed to distinguish the strains within mixed

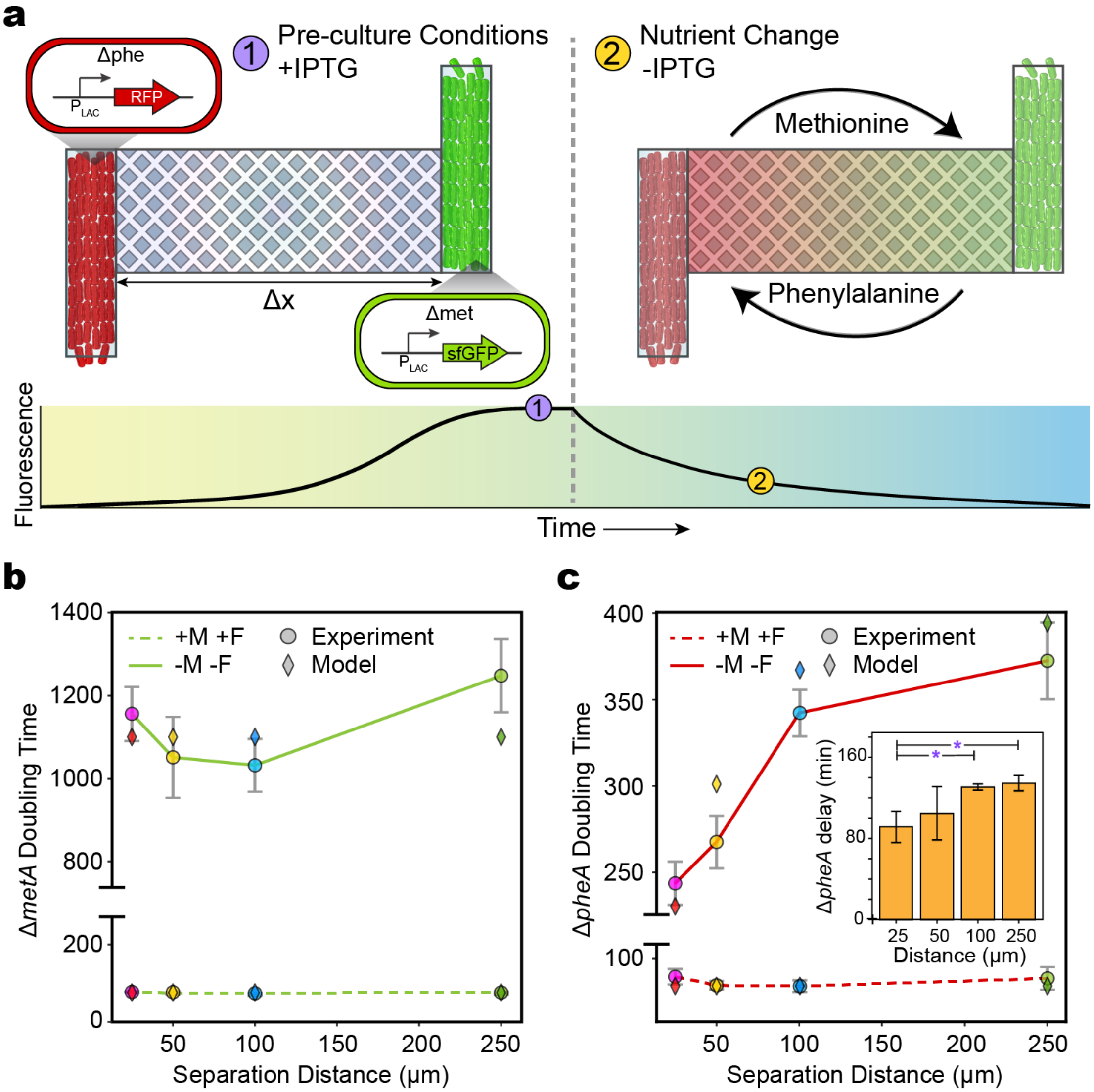

Figure 6.2: Spatial and temporal modes of amino acid cross-feeding in a synthetic *E. coli* consortium. **(a)** Schematic of the experimental design. $\Delta metA$ and $\Delta pheA$ are labeled with IPTG-inducible fluorescent reporters. The strains are initially cultured in the presence of IPTG. At the denoted time, IPTG is removed and the media condition is altered. The maximum growth rate is inferred based on the rate of decay of the fluorescence signal. Relationship between distance and population-level doubling times of **(b)** $\Delta metA$ or **(c)** $\Delta pheA$. The dashed and solid lines represent presence and absence of methionine (M) and phenylalanine (F), respectively. Diamonds represent the model fits. Inset: The time of maximum $\Delta pheA$ growth rate in media lacking M and F. Horizontal lines denote a statistically significant difference ($P < 0.05$) based on one-tailed bootstrap hypothesis testing. $*P < 0.05, **P < 0.01$, and $***P < 0.001$ (see **Appendix A**).

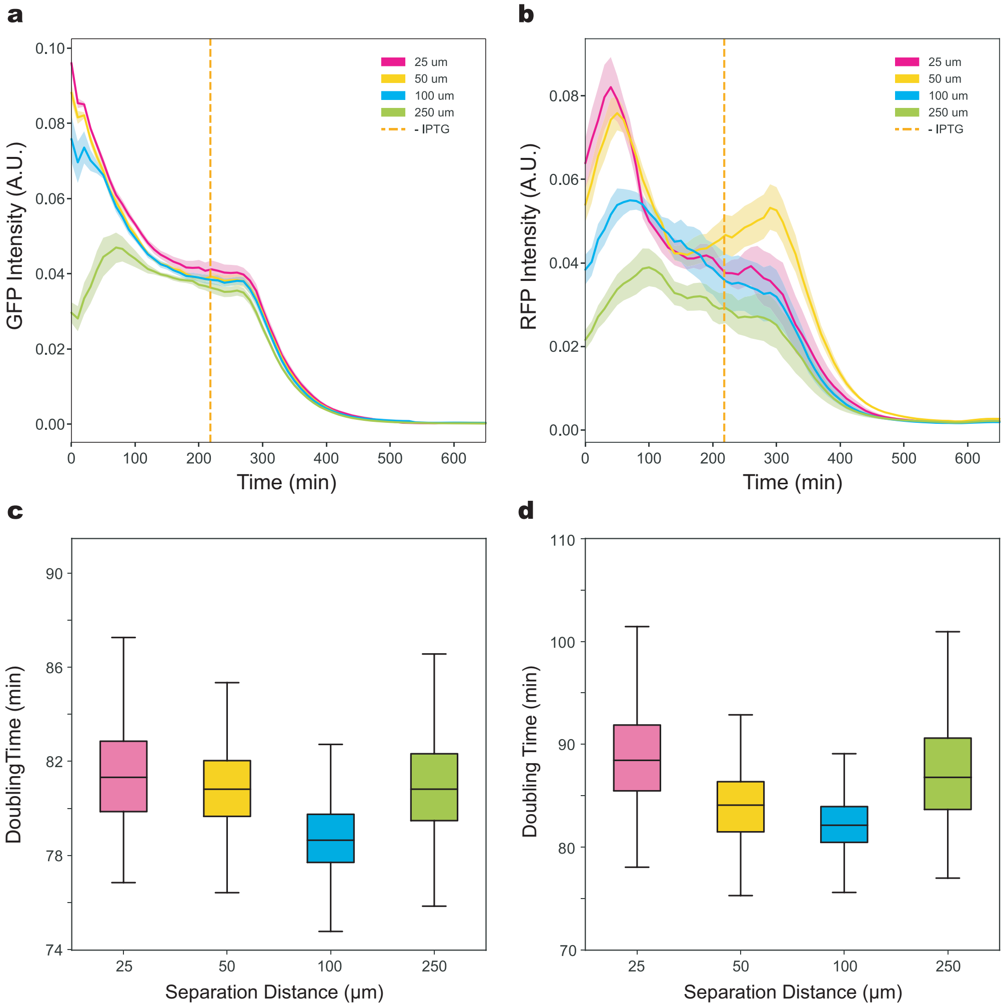

Figure 6.3: Fluorescence time-series and doubling time distributions for the +M +F condition. **(a)** GFP fluorescence in the $\Delta metA$ strain as a function of time in media supplemented with all amino acids. The dashed line indicates the time of the media switch from media containing IPTG to media lacking IPTG. Solid lines and shaded regions represent the mean and one standard deviation from the mean, respectively. **(b)** RFP fluorescence in the $\Delta pheA$ strain over time in media supplemented with all amino acids. **(c)** Box plot of cell doubling times for $\Delta metA$ at each interaction channel length. Horizontal lines within boxes depict the median and upper and lower edges represent the upper and lower quartiles, respectively. Upper and lower whiskers represent the 95th and 5th confidence intervals, respectively. Differences between the distributions represented in the box plot were not statistically significant based on one-tailed bootstrap hypothesis testing. **(d)** Box plot of the $\Delta pheA$ doubling times at each interaction channel length. Differences between the distributions represented in the box plot were not statistically significant based on one-tailed bootstrap hypothesis testing.

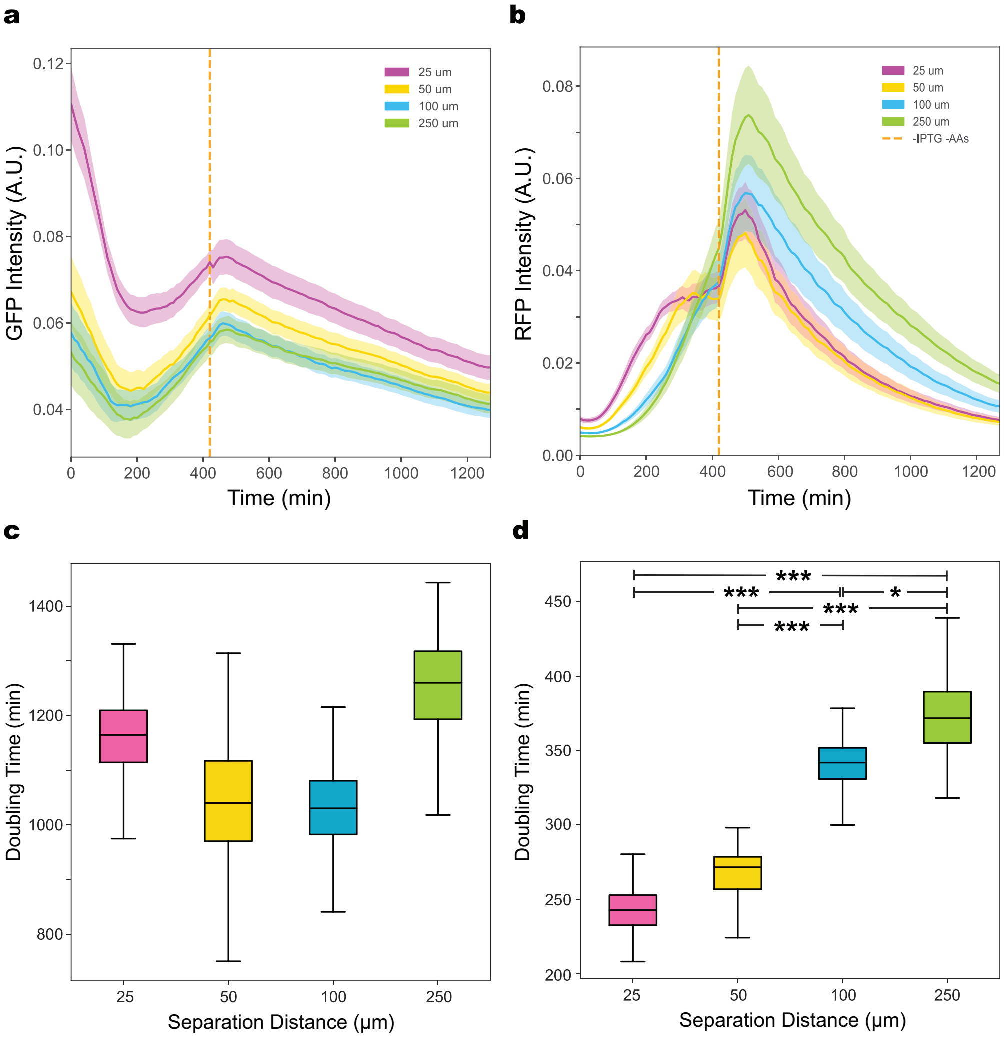

Figure 6.4: Fluorescence time-series and doubling time distributions for the -M -F condition. **(a)** GFP fluorescence over time in the $\Delta metA$ strain at different distances from the partner strain ($\Delta pheA$). The dashed line represents the time when the media was switched from pre-culture to test conditions. Solid lines represent the mean and shaded regions represent one standard deviation from the mean. **(b)** RFP fluorescence over time in the $\Delta pheA$ strain at different distances from the partner strain ($\Delta metA$). **(c)** Box plot of the cell doubling times for the $\Delta metA$ strain. Horizontal lines within boxes denote the median, and upper and lower edges represent the upper and lower quartiles, respectively. Upper and lower whiskers represent the 95th and 5th confidence intervals, respectively. Differences between the distributions represented in the box plot were not statistically significant based on one-tailed bootstrap hypothesis testing. **(d)** Box plot of the doubling times for $\Delta pheA$ strain. Horizontal bars with stars indicate a statistically significant difference ($P < 0.05$) based on one-tailed bootstrap hypothesis testing. $*P < 0.05, **P < 0.01$, and $***P < 0.001$ (see **Appendix A**).

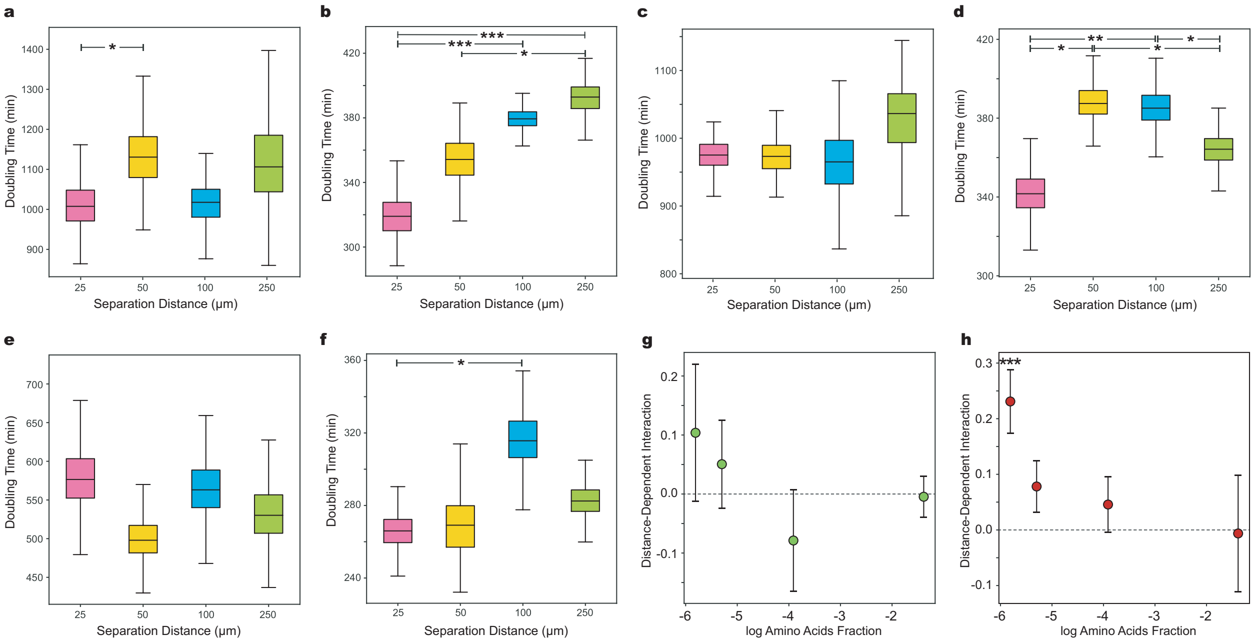

Figure 6.5: Growth rates of amino-acid auxotrophs across different concentrations of supplemented amino acids. For all box plots in the figure, horizontal lines within boxes denote the median and upper and lower edges represent the upper and lower quartiles, respectively. Upper and lower whiskers represent the 95th and 5th confidence intervals, respectively. For all panels displaying box plots, the horizontal bars denote a statistically significance difference (P < 0.05) based on one-tailed bootstrap hypothesis testing. **(a)** Box plot of the doubling times for the $\Delta metA$ strain at 0.003X amino acid (AA) concentration. **(b)** Box plot of the cell doubling times for the $\Delta pheA$ strain for 0.003X AA. **(c)** Box plot of the cell doubling times for the $\Delta metA$ strain with 0.005X AA. **(d)** Box plot of the cell doubling times for the $\Delta pheA$ strain with 0.005X AA. **(e)** Box plot of the cell doubling times for the $\Delta metA$ strain with 0.02X AA. **(f)** Box plot of the cell doubling times for the $\Delta pheA$ strain with 0.02X AA. **(g)** Relationship between the fraction of all amino acids and the sensitivity of growth of $\Delta metA$ to spatial separation from $\Delta pheA$. The distance-dependent interaction value is defined as the ratio of the minimum doubling time of each strain in the 25 μm to 250 μm condition $(D_{25}D_{250}^{-1})-1$. Error bars represent one standard deviation from the mean interaction value. A positive interaction was greater than zero and a negative interaction was less than zero. No data points showed statistically significant differences ($P < 0.05$) between D_{25} and D_{250}, using a two-sided t-test. **(h)** Relationship between the fraction of all amino acids and the sensitivity of growth of $\Delta pheA$ (interaction strength) to spatial separation from $\Delta metA$. Error bars represent one standard deviation from the mean interaction value. Three stars (***) indicate P = 0.00040 for the difference in D_{25} and D_{250} using a two-sided t-test. No other data points showed statistically significant differences ($P < 0.05$) between D_{25} and D_{250} (see **Appendix A**).

communities and quantify single-cell growth rates (**Figure 6.6a**). The interaction channel length did not contribute to the variation in the growth rates of $\Delta metA$ and $\Delta pheA$ (**Figure 6.6b,c**). The average $\Delta metA$ and $\Delta pheA$ growth rates within a chamber decreased over time but remained non-zero for the majority of the experiment (**Figure 6.7a**). In addition, the percentage of growing cells across all growth chambers in the mixed condition was larger than 40% for both strains for the majority of the experiment (**Figure 6.7a,** inset). To evaluate the difference in each strain's growth rate in the co-culture compared to monoculture, similar MISTiC experiments were performed for $\Delta metA$ and $\Delta pheA$ (see Experiments 9 and 10, **Appendix A**). The co-culture growth rates were significantly higher than their respective monoculture conditions, demonstrating a mutual growth benefit in mixed conditions within MISTiC (**Figure 6.7a**).

The Spearman's correlation between the growth rate of each strain and the fraction of the growth chamber occupied by the partner strain was used to quantify the effect of the partner strain's abundance on growth rate (**Figure 6.7b,** inset). Both strains exhibited statistically significant and non-zero Spearman correlations for the majority of the experiment, indicating a mutualism. The Spearman's correlation was consistently higher for $\Delta pheA$, indicating a stronger dependence of the growth rate of $\Delta pheA$ on the abundance of $\Delta metA$ than the reciprocal, consistent with growth measurements in the spatially separated condition (**Figure 6.2b,c**). In spite of the growth rate difference, the average ratio of the two strains approached a stable steady-state (**Figure 6.6d**). As the percentage of dividing cells (**Figure 6.6e**) was significantly lower than the percentage of growing cells (**Figure 6.7a,** inset) for both strains, cell elongation was the dominant mode of growth in these conditions. In addition, growth rates did not vary as a function of the position of single cells within the growth chambers (**Figure 6.6f**). These findings illustrate the ability of MISTiC to resolve subpopulation growth heterogeneities based on single-cell data.

6.3 Elucidating the interaction network of a $\Delta metA$ and $\Delta pheA$ consortium

To determine how rescuing the growth of $\Delta metA$ impacted the interaction network, we examined the growth rates of the spatially separated strains in the presence of all amino acids except F (see Experiment 12, **Apppendix A**). The doubling time of $\Delta metA$ was similar to its doubling time in the presence of M and F across all distances (**Figure 6.8a** and **Figure 6.9a,d**). The rate of change of RFP fluorescence was biphasic, indicating that $\Delta pheA$ had two growth modes in this condition (**Figure 6.9b,c**). The $\Delta pheA$ doubling times in the first growth phase did not change across distance, yielding a neutral interaction network (**Figure 6.10** and **Figure 6.9e**). The second $\Delta pheA$ growth phase displayed a moderately competitive growth trend across a tenfold change in distance (**Figure 6.8a**, **Figure 6.9f**, and **Figure 6.10**). The positive interaction from $\Delta metA$ to $\Delta pheA$ was abolished by rescuing $\Delta metA$ growth, suggesting that rapid growth of $\Delta metA$ resulted in a substantial decrease in the release rate of F.

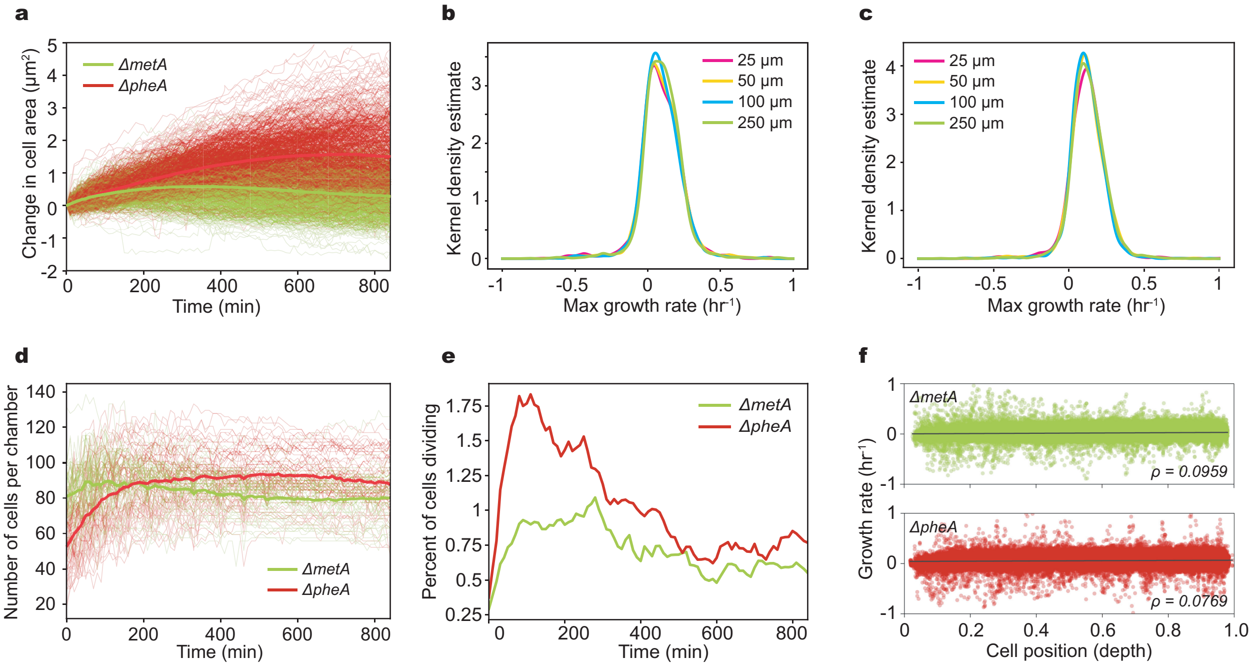

Figure 6.6: Quantification of single-cell growth in the mixed auxotroph condition. **(a)** Change in cell area as a function of time for $\Delta metA$ (n = 937) and $\Delta pheA$ (n = 662). The change in cell area is defined as the cumulative change in cross-sectional area of each cell from its initial value at the time of the media switch. Thin lines represent individual cells and bold lines represent strain averages. **(b)** Kernel density estimate distribution of $\Delta metA$ single cell growth rates over 14 hr post media switch in the mixed auxotroph experiment for each interaction channel length. **(c)** Kernel density estimate distribution of $\Delta pheA$ single cell growth rates.**(d)** Total number of $\Delta metA$ and $\Delta pheA$ cells in each growth chamber as a function of time. Bold lines represent the average number of cells for each strain across all growth chambers. **(e)** Percent of $\Delta metA$ or $\Delta pheA$ cells dividing as a function of time. The fraction of dividing cells was computed using a window spanning 60 min starting at each time point, which was then divided by the average number of $\Delta metA$ or $\Delta pheA$ cells in the window. **(f)** Scatter plot of the correlation between the growth rate and depth position of individual $\Delta metA$ (n=165408) and $\Delta pheA$ (n=193970) cells in a mixed community. Positions zero and one represent the outermost and deepest regions of the growth chamber, respectively, relative to the main channels. Solid bold lines show simple linear regression between maximum growth rate and chamber position. The Pearson correlation coefficient is 0.0959 ($P < 0.001$) for $\Delta metA$ and 0.0769 ($P < 0.001$) for $\Delta pheA$.

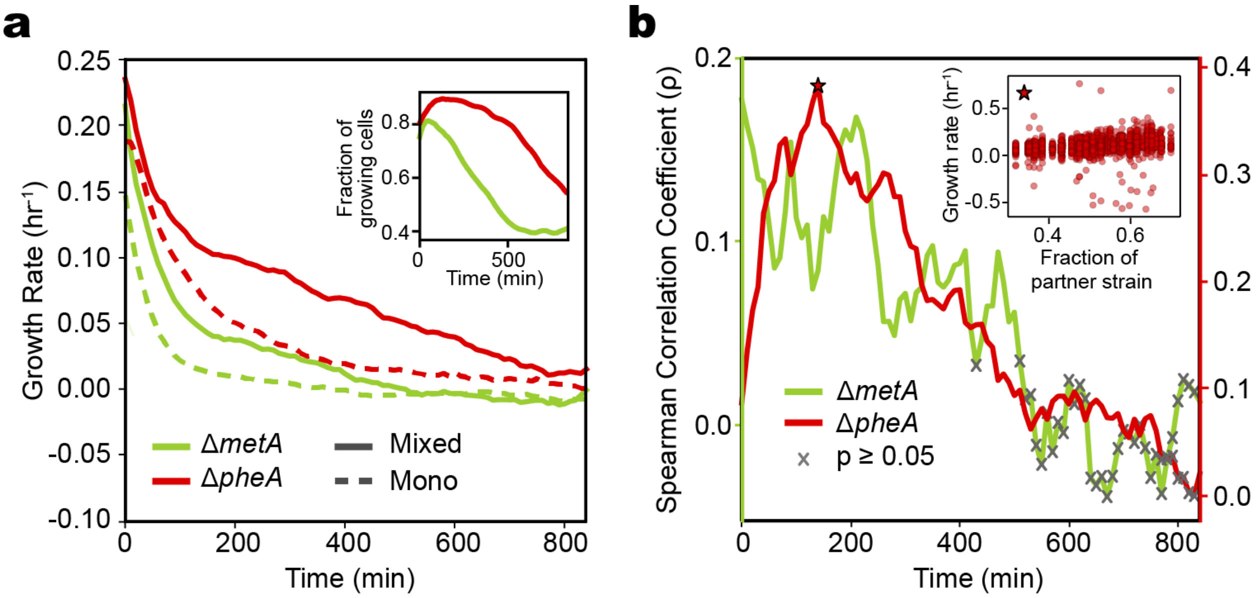

Figure 6.7: Growth correlates of a mixed $\Delta metA$-$\Delta pheA$ community in MISTiC. (a) Relationship between time and the average single-cell growth rates of $\Delta metA$ and $\Delta pheA$ in a mixed community (solid line) or monoculture (dashed line) in media lacking M and F. Inset: fraction of cells with non-zero growth rates as a function of time. **(b)** Spearman's correlation coefficient as a function of time between the fraction of the growth chamber occupied by the partner strain and the growth rate for individual cells (inset). The × symbol denotes correlations corresponding to $P > 0.05$.

To further study the inverse relationship between the growth rate of $\Delta metA$ and the strength of its outgoing positive interaction on $\Delta pheA$, we measured M and F in each producer strain's supernatant across different concentrations of the rescuing amino acids (see **Methods**). The F concentration per unit biomass in the $\Delta metA$ supernatant was inversely proportional to the supplemented M concentration and thus its growth rate, consistent with the significant growth enhancement of $\Delta pheA$ when $\Delta metA$ was slowly growing and metabolically active, but not when it was rescued (**Figure 6.8b**). Notably, the reverse trend was observed for $\Delta pheA$, wherein M was detected only in the highest supplemented F condition. In sum, the differential release profiles of M and F as a function of each producer strain's growth rate provides insight into the topologies of the inferred interaction networks (**Figure 6.10**).

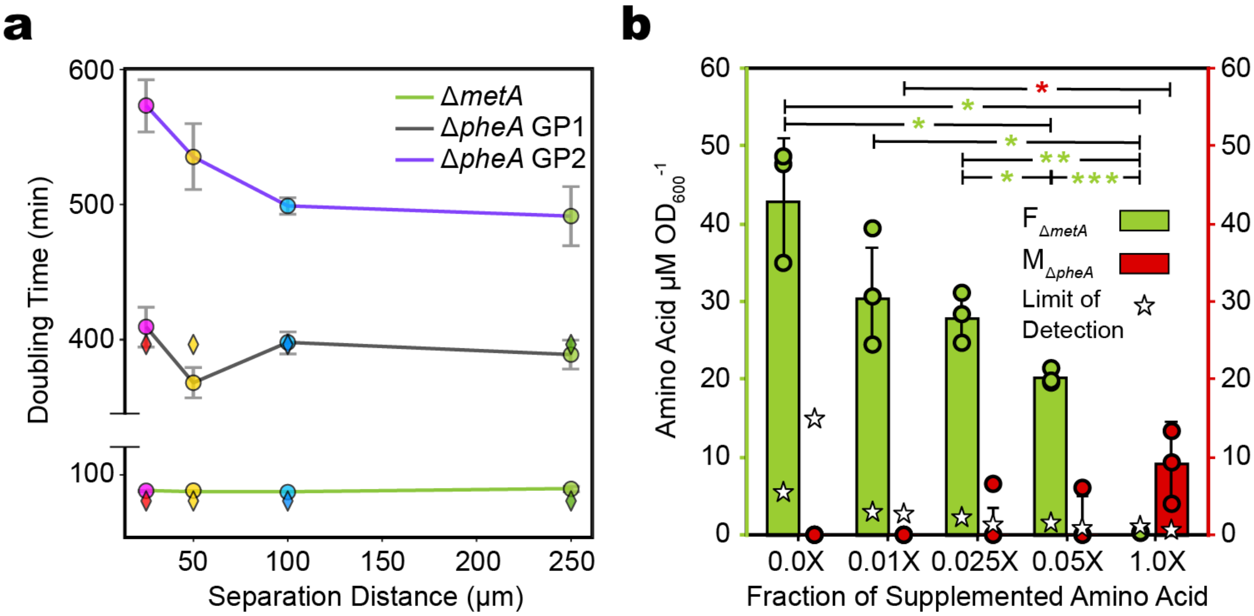

Figure 6.8: Impacts of auxotroph rescue on amino acid secretion and growth of partner strain. **(a)** Relationship between spatial separation and the minimum doubling time in the presence of M and absence of F. Δ*pheA* exhibited two growth phases following the media switch (GP1 and GP2). Diamonds indicate model fits to the maximum growth rates in GP1. **(b)** Concentration of M or F divided by absorbance at 600 nm (OD600) in Δ*pheA* or Δ*metA* conditioned media. Stars indicate the limit of detection for each measurement. 1X amino acid fraction refers to 0.2 mM M and 0.4 mM F, respectively. The horizontal lines denote a statistically significant difference ($P < 0.05$) based on a two-sided t-test. $*P < 0.05, **P < 0.01$, and $***P < 0.001$ (see **Appendix A**).

6.4 Modeling an auxotrophic community cross-feeding across distance.

Our results demonstrated that Δ*metA* and Δ*pheA* auxotroph strains have differential and context-dependent release rates of M and F, highlighting the environmental sensitivity of the system. To integrate our findings into a quantitative framework, we developed a computational model to represent M and F biosynthesis, uptake, diffusion, and amino acid dependent growth rates of Δ*metA* and Δ*pheA*. Consistent with our data, we assume that (1) growth is limited by the concentration of the amino acid that the auxotroph is deficient in producing, (2) release of F by Δ*metA* is inversely proportional to its growth rate, (3) release of M by Δ*pheA* is proportional to its growth rate, and (4) the basal growth rate of Δ*pheA* is larger than that of Δ*metA*, which is attributed to differences in the metabolic consequences of each mutation (**Figure 6.7a**). Similar to the quorum sensing model, we assume that diffusion is modeled as a one-dimensional process by

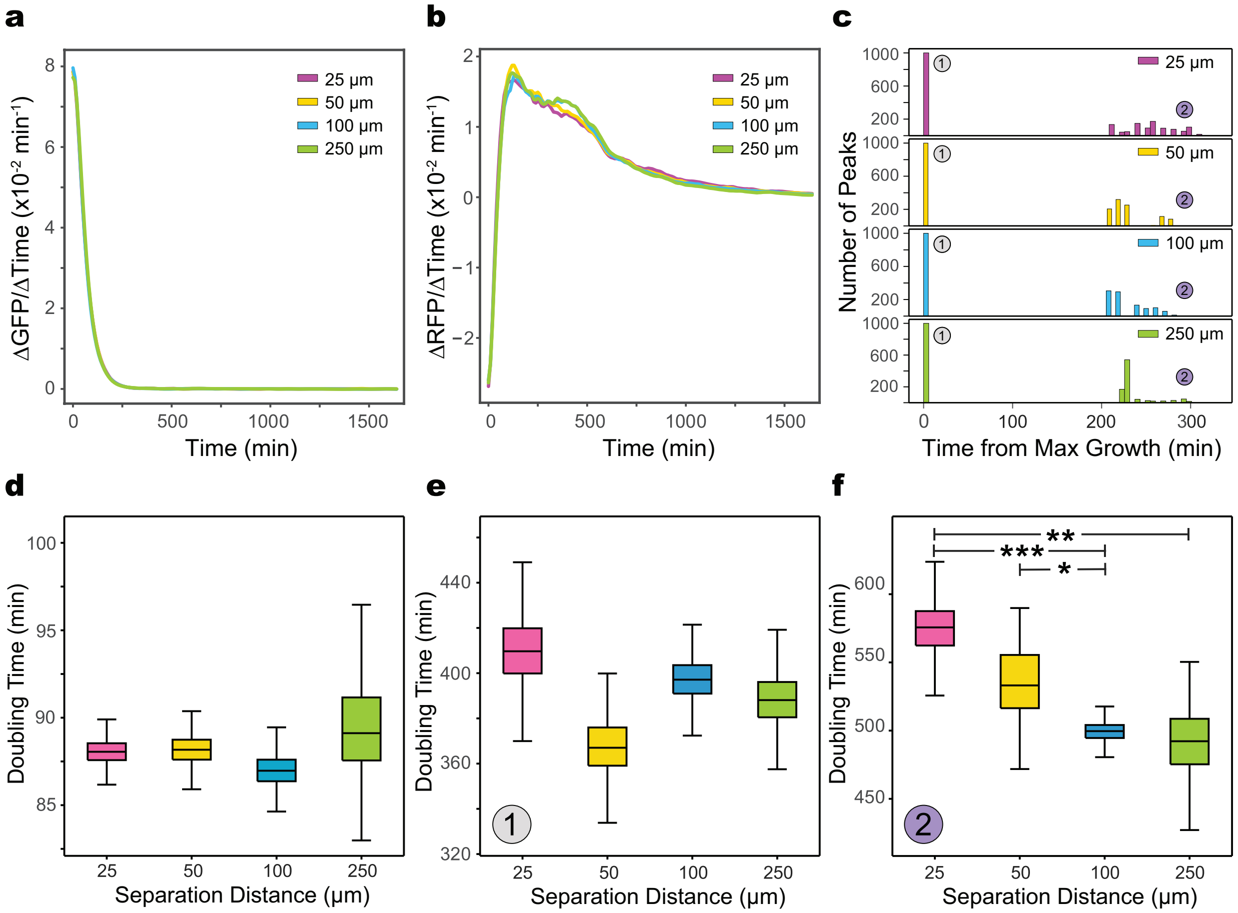

Figure 6.9: Growth rate characterization of amino acid auxotrophs in +M -F conditions. (a) Rate of change in GFP fluorescence of $\Delta metA$ as a function of time. Solid lines represent the mean and shaded regions represent one standard deviation from the mean. **(b)** Rate of change of RFP fluorescence of $\Delta pheA$ over time. **(c)** Histogram of the number of peaks identified in the rate of change of RFP fluorescence over time for 1000 bootstrapped curves using a peak finding algorithm (see **Methods**). The distributions were normalized to the time of maximum growth rate. **(d)** Box plot of cell doubling times for the $\Delta metA$ strain at different distances from the $\Delta pheA$ strain. Horizontal lines within boxes depict the median, and upper and lower edges represent upper and lower quartiles, respectively. Upper and lower whiskers represent the 95th and 5th confidence intervals, respectively. Differences between the distributions represented in the box plot were not statistically significant based on one-tailed bootstrap hypothesis testing. **(e)** Box plot of cell doubling times for first growth phase corresponding to the maximum growth rate of the $\Delta pheA$ strain. Differences between the distributions represented in the box plot were not statistically significant based on one-tailed bootstrap hypothesis testing. **(f)** Box plot of cell doubling times for the second growth phase of the $\Delta pheA$ strain. The horizontal bars denote a statistical significant difference ($P < 0.05$) based on one-tailed bootstrap hypothesis testing. $*P < 0.05, **P < 0.01$, and $***P < 0.001$ (see **Appendix A**).

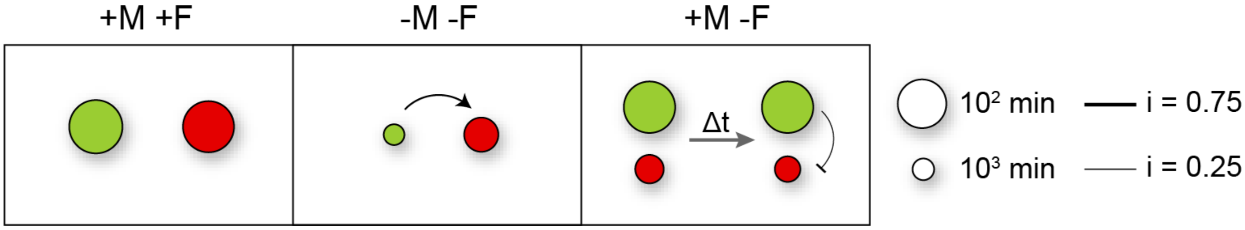

Figure 6.10: Inferred interaction networks of a Δ*metA*-Δ*pheA* in the MISTiC microenvironment. Network topology is based on population-level maximum growth rates of $\Delta metA$ (green) and $\Delta pheA$ (red). The size of the node represents the maximum growth rate in the 25 μm (D_{25}) condition and is computed as $(10 \cdot lnD_{25}^{-1})^2$. The edge widths represent the interaction strength defined as $D_d = 1 - D_{25} \cdot D_{250}^{-1}$ where D_{250} denotes the maximum growth rate in the 250 μm condition.

discretizing space in the interaction channels into 1 μm regions. The diffusion coefficients of methionine (M) and phenylalanine (F) were set to the values of the inferred diffusion coefficients in the quorum sensing model since these small molecules have similar molecular weights ($149 - 213\ g\ mol^{-1}$). Model species are listed in **Table 6.1**, and parameter definitions and values are given in **Table 6.2**.

Species	**Description**
$[M]_{\Delta metA}$	Intracellular [M] in $\Delta metA$
$[F]_{\Delta pheA}$	Intracellular [F] in $\Delta pheA$
$x_{1,\ldots,L}, [M]_{ext}$	Extracellular [M] in different regions of the interaction channel or growth chambers
$y_{1,\ldots,L}, [F]_{ext}$	Extracellular [F] in different regions of the interaction channel or growth chambers

Table 6.1: Species descriptions for auxotroph model.

Intracellular transport of amino acids from the extracellular environment We compute the intracellular concentrations of M and F based on the extracellular concentration using a previous method [147]. The intracellular concentration of M in the $\Delta metA$ strain is given by

$$[M]_{\Delta metA} = U_M \frac{[M]_{ext}}{\kappa_M + [M]_{ext}} + [M]_{ext}, \tag{6.1}$$

where

$$U_M = \frac{V_{max,M} P_{tot}}{D_c} \quad \text{and} \quad \kappa_M = \frac{V_{max,M}}{k_M}. \tag{6.2}$$

Here, $[M]_{ext}$ is the concentration of extracellular methionine, D_c is the diffusion coefficient of amino acid across the outer membrane, $V_{max,M}$ is the uptake rate of M, P_{tot} is the concentration of membrane transporters, and k_M is the binding affinity of M to the transporter. Similarly, the concentration of F in the $\Delta pheA$ strain is

$$[F]_{\Delta pheA} = U_F \frac{[F]_{ext}}{\kappa_F + [F]_{ext}} + [F]_{ext}, \tag{6.3}$$

where

$$U_F = \frac{V_{max,F} P_{tot}}{D_c} \quad \text{and} \quad \kappa_F = \frac{V_{max,F}}{k_F}. \tag{6.4}$$

Here, $[F]_{ext}$ denotes the extracellular F concentration, $V_{max,F}$ is the uptake rate of M, and k_F is the binding affinity of F to its transporter. We assume that D_c and P_{tot} are equivalent for both strains. The kinetic parameters $V_{max,M}$, $V_{max,F}$, κ_M, and κ_F were derived from previous studies that characterized amino acid transport in *E. coli* (**Table 6.2**) [148].

Amino acid limited growth rates of auxotroph strains We assume that growth of each strain is limited by the concentration of the amino acid that this strain is deficient to produce. Therefore, the instantaneous normalized growth rate of each strain is a function of the intracellular concentration of the amino acid. We assume a different non-zero basal growth rate for $\Delta metA$ and $\Delta pheA$ in the absence of the rescuing amino acid denoted by r_M and r_F, respectively. The normalized growth rates for $\Delta metA$ and $\Delta pheA$ are given by the equations

$$GR_{\Delta metA} = (1 - r_M) \frac{[M]^{b_M}_{\Delta metA}}{M^{b_M}_{EC50} + [M]^{b_M}_{\Delta metA}} + r_M, \tag{6.5}$$

$$GR_{\Delta pheA} = (1 - r_F) \frac{[F]^{b_F}_{\Delta metA}}{F^{b_F}_{EC50} + [F]^{b_F}_{\Delta pheA}} + r_F. \tag{6.6}$$

The parameters M_{EC50} and F_{EC50} represent the concentrations of M and F required by $\Delta metA$ and $\Delta pheA$, respectively, to achieve a half-maximal growth rate. The parameters b_M and b_F are Hill coefficients that map the concentration of the amino acid to the growth rate of each strain.

Production and diffusion of amino acids We model the production and diffusion of the amino acids M and F between growth chambers. The $\Delta pheA$ and $\Delta metA$ strains are located in the left and right growth chambers and produce M and F that diffuse through the interaction channel to the opposite end of the channel. The strains $\Delta pheA$ or $\Delta metA$ release and consume M or F. We assume that the amino acid consumption rate cannot be larger than its production rate. The maximum net production of M and F is represented by $\alpha_{net,M}$ and $\alpha_{net,F}$ and is defined as the maximum difference between the production rate minus the consumption rate of each amino acid. We model the net production, degradation, and diffusion of M and F. Let $x_i = [M]$ for $i = 1, ..., L$ denote the concentration of M in the i^{th} unit of the channel.

$$\dot{x}_1 = D_1(x_2 - x_1) - D_2 x_1 - \gamma_M x_1 + \alpha_M \frac{(GR_{\Delta pheA}/U_F)^{c_M}}{(GR_{\Delta pheA}/U_F)^{c_M} + 1}\,, \tag{6.7}$$

$$\dot{x}_i = D_1(x_{i-1} + x_{i+1} - 2x_i) - \gamma_M x_i \text{ for } i = 2, 3, \ldots, L-1\,, \tag{6.8}$$

$$\dot{x}_L = D_1(x_{L-1} - x_L) - D_2 x_L - \gamma_M x_L\,. \tag{6.9}$$

Similarly, let $y_i = [F]$ for $i = 1, ..., L$ denote the concentration of F in the i^{th} unit of the channel.

$$\dot{y}_1 = D(y_2 - y_1) - D_2 y_1 - \gamma_F y_1\,, \tag{6.10}$$

$$\dot{y}_k = D(y_{i-1} + y_{i+1} - 2y_i) - \gamma_F y_i \text{ for } i = 2, 3, \ldots, L-1\,, \tag{6.11}$$

$$\dot{y}_L = D(y_{L-1} - y_L) - D_2 y_L - \gamma_F y_L + \alpha_F \frac{1}{((GR_{\Delta metA}/U_M)^{c_F} + 1)}\,. \tag{6.12}$$

Note that $[M]_{ext} = x_L$ and $[F]_{ext} = y_1$. The parameters γ_M and γ_F denote degradation rates of M and F, α_M and α_F are maximum production rates of the amino acids, and c_M and c_F are Hill coefficients for amino acid production. Consistent with our metabolite measurements, the net production of M is proportional to the growth rate of $\Delta pheA$, whereas the net production of F is inversely proportional to the growth rate of $\Delta metA$.

The model was fit to the population-level growth rates in the physically separated experiments using a genetic algorithm (see **Methods**) and was able to recapitulate the trends across a range of conditions (**Figure 6.2b,c** and **Figure 6.8a**), demonstrating that the model's core assumptions were congruous with the data.

In sum, the stability of the amino-acid auxotroph consortium was shaped by key variables including spatial arrangements, population size, amino acid availability, and growth rate-dependent amino acid release rates. The variation in each strain's growth across defined distances indicates whether metabolites mediating microbial interactions are in a saturated (e.g., below a concentration threshold to impact growth or not limiting for growth) or linear regime (e.g., limiting to growth). In addition, MISTiC enabled characterization of dynamic features of growth responses including biphasic growth (**Figure 6.9b,c**) and delays in the timing of maximum growth (**Figure 6.2c,** inset).

6.5 Methods

Auxotroph community batch culture experiment. Separate culture tubes containing LB with chloramphenicol (25 μg/mL) were inoculated with $\Delta metA$ or $\Delta pheA$ and incubated overnight at 37 °C with shaking. After 16 h, the cultures were diluted into 5 mL of EZ Rich Medium (Teknova) containing chloramphenicol (25 μg/mL) and 1 mM IPTG and lacking M and F at a final OD600 of 0.05. The initial ratio of

Parameter	Description	Value
α_M	Maximum production of M by $\Delta pheA$	0.045 mM min^{-1}
α_F	Maximum production of F by $\Delta metA$	0.55 mM min^{-1}
c_M	Hill coefficient of M production	1.35
c_F	Hill coefficient of F production	1.63
U_M	Maximum uptake rate of M by $\Delta metA$	0.022 min^{-1}
U_F	Maximum uptake rate of F by $\Delta pheA$	4.79 min^{-1}
M_{EC50}	[M] that enables half-maximum growth of $\Delta metA$	0.35 mM
F_{EC50}	[F] that enables half-maximum growth of $\Delta pheA$	0.12 mM
r_M	Basal growth rate of $\Delta metA$ in absence of M	0.073 min^{-1}
r_F	Basal growth rate of $\Delta pheA$ in absence of F	0.21 min^{-1}
γ_M	Degradation rate of methionine	0.073 min^{-1}
γ_F	Degradation rate of phenylalanine	0.044 min^{-1}
b_M	Hill coefficient of $\Delta metA$ growth	1.81
b_F	Hill coefficient of $\Delta pheA$ growth	4.06
D_1^*	Diffusion coefficient through interaction channel	7677.8 μm min^{-1}
D_2^*	Diffusion coefficient from growth chambers to main channels	251.0 μm min^{-1}
$V_{max,M}^+$	Maximum uptake rate of M	0.39
$V_{max,F}^+$	Maximum uptake rate of F	0.75
κ_M^+	Ratio of uptake rate to transporter binding affinity of M	0.0023 mM
κ_F^+	Ratio of uptake rate to transporter binding affinity of F	0.00072 mM
P_{tot}/D_c	Diffusion coefficient of amino acid across cell membranes	1

Table 6.2: Parameter values for auxotroph model. The symbols * and + indicates parameters from the quorum sensing model or previous literature [148], respectively.

$\Delta metA$ to $\Delta pheA$ was 10:1, 1:1, or 1:10 (n=3, for each starting ratio). The cultures were incubated at 37 °C with shaking for at least 24 h before transferring the community to fresh media using a 1:100 dilution. At this transfer time, the OD600 of each culture was measured and a 2 μL sample was spotted onto a glass slide for cell counting with microscopy (20 × magnification) on a Nikon Eclipse Ti. Four images comprising four distinct fields of view were taken of each sample and each image was a composition of phase contrast, GFP and RFP channels. Subsequently, ImageJ was used to extract the number of $\Delta metA$ cells from the GFP channel and $\Delta pheA$ cells from the RFP channel for each image.

Device fabrication. Microfluidic devices for Experiments 6-14 were fabricated according to the methods elaborated in **Chapter 2**. Prior to each experiment, the devices were flushed with 0.5% Tween 20 (Sigma-Aldrich) to prevent cells from adhering to the device.

Auxotroph cell culturing. *E. coli* strains $\Delta metA$ [149] and $\Delta pheA$ [149] were transformed with plasmids A6c_GFP [150] and A6c_RFP [150], respectively, using a standard chemical transformation protocol (see **Appendix B**). The plasmids harbored an IPTG-inducible fluorescent reporter. An initial set of cultures were inoculated into LB media (Lennox, Sigma-Aldrich) containing 25 μg/mL chloramphenicol (Sigma-Aldrich) and incubated overnight at 37 °C with shaking. After approximately 16 h, 1 μL of the overnight cultures were diluted into 3 mL of LB containing 25 μg/mL chloramphenicol and 1 mM IPTG (Sigma-Aldrich) and incubated at 37 °C with shaking until early stationary phase (OD600 0.7–1.1).

MISTiC setup for auxotroph experiments. The cells were loaded into the device following the MISTiC setup procedure outlined in **Chapter 3**. Following cell loading, the microfluidic chip was placed in the custom-designed temperature incubation chamber at 37 °C. The media always contained 1 × MOPS Buffer (Teknova), 1 × ACGU mix (Teknova), chloramphenicol, 0.1% Tween 20, 1.32 mM potassium phosphate dibasic (Teknova), and 0.2% glucose (Teknova), whereas the amino acid composition varied across experiments (see **Appendix A**). The amino acid solutions consisted of either EZ Amino Acids (AA, Teknova) or a modified amino acid solution (AA*). The AA* solution consisted of 0.4 mM L-asparagine (VWR), 0.01 mM calcium pantothenate (VWR), 0.2 mM L-histidine (VWR), 10 mM L-serine (VWR), 0.8 mM L-alanine (Fisher Scientific), 0.4 mM L-lysine (Fisher Scientific), 0.1 mM L-tryptophan (Fisher Scientific), 0.4 mM L-aspartic acid (Dot Scientific), 0.1 mM L-cysteine (Dot Scientific), 0.8 mM L-glycine (Dot Scientific), 0.4 mM L-isoleucine (Dot Scientific), 0.8 mM L-leucine (Dot Scientific), 0.01 mM para-amino benzoic acid (Dot Scientific), 0.4 mM L-proline (Dot Scientific), 0.4 mM L-threonine (Dot Scientific), 0.6 mM L-valine (Dot Scientific), 5.2 mM L-arginine (Sigma), 0.01 mM di-hydroxy benzoic acid (Sigma), 0.6 mM L-glutamic acid (Sigma), 0.01 mM para-hydroxy benzoic acid (Sigma), 0.01 mM thiamine (Sigma), 0.2 mM L-tyrosine (Sigma), and 0.6 mM L-glutamine (Acros Organics). In minimal media supplemented with AA*, varying concentrations of methionine (Dot Scientific) and/or phenylalanine (Dot Scientific) were added. The AA amino acid solution consisted of all components in AA* plus 0.2 mM methionine and 0.4 mM phenylalanine. Cells were grown for a period of time at 37 °C with 1 mM IPTG prior to the media switch (as described in **Appendix A**) to fill the growth chambers. Phase-contrast and fluorescence images were collected every 10 min at 21 different positions. After the growth chambers were filled with cells, the inlets (I_{12} and I_{21}) containing the pre-culture media were set to 0 μL/h and the inlets (I_{11} and I_{22}) containing the test media were set to 200 μL/h.

Population-level image analysis. For Experiments 6, 7, and 11–14, individual growth chambers were segmented in DeepCell [118] using the methods elaborated in **Chapter 3**. The methods for computing the average fluorescence intensity for each growth chamber and excluding outliers were also identical to those described in **Chapter 3**. Fluorescent time-series measurements for each growth chamber in Experiments 6, 7, and 11–14 were analyzed by bootstrapping (see statistical analysis section in **Chapter 3**). Using this method, the biological replicate curves for a given interaction channel length were randomly sampled 10,000 times with replacement. In the spatially separated auxotroph experiments (Experiments 6, 7, 11–14), the fluorescence background for each reporter was subtracted from the data and then the time-series was normalized by dividing by the maximum value. The change in fluorescence per unit time ($\Delta F\ \Delta t^{-1}$) was computed by determining the slope of a line fit to a 10 time point moving window and then multiplying by -1. The global maximum of $\Delta F\ \Delta t^{-1}$ corresponded to the maximum growth rate. The doubling time was calculated using times the following equation:

$$\text{doubling time} = \frac{ln(2)}{max(\Delta F \Delta t^{-1})}\,. \tag{6.13}$$

In Experiment 11, the $\Delta F\ \Delta t^{-1}$ curves displayed a biphasic trend. To characterize the growth rate at each peak, the $\Delta F\ \Delta t^{-1}$ time-series was analyzed between the time point of the media switch and the time point corresponding to 25% of the maximum fluorescence. The local maxima within this time window were identified using the findpeaks algorithm (Python). The bootstrapped $\Delta F\ \Delta t^{-1}$ time-series were aligned by the first peak and the doubling times at the global maximum were calculated as described above. For the second growth phase, the doubling time was calculated at the maximum $\Delta F\ \Delta t^{-1}$ for the period of time between the global maximum and the time point corresponding to 25% of the maximum fluorescence.

Single-cell image analysis. Single-cell metrics were obtained with a custom machine learning approach implemented in Python with the Keras API running on top of TensorFlow [151]. We used two convolutional neural networks with U-Net architecture. First, we performed segmentation of individual cells in each image and then tracked each of the segmented cell instances over time. The segmentation network takes as an input the phase contrast images of cells grown in MISTiC and, for each image, yields a binary mask segmenting the cells from the background. Training data were obtained from a separate experiment imaging fluorescently labeled *E. coli* at 60 × magnification with phase-contrast and fluorescence images collected every 10 min. We used the fluorescence images to generate binary segmentation masks of the cells, which then served as the ground truth for the phase contrast images used for network training. A total of 1066 images were curated this way. The network was trained for 100 epochs using a stochastic gradient descent optimizer and a pixelwise weighted loss function to enforce the learning of narrow borders between adjacent cells. To minimize overfitting of the network to the training data, random affine transformations and elastic deformations were applied in real-time during the training process.

Cell tracking was performed with a separate U-Net similar to a method reported previously [**?**]. The input for this network is a set of consecutive binary segmentation masks. For each cell in the current segmentation, the network predicts the cell in the previous segmentation image from which the current cell was derived. This backwards tracking approach eliminates the need for the network to learn occurrences of cells leaving the chamber and reduces the number of classes to two (the tracked cell and the background). Using segmentations from the mixed auxotroph experiment, we curated 2656 sets of training images with a custom script in MATLAB. Training occurred for 200 epochs using an Adam optimizer and a class-weighted categorical cross-entropy loss function. Similarly, data augmentation was performed to reduce overfitting of the data.

Following segmentation and tracking, the raw output was processed with custom code in Python to reconstruct cell lineage and obtain single-cell metrics. The instantaneous growth rate of each cell was computed from the cross-sectional area recorded during the 100 min window (10 data points) immediately following that instant. Growth rate was computed by fitting a line to each 100 min window and then dividing the slope of the line by the average cell area during that time interval. For all analyses, a minimum tracking duration of 100 min was imposed to enforce consistent computation of growth rate. For all analyses involving growth rate, statistical outliers were identified using a modified z-score computed on the chamber averaged growth rates at each time point,

$$M_i = \frac{0.6745(x_i - \tilde{x})}{M_d}\,. \tag{6.14}$$

where $\tilde{x}$ represents the median growth rate and M_d denotes the median absolute deviation [152]. Statistical outliers were detected using a threshold of $M_i > 3.5$. Growth chambers with more than one time point registering as an outlier were excluded from the analysis (see **Appendix A**). Experimental outliers occurred primarily due to segmentation and tracking errors caused by loss of focus or empty chambers at specific positions. Outliers were considered separately for each strain.

Amino-acid secretion measurements. The $\Delta metA$ and $\Delta pheA$ strains were inoculated into LB (Lennox) containing chloramphenicol (25 μg/mL) and grown overnight at 37 °C with shaking. After 16 h, 10 μL of the cultures were transferred into 3 mL of fresh LB containing chloramphenicol (25 μg/mL) and incubated at 37 °C with shaking until early stationary phase (OD600 0.7–1.1). Immediately following, the cultures were centrifuged at 3500 × g for 5 min, the supernatant was removed, and the cells were inoculated into MOPS EZ Rich Defined Medium lacking M and F at an initial OD600 of 0.05. For the $\Delta metA$ strain, 0, 2, 5, 10, or 200 μM M was added to the media. For $\Delta pheA$ strain, 0, 4, 10, 20, or 400 μM F was added to the media. The cultures were incubated at 37 °C with shaking for 3 h. After recording the OD600 of each culture, the cells were centrifuged at 3500 × g for 10 min, the supernatant was filtered by a 0.2 μm filter (GE Healthcare) and the concentrations of M or F were measured with a fluorometric assay kit (BioVision) or by liquid chromatography-mass spectrometry (LC-MS), respectively. Concentrations of M in the filtered conditioned media of Δ*pheA* cultures were measured with a fluorometric methionine assay kit (BioVision) with a 0.5 μM limit of detection. Raw fluorescence measurements were converted to methionine concentrations using a standard curve.

The analysis of F concentrations in the filtered conditioned media of Δ*metA* was performed on a Shimadzu LC-MS2020. All solvents and reagents used for analysis were HPLC grade or higher quality. Methanol and formic acid were sourced from Fisher Scientific and Acros Organics, respectively. Water was prepared in house with a Millipore Milli-Q water purification system. Separations were performed at 40 °C on a Discovery BIO wide pore C5-5 column (15 cm × 2.1 mm × 5 μm) from Millipore-Sigma with a paired Supelguard (2 cm × 4 mm × 5 μm) guard column. The running buffer was a binary gradient of water with 0.1% v/v formic acid (Buffer A) and methanol (Buffer B) according to the following protocol: 4 min at 5% B, a linear gradient from 5% to 20% for 4 min, a linear gradient from 20% B to 95% B for 2 min, 2 min at 95% B, a linear gradient from 95% B to 5% B for 2 min, equilibration at 5% B for 6 min. The total flow rate was 0.2 mL min^{-1}. Under these conditions, methionine and phenylalanine eluted at 3.8 and 5.8 min, respectively. The ion source was operated in electrospray ionization mode with a cone voltage of 4.5 kV, the interface was held at 400 °C, and the desolvation line at 250 °C. The dry nitrogen was supplied to the nebulizer at 1.5 L/min and drying gas at 15 L/min. The mass spectrometer was run in selective ion monitoring mode for monitoring m/z 150 for methionine and m/z 166 for phenylalanine with a scan time of 1 s. Standards were prepared for each run by adding known concentrations of methionine and phenylalanine to fresh media. The standard curve was run before and after the sample batch and each sample was run twice for technical replicates.

Parameter fitting for auxotroph model. The parameters of the amino acid cross-feeding model (**Table 6.2**) were fit using a genetic algorithm. The genetic algorithm can be most efficient with high-order systems and many unknowns. One of the challenges with the genetic algorithm is there is no proof of convergence and the rate of convergence can be slow if the initial guesses on the parameters are far from the minimizing set and the bounds on the parameters are too broad. In order to overcome these challenges, careful consideration was taken to determine the lower and upper bounds for each parameter. Initially, bounds were determined based on biologically relevant and feasible values. In addition, experimental observations were used to infer necessary relationships between parameters. The bounds on the parameters were adjusted accordingly. After this, the genetic algorithm was executed until the error became invariant for a sequence of 10 generations. As the genetic algorithm is not optimal, it is possible to arrive at slightly different values if we were to run the genetic algorithm longer or reinitiate at new random initial conditions. However, the qualitative fits remain fairly close, as do the parameter values. Nevertheless, given experimental error, it is not in our benefit to achieve an optimal fit, since such a fit does not imply better prediction of quantitative values of parameters.

DISCARD THIS PAGE

Appendix A: Index of Experiments

A.1 Experiment conditions.

Experiment	Descriptor	Media switch	Pre-culture condition	Test condition	Outliers
1	Q. S. (step response)	105 min	aTc	aTc + ara	1;1;0;0
2	Q. S. (step response, inverted)	240 min	aTc	aTc + ara	4;0;1;2
3	Q. S. (forced oscillator, 2 h)	140 min	aTc	aTc ± ara	1;1;1;5
4	Q. S. (forced oscillator, 1 h)	184 min	aTc	aTc ± ara	0;0;1;3
5	Distributed gene circuit oscillator)	217 min	N/A	aTc + IPTG	0;0;3;1
15	Q.S., V_3 (forced oscillator, variable)	330 min (1 h) 890 min (2 h)	aTc	aTc ± ara	6;5;4;5

Table A.1: MISTiC experimental conditions for quorum-sensing experiments. Pre-culture conditions refer to the environment within the microfluidic device from the beginning of the experiment to the time of the first media switch. Test culture conditions refer to the media conditions following the first media switch. Quorum-sensing experiments were performed in Luria Broth (LB). Outliers refer to the number of paired growth chambers that were excluded from the analysis out of n = 10 biological replicates for each interaction channel length (25 μm;50 μm;100 μm;250 μm) based on a set of specific criteria (see **Chapter 3, Methods**). For experiments denoted by (†), the numbers represent single outlier growth chambers that were excluded from the analysis out of n = 20 total biological replicates for 25 μm, 50 μm, 100 μm, and 250 μm interaction channels (see **Chapter 6, Methods**).

Expt.	Descriptor	Media switch	Pre-culture condition	Test condition	Outliers
6	Auxotroph (control)	218 min	0.25X AA + IPTG	0.25X AA	0;0;1;2
7	Auxotroph (−F, −M)	420 min	1X AA* + 0.1X F/M + IPTG	1X AA*	3;2;0;1
8	Auxotroph (mixed)	60 min	1X AA* + 0.1X F/M + IPTG	1X AA* + IPTG	5;2;2;1†
9	Auxotroph (Δ*metA* control)	110 min	1X AA* + 0.1X F/M + IPTG	1X AA* + IPTG	1;2;3;8†
10	Auxotroph (Δ*pheA* control)	90 min	1X AA* + 0.1X F/M + IPTG	1X AA* + IPTG	3;2;2;7†
11	Auxotroph (Δ*metA* rescue)	24 min	0.5X AA* + 0.1X M + 0.05X F + IPTG	0.5X AA* + 1X M	0;0;0;1
12	Auxotroph (all AA)	710 min	0.1X AA + IPTG	0.003X AA	1;0;0;0
13	Auxotroph (all AA)	148 min	0.1X AA + IPTG	0.005X AA	1;0;0;3
14	Auxotroph (all AA)	285 min	0.2X AA + IPTG	0.02X AA	1;2;0;0

Table A.2: MISTiC experimental conditions for auxotroph experiments. Pre-culture conditions refer to the environment within the microfluidic device from the beginning of the experiment to the time of the first media switch. Test culture conditions refer to the media conditions following the first media switch. All experiments used MOPS EZ Rich Defined Medium, with the modifications specified above. AA refers to EZ amino acid solutions containing all amino acids and AA* refers to an amino acid solution lacking methionine (M) or phenylalanine (F). In experiments where F and M were added separately, 1X F and 1X M refer to 0.4 mM and 0.2 mM, respectively. The pre-culture amino acid fraction was varied to control cell growth and fluorescent reporter expression. Outliers refer to the number of paired growth chambers that were excluded from the analysis out of n = 10 biological replicates for each interaction channel length (25 μm; 50 μm; 100 μm; 250 μm) based on a set of specific criteria (see **Chapter 3, Methods**). For experiments denoted by (†), the numbers represent single outlier growth chambers that were excluded from the analysis out of n = 20 total biological replicates for 25 μm, 50 μm, 100 μm, and 250 μm interaction channels (see **Chapter 6, Methods**).

A.2 Statistical test data for all experiments.

A.2 Sender-receiver quorum sensing experiments.

Strain	**25 μm**	**50 μm**	**100 μm**	**250 μm**
Sender	0.402259	0.608653	0.222456	0.936418
Receiver	0.456543	0.735272	0.490299	0.010140

Table A.3: *P*-values for Experiments 1-2, Inverted Positions.

Sender	**50 μm**	**100 μm**	**250 μm**
25 μm	0.4142	0.4865	0.4724
50 μm	—	0.4860	0.4960
100 μm	—	—	0.4009

Receiver	**50 μm**	**100 μm**	**250 μm**
25 μm	0.0084	0.0946	0.0386
50 μm	—	0.1281	0.0038
100 μm	—	—	0.3634

Table A.4: *P*-values for Experiment 3, Signal-to-Noise.

Sender	**50 μm**	**100 μm**	**250 μm**
25 μm	0.3011	0.5635	0.6508
50 μm	—	0.2185	0.4167
100 μm	—	—	0.5957

Receiver	**50 μm**	**100 μm**	**250 μm**
25 μm	0.041243	0.000008	0.000063
50 μm	—	0.006158	0.007676
100 μm	—	—	0.111161

Table A.5: *P*-values for Experiment 4, Signal-to-Noise.

A.2 Dual-feedback oscillator experiments.

Activator	50 μm	100 μm	250 μm
25 μm	0.00027	0.000882	0.0003684
50 μm	—	0.2185	0.4167
100 μm	—	—	0.3396577

Repressor	50 μm	100 μm	250 μm
25 μm	0.490548	0.00281	0.006595
50 μm	—	0.01196	0.026273
100 μm	—	—	0.825160

Table A.6: P-values for Experiment 5, Amplitudes.

Activator	50 μm	100 μm	250 μm
25 μm	0.530488	0.082501	0.0121141
50 μm	—	0.074239	0.0180749
100 μm	—	—	0.7831872

Repressor	50 μm	100 μm	250 μm
25 μm	0.482493	0.116482	7.36E-06
50 μm	—	0.221686	1.12E-05
100 μm	—	—	0.003286

Table A.7: P-values for Experiment 5, Number of Peaks.

	50 μm	100 μm	250 μm
25 μm	0.3311	0.0868	0.0002
50 μm	—	0.2526	0.0003
100 μm	—	—	0.0090

Table A.8: P-values for Experiments 5, Maximum Correlation.

	50 μm	100 μm	250 μm
25 μm	0.8930	0.3204	0.0216
50 μm	—	0.1789	0.0149
100 μm	—	—	0.1008

Table A.9: P-values for Experiments 5, Time Lag.

A.2 Auxotroph experiments.

ΔmetA	50 μm	100 μm	250 μm
25 μm	0.968962	0.222213	0.6677918
50 μm	—	0.175572	0.6213711
100 μm	—	—	0.4308596

ΔpheA	50 μm	100 μm	250 μm
25 μm	0.108647	0.801381	0.4505158
50 μm	—	0.191799	0.1860261
100 μm	—	—	0.6497227

Table A.10: *P*-values for Experiment 6, +M +F test condition.

ΔmetA	50 μm	100 μm	250 μm
25 μm	0.070324	0.131259	0.288765
50 μm	—	0.750636	0.413298
100 μm	—	—	0.622076

ΔpheA	50 μm	100 μm	250 μm
25 μm	0.364665	5.57E−06	6.29E−06
50 μm	—	1.05E−05	1.49E−05
100 μm	—	—	0.027184

Table A.11: *P*-values for Experiment 7, −M −F test condition.

ΔpheA	50 μm	100 μm	250 μm
25 μm	0.3355	0.0432	0.0494
50 μm	—	0.0682	0.1185
100 μm	—	—	0.0935

Table A.12: *P*-values for Experiment 7, −M −F time lag in growth.

ΔmetA	50 μm	100 μm	250 μm
25 μm	0.896383	0.424424	0.774661
50 μm	—	0.394931	0.817224
100 μm	—	—	0.535158

Table A.13: *P*-values for Experiment 11, +M −F test condition.

ΔpheA GP1	**50 μm**	**100 μm**	**250 μm**
25 μm	0.489943	0.552320	0.8350058
50 μm	—	0.138334	0.5632902
100 μm	—	—	0.3307124

ΔpheA GP2	**50 μm**	**100 μm**	**250 μm**
25 μm	0.182705	0.000366	0.004516
50 μm	—	0.020797	0.089901
100 μm	—	—	0.624952

Table A.14: *P*-values for Experiment 11, +M −F test condition.

ΔmetA	**50 μm**	**100 μm**	**250 μm**
25 μm	0.037385	0.641391	0.5535304
50 μm	—	0.098395	0.2834969
100 μm	—	—	0.8037953

ΔpheA	**50 μm**	**100 μm**	**250 μm**
25 μm	0.064692	0.000759	0.000389
50 μm	—	0.120851	0.043729
100 μm	—	—	0.287352

Table A.15: *P*-values for Experiment 12, 0.003X AAs test condition.

ΔmetA	**50 μm**	**100 μm**	**250 μm**
25 μm	0.247728	0.754728	0.0822178
50 μm	—	0.505827	0.2253888
100 μm	—	—	0.1477334

ΔpheA	**50 μm**	**100 μm**	**250 μm**
25 μm	0.011602	0.009112	0.496241
50 μm	—	0.673519	0.029181
100 μm	—	—	0.022791

Table A.16: *P*-values for Experiment 13, 0.005X AAs test condition.

ΔmetA	**50 μm**	**100 μm**	**250 μm**
25 μm	0.05376	0.943291	0.6221304
50 μm	—	0.057607	0.1632572
100 μm	—	—	0.6682308

ΔpheA	**50 μm**	**100 μm**	**250 μm**
25 μm	0.58644	0.040782	0.18212
50 μm	—	0.288083	0.691512
100 μm	—	—	0.305052

Table A.17: *P*-values for Experiment 14, 0.02X AAs test condition.

A.2 Sender-V_3 quorum sensing experiments.

Sender	**50 μm**	**100 μm**	**250 μm**
25 μm	0.5778	0.6312	0.6394
50 μm	—	0.4636	0.2987
100 μm	—	—	0.4465

Receiver	**50 μm**	**100 μm**	**250 μm**
25 μm	0.0003	0.0365	0.1195
50 μm	—	0.0001	0.0025
100 μm	—	—	0.0235

Table A.18: P-values for Experiment 15, 1 h Oscillatory Phase, Signal-to-Noise.

Sender	**50 μm**	**100 μm**	**250 μm**
25 μm	0.1304	0.2272	0.4145
50 μm	—	0.2308	0.4172
100 μm	—	—	0.5021

Receiver	**50 μm**	**100 μm**	**250 μm**
25 μm	0.0170	0.0274	0.0118
50 μm	—	0.0401	0.1083
100 μm	—	—	0.0337

Table A.19: P-values for Experiment 15, 2 h Oscillatory Phase, Signal-to-Noise.

A.2 Amino acid secretion assays.

M-ΔpheA	**0.01X**	**0.025X**	**0.05X**	**1.0X**
0X	0.154073	0.162219	0.128987	0.104564
0.01X	—	0.697201	0.234794	0.010176
0.025X	—	—	0.377097	0.153827
0.05X	—	—	—	0.110678

Table A.20: P-values for methionine secretion by $\Delta pheA$.

F-ΔmetA	**0.01X**	**0.025X**	**0.05X**	**1.0X**
0X	0.118566	0.051864	0.031624	0.010126
0.01X	—	0.523527	0.119889	0.018765
0.025X	—	—	0.04259	0.004458
0.05X	—	—	—	0.000813

Table A.21: P-values for phenylalanine secretion by $\Delta metA$.

Appendix B: Strains and Plasmids

Strain Identifier	**Strain Background**	**Plasmid(s)**	**Reference**
Sender	BW27783	A6c_LuxI_GFP* OR A6c_LuxI_CFP*	[116]
Receiver	MG1655z1	E2c_LuxR_RFP*	[117]
Activator	CY027 (*E. coli* $\Delta lacI \Delta araC \Delta sdiA$ Ptrc*-cinR Ptrc*-rhlR) Addgene #72402	pC220 (Addgene #65877), pC239 (Addgene #65953)	[56]
Repressor	CY027 (*E. coli* $\Delta lacI \Delta araC \Delta sdiA$ Ptrc*-cinR Ptrc*-rhlR) Addgene #72402	pC236 (Addgene #65951), pC239 (Addgene #65953)	[56]
Repeater$_{WT}$	MG1655z1	E2c_LuxR_wtLuxI_GFP*	[117]
Repeater$_{V_2}$	MG1655z1	E2c_LuxR_v1LuxI_GFP*	[117]
Repeater$_{V_3}$	MG1655z1	E2c_LuxR_v2LuxI_GFP*	[117]
Repeater$_{V_4}$	MG1655z1	E2c_LuxR_v3LuxI_GFP*	[117]
Repeater$_{V_5}$	MG1655z1	E2c_LuxR_v4LuxI_GFP*	[117]
$\Delta metA$	BW25113	A6c_GFP*	[149]
$\Delta pheA$	BW25113	A6c_RFP*	[149]

Table B.1: Strains and plasmids used in this study. An asterisk (*) indicates plasmids that were constructed for this study. All other constructs were derived from the indicated references.

B.1 Plasmid Maps

Plasmid maps are included here for constructs with substantial modifications from the original reference vector. A general plasmid map, E2c_LuxR_xxLuxI_GFP, is provided for all repeater variants as the constructs differ only by sequence mutations in pLuxI (see **Figure 5.8**). Plasmid maps for all other constructs in **Table B.1** can be found in the listed references or on the Addgene database.

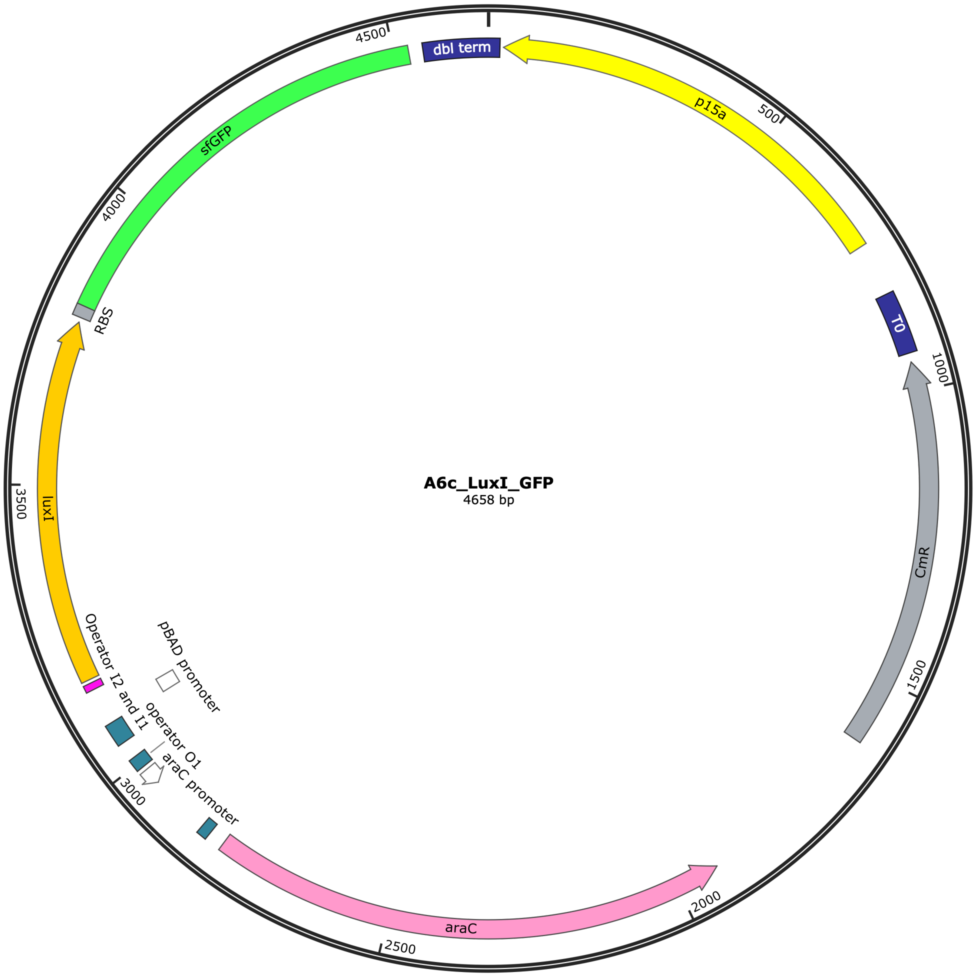

Figure B.1: Plasmid map for A6c_LuxI_GFP.

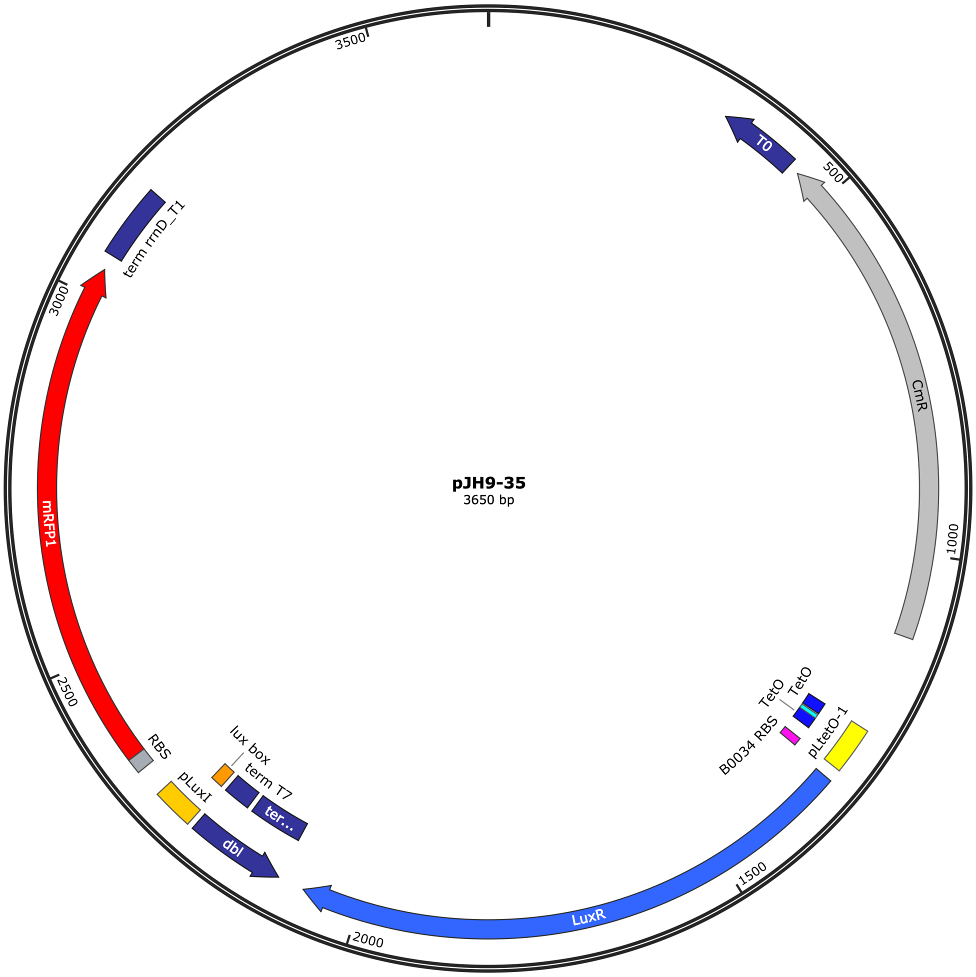

Figure B.2: Plasmid map for E2c_LuxR_RFP.

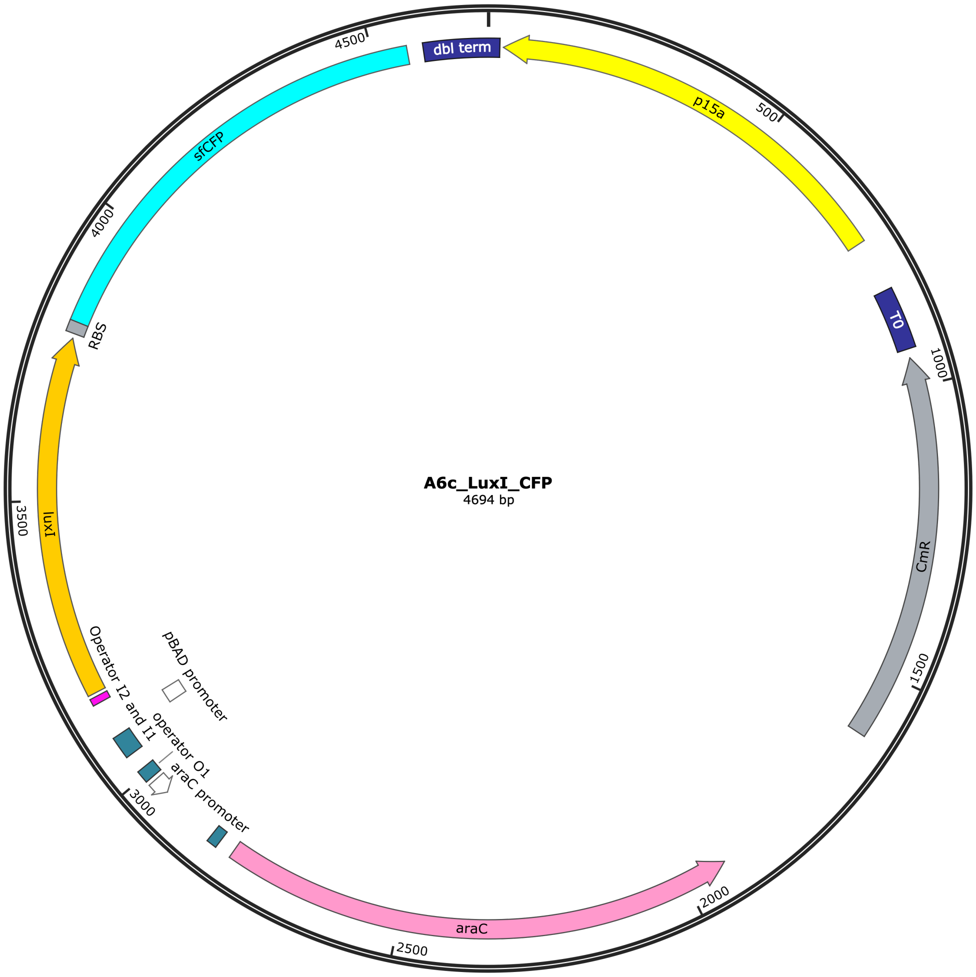

Figure B.3: Plasmid map for A6c_LuxI_CFP.

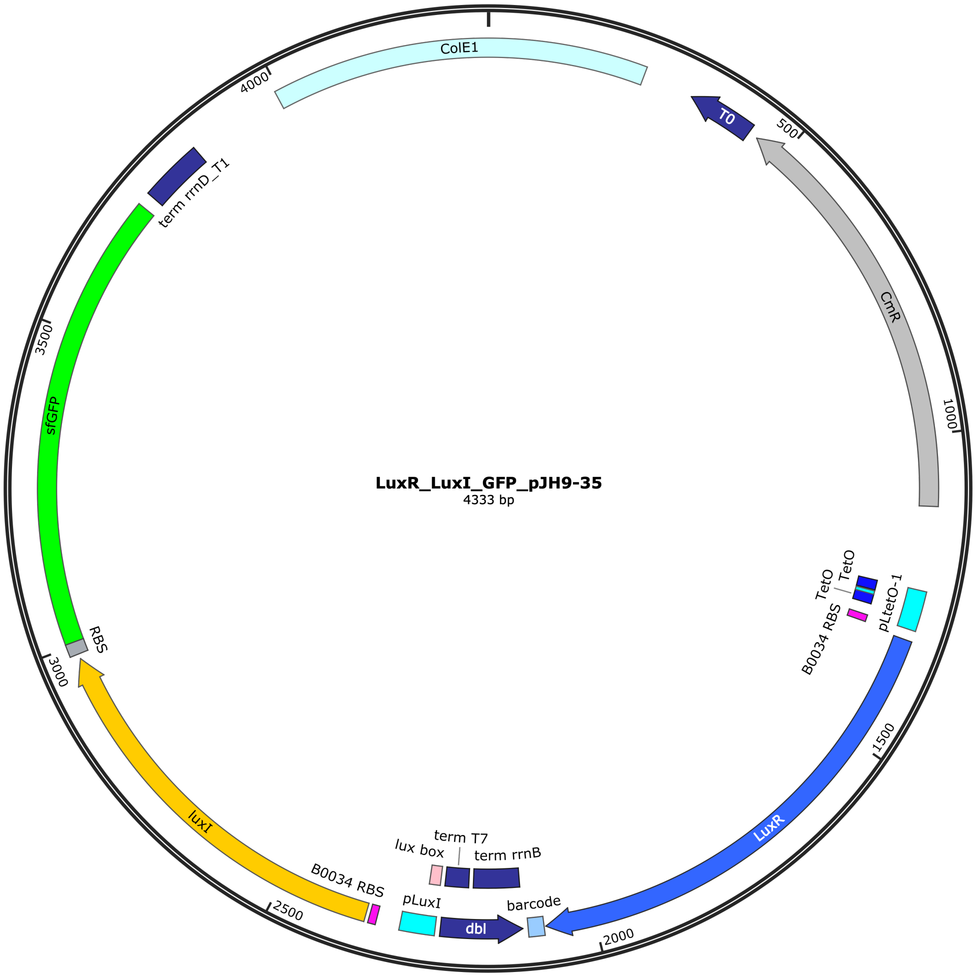

Figure B.4: Plasmid map for E2c_LuxR_xxLuxI_GFP.

LIST OF REFERENCES

[1] Francis Crick. Central dogma of molecular biology. *Nature*, 227(5258):561–563, 1970.

[2] Sarah Franklin and Thomas M. Vondriska. Genomes, proteomes, and the central dogma. *Circulation: Cardiovascular Genetics*, 4(5):576, 2011.

[3] Vân Anh Huynh-Thu and Guido Sanguinetti. Gene regulatory network inference: an introductory survey. In *Methods in Molecular Biology*, volume 1883, pages 1–23. Humana Press Inc., 2019.

[4] Fernando Santos-Beneit. The Pho regulon: a huge regulatory network in bacteria. *Frontiers in Microbiology*, 0(APR):402, 2015.

[5] Jun Yan, Haifang Wang, Yuting Liu, and Chunxuan Shao. Analysis of gene regulatory networks in the mammalian circadian rhythm. *PLOS Computational Biology*, 4(10):e1000193, 2008.

[6] David Karig, K Michael Martini, Ting Lu, Nicholas A DeLateur, Nigel Goldenfeld, and Ron Weiss. Stochastic Turing patterns in a synthetic bacterial population. *Proceedings of the National Academy of Sciences*, 115(26):6572–6577, 2018.

[7] Yangxiaolu Cao, Marc D. Ryser, Stephen Payne, Bochong Li, Christopher V. Rao, and Lingchong You. Collective space-sensing coordinates pattern scaling in engineered bacteria. *Cell*, 165(3):620–630, 2016.

[8] Laurent Potvin-Trottier, Nathan D. Lord, Glenn Vinnicombe, and Johan Paulsson. Synchronous long-term oscillations in a synthetic gene circuit. *Nature*, 538(7626):514–517, 2016.

[9] Yamin Ding, Jianwei Shen, Jianquan Lu, and Jürgen Kurths. Stochastic resonance in genetic regulatory networks under Lévy noise. *EPL (Europhysics Letters)*, 127(5):50003, 2019.

[10] Denise M. Wolf, Lisa Fontaine-Bodin, Ilka Bischofs, Gavin Price, Jay Keasling, and Adam P. Arkin. Memory in microbes: quantifying history-dependent behavior in a bacterium. *PLOS ONE*, 3(2):e1700, 2008.

[11] Timothy S. Gardner, Charles R. Cantor, and James J. Collins. Construction of a genetic toggle switch in Escherichia coli. *Nature*, 403(6767):339–342, 2000.

[12] Joanna Jaruszewicz and Tomasz Lipniacki. Toggle switch: noise determines the winning gene. *Physical biology*, 10(3), 2013.

[13] HH McAdams and L Shapiro. Circuit simulation of genetic networks. *Science*, 269(5224):650–656, 1995.

[14] Abhyudai Singh and Leor S. Weinberger. Stochastic gene expression as a molecular switch for viral latency. *Current Opinion in Microbiology*, 12(4):460–466, 2009.

[15] Douglas H. Erwin and Eric H. Davidson. The evolution of hierarchical gene regulatory networks. *Nature Reviews Genetics 2009 10:2*, 10(2):141–148, 2009.

[16] Eric H. Davidson and Douglas H. Erwin. Gene regulatory networks and the evolution of animal body plans. *Science*, 311(5762):796–800, 2006.

[17] Miri Adler, Pablo Szekely, Avi Mayo, and Uri Alon. Optimal regulatory circuit topologies for fold-change detection. *Cell Systems*, 4(2):171–181.e8, 2017.

[18] Patrick Hillenbrand, Georg Fritz, and Ulrich Gerland. Biological signal processing with a genetic toggle switch. *PLOS ONE*, 8(7):e68345, 2013.

[19] Michael B Elowitz and Stanislas Leibler. A synthetic oscillatory network of transcriptional regulators. *Nature*, 403(6767):335–338, 2000.

[20] Bas Jhm Rosier and Tom Fa De Greef. How to make an oscillator. *eLife*, 4, 2015.

[21] Alexandra Pokhilko, Aurora Piñas Fernández, Kieron D Edwards, Megan M Southern, Karen J Halliday, and Andrew J Millar. The clock gene circuit in Arabidopsis includes a repressilator with additional feedback loops. *Molecular Systems Biology*, 8:574, 2012.

[22] J. Patrick Pett, Anja Korenčič, Felix Wesener, Achim Kramer, and Hanspeter Herzel. Feedback loops of the mammalian circadian clock constitute repressilator. *PLoS Computational Biology*, 12(12), 2016.

[23] Ahmad S. Khalil and James J. Collins. Synthetic biology: applications come of age. *Nature Reviews Genetics*, 11(5):367–379, 2010.

[24] Haoqian Zhang, Min Lin, Handuo Shi, Weiyue Ji, Longwen Huang, Xiaomeng Zhang, Shan Shen, Rencheng Gao, Shuke Wu, Chengzhe Tian, Zhenglin Yang, Guosheng Zhang, Siheng He, Hao Wang, Tiffany Saw, Yiwei Chen, and Qi Ouyang. Programming a pavlovian-like conditioning circuit in Escherichia coli. *Nature Communications*, 5:3102, 2014.

[25] Miles W. Gander, Justin D. Vrana, William E. Voje, James M. Carothers, and Eric Klavins. Digital logic circuits in yeast with CRISPR-dCas9 NOR gates. *Nature Communications*, 8(1):1–11, 2017.

[26] Hyojin Kim, Daniel Bojar, and Martin Fussenegger. A CRISPR/Cas9-based central processing unit to program complex logic computation in human cells. *Proceedings of the National Academy of Sciences*, 116(15):7214–7219, 2019.

[27] Vittorio Bartoli, Grace A. Meaker, Mario di Bernardo, and Thomas E. Gorochowski. Tunable genetic devices through simultaneous control of transcription and translation. *Nature Communications*, 11(1):1–11, 2020.

[28] Xinyi Wan, Francesca Volpetti, Ekaterina Petrova, Chris French, Sebastian J. Maerkl, and Baojun Wang. Cascaded amplifying circuits enable ultrasensitive cellular sensors for toxic metals. *Nature Chemical Biology*, 15(5):540–548, 2019.

[29] Viktor Stein and Kirill Alexandrov. Protease-based synthetic sensing and signal amplification. *Proceedings of the National Academy of Sciences*, 111(45):15934–15939, 2014.

[30] Jerome Bonnet, Peter Yin, Monica E. Ortiz, Pakpoom Subsoontorn, and Drew Endy. Amplifying genetic logic gates. *Science*, 340(6132):599–603, 2013.

[31] Qiang Zhang, Sudin Bhattacharya, and Melvin E. Andersen. Ultrasensitive response motifs: basic amplifiers in molecular signalling networks, 2013.

[32] Arturo Urrios, Javier Macia, Romilde Manzoni, Núria Conde, Adriano Bonforti, Eulàlia de Nadal, Francesc Posas, and Ricard Solé. A synthetic multicellular memory device. *ACS Synthetic Biology*, 5(8):862–873, 2016.

[33] Jesus Fernandez-Rodriguez, Lei Yang, Thomas E. Gorochowski, D. Benjamin Gordon, and Christopher A. Voigt. Memory and combinatorial logic based on DNA inversions: dynamics and evolutionary stability. *ACS Synthetic Biology*, 4(12):1361–1372, 2015.

[34] Tatenda Shopera, William R Henson, Andrew Ng, Young Je Lee, Kenneth Ng, and Tae Seok Moon. Robust, tunable genetic memory from protein sequestration combined with positive feedback. *Nucleic Acids Research*, 43(18):9086–9094, 2015.

[35] Caleb J Bashor, Nikit Patel, Sandeep Choubey, Ali Beyzavi, Jané Kondev, James J Collins, and Ahmad S Khalil. Complex signal processing in synthetic gene circuits using cooperative regulatory assemblies. *Science*, 364(6440):593–597, 2019.

[36] Isaak E. Müller, Jacob R. Rubens, Tomi Jun, Daniel Graham, Ramnik Xavier, and Timothy K. Lu. Gene networks that compensate for crosstalk with crosstalk. *Nature Communications*, 10(1):1–8, 2019.

[37] Brandon Alexander Holt and Gabriel A. Kwong. Protease circuits for processing biological information. *Nature Communications*, 11(1):1–12, 2020.

[38] Ximing Li, Luna Rizik, Valeriia Kravchik, Maria Khoury, Netanel Korin, and Ramez Daniel. Synthetic neural-like computing in microbial consortia for pattern recognition. *Nature Communications*, 12(1):1–12, 2021.

[39] John T Sexton and Jeffrey J Tabor. Multiplexing cell-cell communication. *Molecular Systems Biology*, 16(7), 2020.

[40] Salva Duran-Nebreda, Jordi Pla, Blai Vidiella, Jordi Piñero, Nuria Conde-Pueyo, and Ricard Solé. Synthetic lateral inhibition in periodic pattern forming microbial colonies. *ACS Synthetic Biology*, 10(2):277–285, 2021.

[41] Christian R Boehm, Paul K Grant, and Jim Haseloff. Programmed hierarchical patterning of bacterial populations. *Nature Communications*, 9(1), 2018.

[42] Mika Tei, Melinda Liu Perkins, Justin Hsia, Murat Arcak, and Adam Paul Arkin. Designing spatially distributed gene regulatory networks to elicit contrasting patterns. *ACS Synthetic Biology*, 8(1):119–126, 2019.

[43] Subhayu Basu, Yoram Gerchman, Cynthia H. Collins, Frances H. Arnold, and Ron Weiss. A synthetic multicellular system for programmed pattern formation. *Nature*, 434(7037):1130–1134, 2005.

[44] Xiaojing J. Gao, Lucy S. Chong, Matthew S. Kim, and Michael B. Elowitz. Programmable protein circuits in living cells. *Science*, 361(6408):1252–1258, 2018.

[45] Stephanie K. Aoki, Gabriele Lillacci, Ankit Gupta, Armin Baumschlager, David Schweingruber, and Mustafa Khammash. A universal biomolecular integral feedback controller for robust perfect adaptation. *Nature 2019 570:7762*, 570(7762):533–537, 2019.

[46] Nathaniel Roquet, Ava P. Soleimany, Alyssa C. Ferris, Scott Aaronson, and Timothy K. Lu. Synthetic recombinase-based state machines in living cells. *Science*, 353(6297), 2016.

[47] Charlie Gilbert, Tzu-Chieh Tang, Wolfgang Ott, Brandon A. Dorr, William M. Shaw, George L. Sun, Timothy K. Lu, and Tom Ellis. Living materials with programmable functionalities grown from engineered microbial co-cultures. *Nature Materials*, 20(5):691–700, 2021.

[48] Jessica L. Terrell, Tanya Tschirhart, Justin P. Jahnke, Kristina Stephens, Yi Liu, Hong Dong, Margaret M. Hurley, Maria Pozo, Ryan McKay, Chen Yu Tsao, Hsuan-Chen Wu, Gary Vora, Gregory F. Payne, Dimitra N. Stratis-Cullum, and William E. Bentley. Bioelectronic control of a microbial community using surface-assembled electrogenetic cells to route signals. *Nature Nanotechnology*, 16(6):688–697, 2021.

[49] Luis E. Contreras-Llano, Conary Meyer, Yao Liu, Mridul Sarker, Sierin Lim, Marjorie L. Longo, and Cheemeng Tan. Holistic engineering of cell-free systems through proteome-reprogramming synthetic circuits. *Nature Communications*, 11(1):1–10, 2020.

[50] Henrike Niederholtmeyer, Zachary Z. Sun, Yutaka Hori, Enoch Yeung, Amanda Verpoorte, Richard M. Murray, and Sebastian J. Maerkl. Rapid cell-free forward engineering of novel genetic ring oscillators. *eLife*, 4, 2015.

[51] Alex Joesaar, Shuo Yang, Bas Bögels, Ardjan van der Linden, Pascal Pieters, B. V. V. S. Pavan Kumar, Neil Dalchau, Andrew Phillips, Stephen Mann, and Tom F. A. de Greef. DNA-based communication in populations of synthetic protocells. *Nature Nanotechnology*, 14(4):369–378, 2019.

[52] Valeriu Balaban, Sean Lim, Gaurav Gupta, James Boedicker, and Paul Bogdan. Quantifying emergence and self-organisation of Enterobacter cloacae microbial communities. *Scientific Reports*, 8(1):1–9, 2018.

[53] Corentin Briat, Ankit Gupta, and Mustafa Khammash. Antithetic integral feedback ensures robust perfect adaptation in noisy biomolecular networks. *Cell Systems*, 2(1):15–26, 2016.

[54] Gianfranco Fiore, Antoni Matyjaszkiewicz, Fabio Annunziata, Claire Grierson, Nigel J Savery, Lucia Marucci, and Mario Di Bernardo. In-silico analysis and implementation of a multicellular feedback control strategy in a synthetic bacterial consortium. *ACS Synthetic Biology*, 6(3):507–517, 2017.

[55] Oliver Purcell, Nigel J. Savery, Claire S. Grierson, and Mario di Bernardo. A comparative analysis of synthetic genetic oscillators. *Journal of the Royal Society Interface*, 7(52):1503, 2010.

[56] Ye Chen, Jae Kyoung Kim, Andrew J. Hirning, Krešimir Josić, and Matthew R. Bennett. Emergent genetic oscillations in a synthetic microbial consortium. *Science*, 349(6251):986–989, 2015.

[57] Lea Goentoro, Oren Shoval, Marc W. Kirschner, and Uri Alon. The incoherent feedforward loop can provide fold-change detection in gene regulation. *Molecular Cell*, 36(5):894–899, dec 2009.

[58] Yeqing Zong, Haoqian M. Zhang, Cheng Lyu, Xiangyu Ji, Junran Hou, Xian Guo, Qi Ouyang, and Chunbo Lou. Insulated transcriptional elements enable precise design of genetic circuits. *Nature Communications*, 8(1):1–13, 2017.

[59] Javier Santos-Moreno and Yolanda Schaerli. Using synthetic biology to engineer spatial patterns. *Advanced Biosystems*, 3(4):1800280, 2019.

[60] Maximilian Weitz, Andrea Mückl, Korbinian Kapsner, Ronja Berg, Andrea Meyer, and Friedrich C. Simmel. Communication and computation by bacteria compartmentalized within microemulsion droplets. *Journal of the American Chemical Society*, 136(1):72–75, 2013.

[61] Shi Yu, Shihu Wang, and Ronald G. Larson. Proteins searching for their target on DNA by one-dimensional diffusion: overcoming the "speed-stability" paradox. *Journal of Biological Physics*, 39(3):565, 2013.

[62] Siowling Soh, Marta Byrska, Kristiana Kandere-Grzybowska, and Bartosz A. Grzybowski. Reaction-diffusion systems in intracellular molecular transport and control. *Angewandte Chemie International Edition*, 49(25):4170–4198, 2010.

[63] Reed M. Stubbendieck, Carol Vargas-Bautista, and Paul D. Straight. Bacterial communities: interactions to scale. *Frontiers in Microbiology*, 7:1234, 2016.

[64] Velemir Ninkovic, Dimitrije Markovic, and Merlin Rensing. Plant volatiles as cues and signals in plant communication. *Plant, Cell, and Environment*, 44(4):1030–1043, 2021.

[65] H. L. Penman. Gas and vapour movements in the soil: the diffusion of vapours through porous solids. *The Journal of Agricultural Science*, 30(3):437–462, 1940.

[66] Ákos T. Kovács. Impact of spatial distribution on the development of mutualism in microbes. *Frontiers in Microbiology*, 0(NOV):649, 2014.

[67] Michelle G. J. L. Habets, Daniel E. Rozen, Rolf F. Hoekstra, and J. Arjan G. M. de Visser. The effect of population structure on the adaptive radiation of microbial populations evolving in spatially structured environments. *Ecology Letters*, 9(9):1041–1048, 2006.

[68] Lingjun Li, Tian Wu, Ying Wang, Min Ran, Yu Kang, Qi Ouyang, and Chunxiong Luo. Spatial coordination in a mutually beneficial bacterial community enhances its antibiotic resistance. *Communications Biology*, 2(1):1–13, 2019.

[69] Venhar Celik Ozgen, Wentao Kong, Andrew E. Blanchard, Feng Liu, and Ting Lu. Spatial interference scale as a determinant of microbial range expansion. *Science Advances*, 4(11):eaau0695, 2018.

[70] Sylvie Estrela and Sam P. Brown. Metabolic and demographic feedbacks shape the emergent spatial structure and function of microbial communities. *PLOS Computational Biology*, 9(12):e1003398, 2013.

[71] Carey D. Nadell, Kevin R. Foster, and João B. Xavier. Emergence of spatial structure in cell groups and the evolution of cooperation. *PLOS Computational Biology*, 6(3):e1000716, 2010.

[72] Jessica L. Mark Welch, Yuko Hasegawa, Nathan P. McNulty, Jeffrey I. Gordon, and Gary G. Borisy. Spatial organization of a model 15-member human gut microbiota established in gnotobiotic mice. *Proceedings of the National Academy of Sciences*, 114(43):E9105–E9114, 2017.

[73] Felix J H Hol, Peter Galajda, Rutger G Woolthuis, Cees Dekker, and Juan E Keymer. The idiosyncrasy of spatial structure in bacterial competition. *BMC research notes*, 8:245, 2015.

[74] Arthur Prindle, Phillip Samayoa, Ivan Razinkov, Tal Danino, Lev S. Tsimring, and Jeff Hasty. A sensing array of radically coupled genetic 'biopixels'. *Nature*, 481(7379):39–44, 2012.

[75] Tal Danino, Octavio Mondragón-Palomino, Lev Tsimring, and Jeff Hasty. A synchronized quorum of genetic clocks. *Nature*, 463(7279):326–330, 2010.

[76] Ryan H. Hsu, Ryan L. Clark, Jin Wen Tan, John C. Ahn, Sonali Gupta, Philip A. Romero, and Ophelia S. Venturelli. Microbial Interaction Network Inference in Microfluidic Droplets. *Cell Systems*, 9(3):229–242.e4, 2019.

[77] Jihyang Park, Alissa Kerner, Mark A Burns, Xiaoxia Nina Lin, Alfredo Herrera-Estrella, and Mexico Cinvestav. Microdroplet-Enabled Highly Parallel Co-Cultivation of Microbial Communities. *PLoS ONE*, 6(2), 2011.

[78] Laurent Potvin-Trottier, Scott Luro, and Johan Paulsson. Microfluidics and single-cell microscopy to study stochastic processes in bacteria. *Current Opinion in Microbiology*, 43:186–192, 2018.

[79] Leland B Hyman, Clare R Christopher, and Philip A Romero. Single-cell nucleic acid profiling in droplets (SNAPD) enables high-throughput analysis of heterogeneous cell populations. *Nucleic Acids Research*, 2021.

[80] Sampriti Mukherjee and Bonnie L. Bassler. Bacterial quorum sensing in complex and dynamically changing environments. *Nature Reviews Microbiology*, 17(6):371–382, 2019.

[81] Spencer R. Scott and Jeff Hasty. Quorum sensing communication modules for microbial consortia. *ACS Synthetic Biology*, 5(9):969–977, 2016.

[82] Melissa B. Miller and Bonnie L. Bassler. Quorum sensing in bacteria. *Annual Review of Microbiology*, 55:165–199, 2003.

[83] Sophie E Darch, Stuart A West, Klaus Winzer, and Stephen P Diggle. Density-dependent fitness benefits in quorum-sensing bacterial populations. *Proceedings of the National Academy of Sciences*, 109(21):8259–8263, 2012.

[84] Subhash C. Verma and Tim Miyashiro. Quorum sensing in the squid-vibrio symbiosis. *International Journal of Molecular Sciences*, 14(8):16386–16401, 2013.

[85] Brian K. Hammer and Bonnie L. Bassler. Quorum sensing controls biofilm formation in Vibrio cholerae. *Molecular Microbiology*, 50(1):101–104, 2003.

[86] T. R. De Kievit. Quorum sensing in Pseudomonas aeruginosa biofilms. *Environmental Microbiology*, 11(2):279–288, 2009.

[87] Boyuan Wang and Tom W. Muir. Regulation of virulence in Staphylococcus aureus: molecular mechanisms and remaining puzzles. *Cell Chem Biol.*, 23(2):214–224, 2016.

[88] Thomas C. Rösch and Peter L. Graumann. Induction of plasmid conjugation in Bacillus subtilis is bistable and driven by a direct interaction of a Rap/Phr quorum-sensing system with a master repressor. *Journal of Biological Chemistry*, 290(33):20221–20232, 2015.

[89] Alvin Tamsir, Jeffrey J Tabor, and Christopher A Voigt. Robust multicellular computing using genetically encoded NOR gates and chemical 'wires'. *Nature*, (469):212–215, 2011.

[90] Joseph W Larkin, Xiaoling Zhai, Kaito Kikuchi, Samuel E Redford, Arthur Prindle, Jintao Liu, Sacha Greenfield, Aleksandra M Walczak, Jordi Garcia-Ojalvo, Andrew Mugler, and Gürol M Süel. Signal percolation within a bacterial community. *Cell systems*, 7(2):137–145.e3, 2018.

[91] Julius Adler. Chemotaxis in bacteria. *Science*, 153(3737):708–716, 1966.

[92] Svetlana Surkova, Elena Golubkova, Ludmila Mamon, and Maria Samsonova. Dynamic maternal gradients and morphogenetic networks in Drosophila early embryo. *Biosystems*, 173:207–213, 2018.

[93] Cheemeng Tan, Faisal Reza, and Lingchong You. Noise-limited frequency signal transmission in gene circuits. *Biophysical journal*, 93(11):3753–61, 2007.

[94] Nitzan Rosenfeld, Jonathan W Young, Uri Alon, Peter S Swain, and Michael B Elowitz. Gene regulation at the single-cell level. *Science*, 307(5717):1962–1965, 2005.

[95] Yu Tanouchi, Dennis Tu, Jungsang Kim, and Lingchong You. Noise reduction by diffusional dissipation in a minimal quorum sensing motif. *PLoS Computational Biology*, 4(8):4–11, 2008.

[96] Otto X Cordero and Manoshi S Datta. Microbial interactions and community assembly at microscales. *Current Opinion in Microbiology*, 31:227–234, 2016.

[97] Hyun Jung Kim, James Q Boedicker, Jang Wook Choi, and Rustem F Ismagilov. Defined spatial structure stabilizes a synthetic multispecies bacterial community. *Proceedings of the National Academy of Sciences*, 105(47):18188–18193, 2008.

[98] Jeffrey R Moffitt, B Lee, and Philippe Cluzel. The single-cell chemostat: an agarose-based, microfluidic device for high-throughput, single-cell studies of bacteria and bacterial communities. *Lab on a Chip*, 12:1487–1494, 2012.

[99] Xiaolong Luo, Hsuan-chen Wu, Chen-yu Tsao, Yi Cheng, Jordan Betz, Gregory F Payne, Gary W Rubloff, and William E Bentley. Biofabrication of stratified biofilm mimics for observation and control of bacterial signaling. *Biomaterials*, 33:5136–5143, 2012.

[100] Xiaolong Luo, Chen-yu Tsao, Hsuan-chen Wu, David N Quan, Gregory F Payne, Gary W Rubloff De, and William E Bentley. Distal modulation of bacterial cell-cell signalling in a synthetic ecosystem using partitioned microfluidics. *Lab on a Chip*, 15:1842–1851, 2015.

[101] Ekaterina Osmekhina, Christopher Jonkergouw, Georg Schmidt, Farzin Jahangiri, Ville Jokinen, Sami Franssila, and Markus B Linder. Controlled communication between physically separated bacterial populations in a microfluidic device. *Communications Biology*, 1:1–7, 2018.

[102] Alina Burmeister, Fabienne Hilgers, Annika Langner, Christoph Westerwalbesloh, Yannic Kerkhoff, Niklas Tenhaef, Thomas Drepper, Dietrich Kohlheyer, Eric Von Lieres, Stephan Noack, and Alexander Grünberger. A microfluidic co-cultivation platform to investigate microbial interactions at defined. *Lab on a Chip*, 19:98–110, 2019.

[103] Jack Merrin, Stanislas Leibler, and John S Chuang. Printing multistrain bacterial patterns with a piezoelectric inkjet printer. *PLoS ONE*, 2(7):663, 2007.

[104] T Tolker-Nielsen and S Molin. Spatial organization of microbial biofilm communities. *Microbial Ecology*, 40(2):75–84, 2000.

[105] William W Driscoll and John W Pepper. Theory for the evolution of diffusible external goods. *Evolution*, 64(9):2682–2687, 2010.

[106] Christoph Ratzke and Jeff Gore. Self-organized patchiness facilitates survival in a cooperatively growing Bacillus subtilis population. *Nature Microbiology*, 1(5):16022, 2016.

[107] Carey D. Nadell, Knut Drescher, and Kevin R. Foster. Spatial structure, cooperation and competition in biofilms. *Nature Reviews Microbiology*, 14(9):589–600, 2016.

[108] Felix J. H. Hol, Peter Galajda, Krisztina Nagy, Rutger G. Woolthuis, Cees Dekker, and Juan E. Keymer. Spatial Structure Facilitates Cooperation in a Social Dilemma: Empirical Evidence from a Bacterial Community. *PLoS ONE*, 8(10):e77042, 2013.

[109] Ben Libberton, Malcolm J Horsburgh, and Michael A Brockhurst. The effects of spatial structure, frequency dependence and resistance evolution on the dynamics of toxin-mediated microbial invasions. *Evolutionary Applications*, 8(7):738, 2015.

[110] Steven G. McBride and Michael S. Strickland. Quorum sensing modulates microbial efficiency by regulating bacterial investment in nutrient acquisition enzymes. *Soil Biology and Biochemistry*, 136:107514, 2019.

[111] Kelei Zhao, Linjie Liu, Xiaojie Chen, Ting Huang, Lianming Du, Jiafu Lin, Yang Yuan, Yingshun Zhou, Bisong Yue, Kun Wei, and Yiwen Chu. Behavioral heterogeneity in quorum sensing can stabilize social cooperation in microbial populations. *BMC Biology*, 17(1):20, 2019.

[112] Xinyun Cao, Joshua J Hamilton, and Ophelia S Venturelli. Understanding and Engineering Distributed Biochemical Pathways in Microbial Communities. *Biochemistry*, 58(2):94–107, 2019.

[113] Joao B Xavier, Wook Kim, and Kevin R Foster. A molecular mechanism that stabilizes cooperative secretions in Pseudomonas aeruginosa. *Molecular Microbiology*, 79(1):166–179, 2011.

[114] Jeremy M Yarwood, Esther M Volper, and E Peter Greenberg. Delays in Pseudomonas aeruginosa quorum-controlled gene expression are conditional. *Proceedings of the National Academy of Sciences*, 102(25):9008–9013, 2005.

[115] Weiqian Zeng, Pei Du, Qiuli Lou, Lili Wu, Haoqian M. Zhang, Chunbo Lou, Hongli Wang, and Qi Ouyang. Rational design of an ultrasensitive quorum-sensing switch. *ACS Synthetic Biology*, 6(8):1445–1452, 2017.

[116] A. Khlebnikov, K. A. Datsenko, T. Skaug, B. L. Wanner, and J. D. Keasling. Homogeneous expression of the PBAD promoter in Escherichia coli by constitutive expression of the low-affinity high-capacity araE transporter. *Microbiology*, 147(12):3241–3247, 2001.

[117] Robert Sidney Cox, Michael G Surette, Michael B Elowitz, and Michael B Elowitz. Programming gene expression with combinatorial promoters. *Molecular Systems Biology*, 3:145, 2007.

[118] David A. Van Valen, Takamasa Kudo, Keara M. Lane, Derek N. Macklin, Nicolas T. Quach, Mialy M. DeFelice, Inbal Maayan, Yu Tanouchi, Euan A. Ashley, and Markus W. Covert. Deep learning automates the quantitative analysis of individual cells in live-cell imaging experiments. *PLOS Computational Biology*, 12(11):e1005177, 2016.

[119] Johannes Schindelin, Ignacio Arganda-Carreras, Erwin Frise, Verena Kaynig, Mark Longair, Tobias Pietzsch, Stephan Preibisch, Curtis Rueden, Stephan Saalfeld, Benjamin Schmid, Jean-Yves Tinevez, Daniel James White, Volker Hartenstein, Kevin Eliceiri, Pavel Tomancak, and Albert Cardona. Fiji: an open-source platform for biological-image analysis. *Nature Methods*, 9(7):676–682, 2012.

[120] Uddipan Sarma and Indira Ghosh. Oscillations in MAPK cascade triggered by two distinct designs of coupled positive and negative feedback loops. *BMC Research Notes*, 5:287, 2012.

[121] Bernd Blasius, Lars Rudolf, Guntram Weithoff, Ursula Gaedke, and Gregor F. Fussmann. Long-term cyclic persistence in an experimental predator–prey system. *Nature*, 577(7789):226–230, 2019.

[122] Kai Wei Kelvin Lee, Saravanan Periasamy, Manisha Mukherjee, Chao Xie, Staffan Kjelleberg, and Scott A Rice. Biofilm development and enhanced stress resistance of a model, mixed-species community biofilm. *ISME Journal*, 8(4):894–907, 2014.

[123] Leon O. Murphy, Sallie Smith, Rey Huei Chen, Diane C. Fingar, and John Blenis. Molecular interpretation of ERK signal duration by immediate early gene products. *Nature Cell Biology*, 4(8):556–564, 2002.

[124] Louise Ashall, Caroline A. Horton, David E. Nelson, Pawel Paszek, Claire V. Harper, Kate Sillitoe, Sheila Ryan, David G. Spiller, John F. Unitt, David S. Broomhead, Douglas B. Kell, David A. Rand, Violaine Sée, and Michael R. H. White. Pulsatile stimulation determines timing and specificity of NF-κB-dependent transcription. *Science*, 324(5924):242–246, 2009.

[125] Gabriele Micali, Gerardo Aquino, David M. Richards, and Robert G. Endres. Accurate encoding and decoding by single cells: amplitude versus frequency modulation. *PLOS Computational Biology*, 11(6):e1004222, 2015.

[126] Jeremy E. Purvis and Galit Lahav. Encoding and decoding cellular information through signaling dynamics. *Cell*, 152(5):945–956, 2013.

[127] Matthew R. Bennett, Wyming Lee Pang, Natalie A. Ostroff, Bridget L. Baumgartner, Sujata Nayak, Lev S. Tsimring, and Jeff Hasty. Metabolic gene regulation in a dynamically changing environment. *Nature 2008 454:7208*, 454(7208):1119–1122, 2008.

[128] Ovidiu Lipan and Wing H. Wong. The use of oscillatory signals in the study of genetic networks. *Proceedings of the National Academy of Sciences*, 102(20):7063–7068, 2005.

[129] Ido Golding, Johan Paulsson, Scott M. Zawilski, and Edward C. Cox. Real-time kinetics of gene activity in individual bacteria. *Cell*, 123(6):1025–1036, 2005.

[130] Ertugrul M. Ozbudak, Mukund Thattai, Iren Kurtser, Alan D. Grossman, and Alexander Van Oudenaarden. Regulation of noise in the expression of a single gene. *Nature Genetics*, 31(1):69–73, 2002.

[131] Peter L Irwin, Ly-Huong T Nguyen, George C Paoli, and Chin-Yi Chen. Evidence for a bimodal distribution of Escherichia coli doubling times below a threshold initial cell concentration. *BMC Microbiology 2010 10:1*, 10(1):1–14, 2010.

[132] Marc Weber and Javier Buceta. Noise regulation by quorum sensing in low mRNA copy number systems. *BMC Systems Biology 2011 5:1*, 5(1):1–13, 2011.

[133] Pieter Rein Ten Wolde and Andrew Mugler. Importance of crowding in signaling, genetic, and metabolic networks. *International Review of Cell and Molecular Biology*, 307:419–442, 2014.

[134] Alma Dal Co, Simon van Vliet, Daniel Johannes Kiviet, Susan Schlegel, and Martin Ackermann. Short-range interactions govern the dynamics and functions of microbial communities. *Nature Ecology and Evolution*, 4(3):366–375, 2020.

[135] Paul B. Dieterle, Jiseon Min, Daniel Irimia, and Ariel Amir. Dynamics of diffusive cell signaling relays. *eLife*, 9:1–48, 2020.

[136] Paul K Grant, Neil Dalchau, James R Brown, Fernan Federici, Timothy J Rudge, Boyan Yordanov, Om Patange, Andrew Phillips, and Jim Haseloff. Orthogonal intercellular signaling for programmed spatial behavior. *Molecular Systems Biology*, 12(1):849, 2016.

[137] Daniel St Johnston and Christiane Nüsslein-Volhard. The origin of pattern and polarity in the Drosophila embryo. *Cell*, 68(2):201–219, jan 1992.

[138] Kristi A. Egland and E. P. Greenberg. Quorum sensing in Vibrio fischeri: elements of the luxl promoter. *Molecular Microbiology*, 31(4):1197–1204, 1999.

[139] Adam J. Meyer, Thomas H. Segall-Shapiro, Emerson Glassey, Jing Zhang, and Christopher A. Voigt. Escherichia coli “Marionette” strains with 12 highly optimized small-molecule sensors. *Nature Chemical Biology*, 15(2):196–204, 2019.

[140] Luis Caetano M. Antunes, Rosana B.R. Ferreira, C. Phoebe Lostroh, and E. Peter Greenberg. A mutational analysis defines Vibrio fischeri LuxR binding sites. *Journal of Bacteriology*, 190(13):4392–4397, 2008.

[141] Shao-Heng Bao, Wen-Ying Li, Chang-Jun Liu, Dong-Yi Zhang, and Er Meng. Quorum-sensing based small RNA regulation for dynamic and tuneable gene expression. *Biotechnology Letters 2019 41:10*, 41(10):1147–1154, 2019.

[142] Daniel R. Amor, Raúl Montañez, Salva Duran-Nebreda, and Ricard Solé. Spatial dynamics of synthetic microbial mutualists and their parasites. *PLOS Computational Biology*, 13(8):e1005689, 2017.

[143] Simon Maccracken Stump, Evan Curtis Johnson, and Christopher A. Klausmeier. Local interactions and self-organized spatial patterns stabilize microbial cross-feeding against cheaters. *Journal of The Royal Society Interface*, 15(140), 2018.

[144] Michael T Mee, James J Collins, George M Church, and Harris H Wang. Syntrophic exchange in synthetic microbial communities. *Proceedings of the National Academy of Sciences*, 111(20):E2149–56, 2014.

[145] Johanna Roostalu, Arvi Jõers, Hannes Luidalepp, Niilo Kaldalu, and Tanel Tenson. Cell division in Escherichia coli cultures monitored at single cell resolution. *BMC Microbiology*, 8:1–14, 2008.

[146] Ophelia S Venturelli, Alex Carr, Garth Fisher, Ryan Hsu, Rebecca Lau, Benjamin P. Bowen, Susan Hromada, Trent Northen, and Adam P Arkin. Deciphering microbial interactions in synthetic human gut microbiome communities. *Molecular Systems Biology*, 14:e8157, 2018.

[147] Anisha M Perez, Marcella M Gomez, Prashant Kalvapalle, Erin O’Brien-Gilbert, Matthew R Bennett, and Yousif Shamoo. Using cellular fitness to map the structure and function of a major facilitator superfamily effluxer. *Molecular Systems Biology*, 13(12):964, 2017.

[148] J R Piperno and D L Oxender. Amino acid transport systems in Escherichia coli K12. *Journal of Biological Chemistry*, 243(22):5914–5920, 1968.

[149] Tomoya Baba, Takeshi Ara, Miki Hasegawa, Yuki Takai, Yoshiko Okumura, Miki Baba, Kirill A Datsenko, Masaru Tomita, Barry L Wanner, and Hirotada Mori. Construction of Escherichia coli K-12 in-frame, single-gene knockout mutants: the Keio collection. *Molecular Systems Biology*, 2:2006.0008, 2006.

[150] Taek Lee, Rachel A Krupa, Fuzhong Zhang, Meghdad Hajimorad, William J Holtz, Nilu Prasad, Sung Lee, and Jay D Keasling. BglBrick vectors and datasheets: a synthetic biology platform for gene expression. *Journal of Biological Engineering*, 5(1):12, 2011.

[151] Olaf Ronneberger, Philipp Fischer, and Thomas Brox. U-Net: Convolutional Networks for Biomedical Image Segmentation. *MICCAI*, pages 234–241, 2015.

[152] B Iglewicz and DC Hoaglin. How to detect and handle outliers. *The ASQC Basic References in Quality Control: Statistical Techniques*, 16, 1993.